eXPRESS Polymer Letters Vol.4, No.10 (2010) 589
Available online at www.expresspolymlett.com
DOI: 10.3144/expresspolymlett.2010.73

Editorial corner – a personal view

New frontiers of shape memory polymers

B. K. Kim[*]

Department of Polymer Science and Engineering, Pusan National University, Busan 609-735, Korea

Frequent appearances of reviews and themed issues as well as rapidly increasing number of papers and patents regarding shape memory polymers (SMP) reflect a large room for scientific and technical investigation with ample potential applications of these materials. Permanent shape of SMP created at the primary shaping process is deformed into a temporary shape in rubbery state and fixed upon cooling into the glassy state along a prescribed programming. Upon exposure to external stimulus which typically is heat the permanent shape is recovered by the elasticity of networks.

In contrast to the conventional one-way (irreversible) SMP, two-way (reversible) SMP has recently been reported. The temporary shape under constant stress is subject to cyclic heating and cooling, which cause contraction and extension according to the temperature dependent rubbery modulus. Moreover, multiple shaping has also become possible by providing the materials with multiple transitions, which enable two or more subsequent shape changes upon heating. Hybridizations at nano-level such as nano-filler, nano-tube, and nano-layer as well as with other polymer are new frontiers to enhance the key SM properties. Chemical hybrids of polyurethane with various acrylate are simple choice for multiple transitions.

Chemical hybrid with nano-silica provided the SMP with multifunctional cross-link, reinforcing filler, and relaxation retarder which were evidenced from >99% shape fixity and recovery with negligible hysteresis over repeated cycles. Hybrid bi-layer consisting of two SMPs having different thermal transitions, or SMP coated with gold can be used for de-bondable bonding, electro active polymer, or to reversibly alter its geometry from a tube to a layer upon change in temperature.

Most engineered area of SMP, beside packaging materials, is coatings including self-curable paint, absorption and release of moisture by coated wall, vapor permeable water resistant coatings, and smart textiles. New generation for SMP may be opened with medical devices including minimally invasive surgery, orthodontic devices, delivery vesicles, etc. Prospective works will be directed toward the performance oriented multifunctional (biodegradable, anti-bacterial, health care, swell-deswell) and multi-responsive (light, electric, magnetic field moisture, heat) multi-materials (organic-inorganic hybrids).

Prof. Dr. B. K. Kim
Member of International Advisory Board

---

[*]Corresponding author, e-mail: bkkim@pnu.edu

eXPRESS Polymer Letters Vol.4, No.10 (2010) 590–598
Available online at www.expresspolymlett.com
DOI: 10.3144/expresspolymlett.2010.74

Enhancement of interfacial properties of basalt fiber reinforced nylon 6 matrix composites with silane coupling agents

T. Deák[1], *T. Czigány**[1], *P. Tamás*[1], *Cs. Németh*[2]

[1]Department of Polymer Engineering, Budapest University of Technology and Economics, Műegyetem rkp. 3., H-1111 Budapest, Hungary
[2]Chemical Research Center, Hungarian Academy of Sciences, Pusztaszeri út 59-67., H-1025 Budapest, Hungary

Received 30 April 2010; accepted in revised form 31 May 2010

Abstract. In this work solution surface treatment was applied for producing basalt fiber reinforced PA6 matrix composites. Beyond scanning electron microscopy, static and dynamic mechanical tests, dynamic mechanical analysis of composites was used for qualifying the interfacial adhesion in a wide temperature range. The loss factor peak height of loss factor is particularly important, because it is in close relationship with the mobility of polymer molecular chain segments and side groups, hence it correlates with the number and strength of primary or secondary bondings established between the matrix and the basalt fibers. It was proven, that the interfacial adhesion between basalt fibers and polyamide can be largely improved by the application of silane coupling agents in the entire usage temperature range of composites. The presence of coupling agents on the surface of basalt fibers was proven by Fourier transform infrared spectroscopy. The best results were obtained by 3-glycidoxypropyltrimethoxysilane coupling agent.

***Keywords:** polymer composites, adhesion, basalt fibers*

1. Introduction

Thermoplastic matrix composites have gained great importance in the last 30 years. The most common processing technology of thermoplastic matrix composites is injection molding, which is capable of fabricating products in large quantities with good dimensional accuracy and complex geometry. In the last two decades, due to their good properties, basalt fibers (BF) have come into consideration as potential reinforcement of composite materials. Basalt fibers are incombustible, chemically inert, environmentally and ecologically harmless, and free of carcinogens and other health hazards. Basalt fibers have been comprehensively investigated as reinforcement of polypropylene (PP) matrix composites [1, 2]. Polyamide (PA) has been seldom used for this purpose, although it promises better results, because PA and basalt both have polar chemical structure, thus presumably it is easier to promote proper interface adhesion between the fibers and the matrix. It must be also noted that polyamides have better mechanical properties and higher heat resistance than polypropylene [3–7]. Glass fiber reinforced PA is a vital engineering material in automotive and other industries today. Most car manufacturers employ glass fiber reinforced PA intake manifolds and sumps in their engines. One of the most significant problems of injection molded composites is the formation of proper interfacial adhesion between the matrix and the fibers. It is particularly relevant because during processing the strong shearing stresses reduce the

---

*Corresponding author, e-mail: czigany@eik.bme.hu length of basalt and glass fibers to the order of magnitude of a few tenths millimeters, regardless of their original size. Thus the critical fiber length must be decreased by promoting the interfacial adhesion. In case of BF reinforced PA composites the technology of surface treatment must be developed in order to get composite materials which are comparable with glass fiber reinforced ones. The experiences gained with glass fibers can be used as basis due to the nearly same structure and similar chemical composition of basalt and glass fibers [8]. The most effective way of the enhancement of interfaces in composites is the establishment of strong chemical bonds between the matrix and the fibers. The most common and efficient coupling agents for PA-glass fiber systems are the various silane compounds. The structure of silane molecules is the following: $R–SiX_3$ or $R–(CH_2)_n–SiX_3$. One side of the molecule establishes bond with the surface of the fiber while the other end of the molecule establishes bond with the matrix (Figure 1.). *X* is a hydrolyzable ethoxy ($–OCH_2CH_3$) or methoxy ($–OCH_3$) group, which transforms in water solution through hydrolysis (Figure 1a). Trihydroxysilane is formed during hydrolysis, which develops covalent or hydrogen bonds with the hydroxyl groups on the surface of basalt or glass fibers (Figure 1b). When the fibers are dried, a reversible condensation occurs between the silane molecules and the fiber and between the neighboring silane molecules, forming a polysiloxane layer (Figure 1c). The *R* groups establish bonds with the reactive side groups of the polymer matrix [9–11]. Silane and titanate coupling agents are applied on the surface of fibers during fiber manufacturing. In the industry coupling agents are only one of many components of sizings [2, 8, 12, 13]. Further functions of sizing are protection of fibers, assuring processability and enhancing interfacial adhesion. The currently available continuous basalt fibers are covered with sizings optimized for epoxy, vinylester and polyester resins [9–14]. The methods of enhancing interfacial properties of PP-basalt composites are worked out [15–18], while it is still necessary to find the appropriate technology for PA matrix composites. Probably the coupling agents developed for glass fiber reinforced composites are applicable for BF, due to the similarities between the structure and chemical composition of basalt and glass fibers [19, 20]. The aim of this work was to determine the applicability of silane coupling agents generally applied for glass fiber reinforced PA matrix composites in case of BF. The dependence of properties of composites on the type and amount of silanes was also studied.

2. Experimental

2.1. Materials

In our experiments the original sizing of basalt fibers – applied by the manufacturer – was removed and a new coupling agent was applied, by immersing the fiber in the solution of coupling agent and subsequent drying. This enables the formation of a coating of coupling agent, although we must lack those components of the sizing which have other functions, e.g. the film former. In the first step silane coupling agents with different functional groups were employed (Table 1). Coupling agents

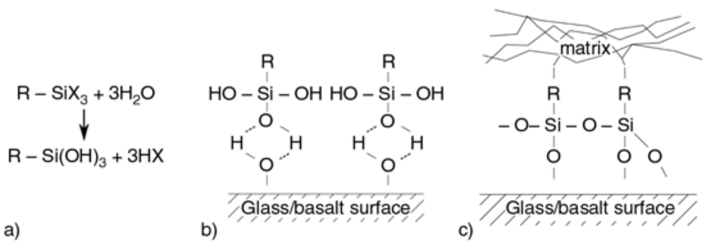

Figure 1. Steps of application of silane coupling agents: hydrolysis (a), formation of bonds between the glass fiber surface and silane (b), polysiloxane (c)

Table 1. Data of used silane coupling agents

Manufacturer	Name	Type	Structure
Wacker Chemie AG	GF80	3-Glycidoxypropyltrimethoxysilane	O / \ $(CH_3O)_3SiC_3H_6OCH_2CH–CH_2$
Wacker Chemie AG	GF91	N-(2-Aminoethyl)-3-aminopropyltrimethoxysilane	$(CH_3O)_3C_3H_6NHC_2H_4NH_2$
Wacker Chemie AG	GF93	3-Aminopropyltriethoxysilane	$(C_2H_5O)_3SiC_3H_6NH_2$

were supplied by Wacker Chemie AG (Burghausen, Germany). These silanes were selected from the types which are most commonly used for glass fiber reinforced composites. The most appropriate of these was selected by comparing the basic mechanical properties of composites. The amount of coupling agents is an important parameter [21], hence further investigations were necessary to assess the effect of coupling agent concentration of composite properties. The above mentioned BF reinforced composites were made with 30 weight% (wt%) fiber content, because for glass fiber reinforced composites this is the most common fiber content. Finally composites were made with different fiber contents. The effectiveness of silane coupling agents was evaluated by the basic static and dynamic mechanical properties of composites and Scanning Electron Microscope (SEM) micrographs, made with a Jeol (Tokyo, Japan) JSM-6380LA instrument.

The matrix was Schulamid 6MV13F polyamide 6 (PA6) from A. Schulman AG (Kerpen, Germany). Basalt fibers were type BCS 13.6 made by Kamenny Vek company (Moscow, Russia). The fibers have an average diameter of 14.2±1.4 μm and are cut to a length of 6 mm. The original sizing was removed by annealing at 400°C for 3 hours. The coupling agents were dissolved in distilled water. Initially the amount of silanes was 1 wt% in the ratio of BF. The basalt fibers were immersed in the solution for 2 hours, after dissolving for 2 hours in order to effectuate the hydrolysis of silanes and their bonding with the hydroxyl groups on the surface of BF. The water was evaporated at 80°C in an air circulating oven. The composites were compounded by a Brabender (Duisburg, Germany) Plasti-Corder PL 2100 twin screw extruder at 255°C and 10 min^{-1} screw rotational speed, afterwards they were granulated. Standard dumbbell specimens with 4×10 mm cross section were made with an Arburg (Lossburg, Germany) 270 C 500-250 injection molding machine at 270°C.

2.2. Methods

Tensile tests were performed according to the EN ISO 527 standard on a Zwick (Ulm, Germany) Z020 universal testing machine. The gauge length was 100 mm, the test speed was 2 mm/min. Elongation was monitored by video extensometer. The 3 point bending tests were performed according to the EN ISO 178 standard. The span length was 64 mm, the test speed was 2 mm/min. Charpy impact tests were performed according to the EN ISO 179 standard with a CEAST (Pianezza, Italy) Resil Impactor instrument, using notched and unnotched specimens. The notch was 'A' type, with 0.25 mm notch tip radius, 45° angle and 2 mm depth. The cross section of the specimens was 4×10 mm, while the span length was 62 mm. The energy absorbed by the specimen was registrated during test and impact strengths α_{cU} for unnotched and α_{cN} for notched specimens) were calculated with Equation (1):

$$\alpha_c = \frac{E_C}{h \cdot w} \cdot 10^3 \tag{1}$$

where E_C is the energy absorbed by the specimen, h is the thickness and w is the width of the specimen (in case of notched specimens w is the residual width). Dynamic Mechanical Analysis (DMA) tests were performed with specimens machined from the injection molded tensile specimens. Tests were executed with dual cantilever configuration and force control (the force amplitude was 400 N) on a Perkin-Elmer (Covina, USA) Diamond DMA instrument from –40 to 180°C. The cross section of specimens was 2×4 mm, the frequency was 1 Hz. The span length was 30 mm. The heating rate was 2°C/min. The surfaces of basalt fibers with different coatings were examined with Fourier transform infrared spectroscopy (FTIR). Tests were performed with a Varian (Palo Alto, USA) Scimitar 2000 instrument. Here the sample is pressed between a diamond and a sapphire. The sample is illuminated through the diamond with infrared light in the wavenumber range between 400 and 4000 cm^{-1}. The reflected light arrives to the spectrometer through the same diamond. The applied samples were bunches of 6 mm long chopped BF. This method is capable of detecting the presence of coupling agents on the surface of BF through identifying atom groups of the silane compounds. Quantitative examination is restrictedly possible by this technique. The residual fiber length in the injection molded specimens was determined in the following way: pieces cut from the middle section of dumbbell specimens were calcinated in ceramic pots with gas flame and in electric oven at 500°C. The fibers were spread on glass slides using formic acid as carrier fluid. The length of fibers was measured with an Olympus (Tokyo, Japan) BX51 optical microscope and analySIS Steel Factory image analysis program, employing through lighting and magnification of 10. The length of 500 fibers was measured from each sample.

3. Results and discussion

The first step was the selection of the most adequate coupling agent. Composites were made with 30 wt% fiber content with fibers treated with the coupling agents shown in Table 1. Mechanical tests were performed according to the previous chapter. The results are shown in Table 2. The composites made with GF80, GF91 and GF93 coupling agents have approximately identical mechanical properties. Considering the results, GF80 coupling agent was chosen for further work because it had the most favorable combination of properties. Figure 2. shows the curves obtained from DMA tests of composites with different types of coupling agents. Neat matrix is denoted by *S*. According to Figure 2, there are very small differences between the DMA curves of composites treated with different coupling agents. This is in accordance with Table 2, where tensile and flexural moduli relate to each other similarly. The amount of coupling agents is a key parameter for solution treatment of fibers. Hence further investigations were needed to determine the effect of solution concentration using the GF80 coupling agent selected previously. The applied concentrations were 0.5, 1, 2 and 4 wt% in ratio of basalt fibers. The optimal concentration was chosen by comparing the basic mechanical properties of composites. The results of mechanical tests are shown in Table 3. It can be seen in Table 3 that all mechanical properties show some form of saturation: the properties seem to approach a limit value with increasing silane concentration. It is obvious that the optimal properties were not reached within the given limits, but the further augmentation of silane concentration would be uneconomical due to the high price of silanes. Finally it can be concluded that among the investigated materials the best composite properties can be reached

Table 2. Mechanical properties of PA6 composites reinforced with basalt fibers treated with different coupling agents

	Type of sizing		
	GF80	**GF91**	**GF93**
Tensile strength, σ_M [MPa]	114.4±0.2	115.2±0.5	113.3±0.3
Tensile modulus, *E* [MPa]	7564±228	7296±287	7669±205
Flexural strength, σ_{fM} [MPa]	159.7±0.7	161.7±0.5	160.4±1.1
Flexural modulus, E_f [MPa]	5963±35	5689±14	5656±23
α_{cN} [kJ/m^2]	10.1±0.5	9.7±0.3	9.6±1.0
α_{cU} [kJ/m^2]	82.4±6.1	83.3±2.6	71.3±6.4

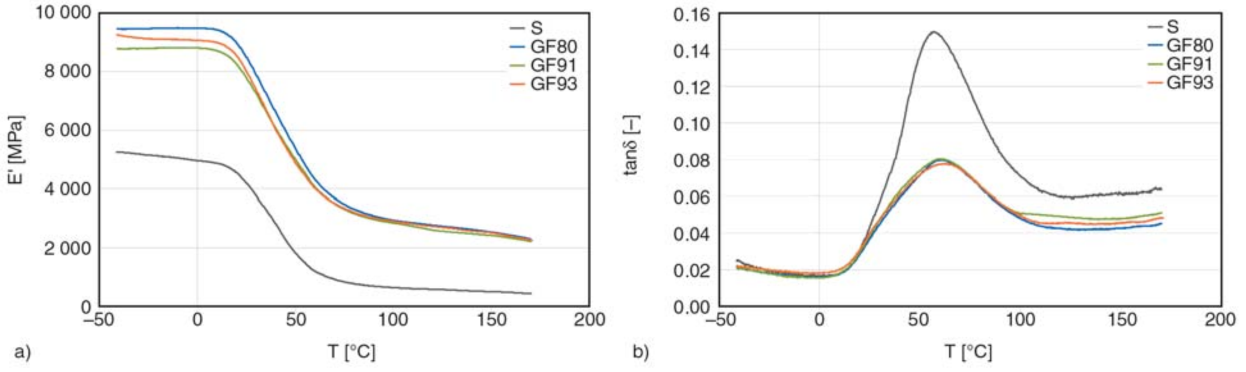

Figure 2. DMA curves of composites with different types of coupling agents (E': storage modulus, tanδ: loss factor)

Table 3. Mechanical properties of PA6 composites reinforced with basalt fibers treated with GF80 coupling agent at different concentrations

	Concentration of sizing			
	GF80 0.5%	**GF80 1%**	**GF80 2%**	**GF80 4%**
Tensile strength, σ_M [MPa]	108.4±0.1	113.2±1.3	119.0±0.5	120.0±1.1
Tensile modulus, *E* [MPa]	7337±70	7564±228	7673±141	7789±210
Flexural strength, σ_{fM} [MPa]	155.2±1.2	162.7±0.5	167.6±0.2	170.8±1.4
Flexural modulus, E_f [MPa]	5685±7	5936±35	5996±21	6065±15
α_{cN} [kJ/m^2]	9.3±0.8	10.1±0.5	11.3±12.7	12.7±0.4
α_{cU} [kJ/m^2]	66.8±3.5	82.4±6.1	86.0±2.8	88.4±8.2

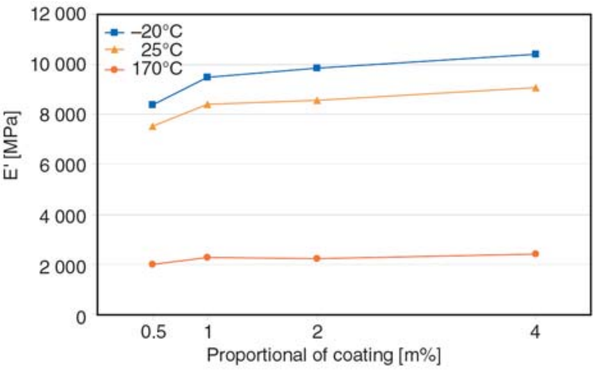

Figure 3. Storage moduli of composites with GF80 coupling agent at –20, 25 and 170°C temperature as the function of proportion of coating correlated to basalt fibers

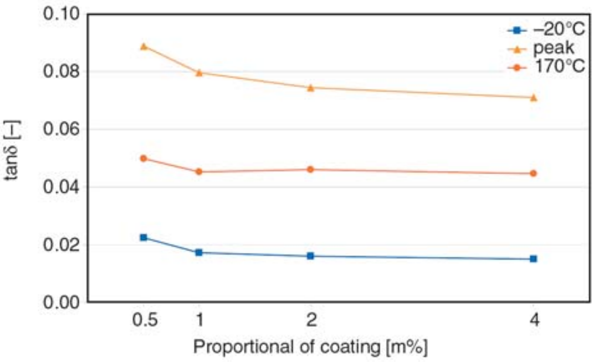

Figure 4. Loss factors of composites with GF80 coupling agent at –20 and 170°C and at the curve peak as the function of proportion of coating correlated to basalt fibers

with GF80 3-glycidoxypropyltrimethoxysilane applied on basalt fibers in a 4 wt% ratio. Figures 3 and 4 show the results of DMA tests of composites with GF80 coupling agent as the function of proportion of coating correlated to BF. In order to make results more expressive, storage modulus (E') and loss factor (tanδ) values are represented as the function of silane concentration and fiber content. Since this mode of representation does not allow us to use a continuous temperature range, 3 allotted temperatures were chosen for the diagrams: –20, 25 and 170°C for the storage modulus. Loss factors were outlined at –20, and 170°C, and at the temperature of the tanδ curve peak. The height of tanδ curve peak is in close relationship with the mobility of polymer molecular chain segments and side groups, hence it correlates with the number and strength of primary or secondary bondings established between the matrix and the BF. The growth of E' with increasing silane concentration is corresponding with Table 3. The loss factor is decreasing with growing silane concentration, but it also shows saturation, approaching a limit value. It can be concluded from Figures 3 and 4 that the tanδ peak is very sensitive to the strength of interfacial adhesion, but storage modulus also shows the differences at other temperatures. The next step was to evaluate the applicability of this surface treatment for composites with different fiber contents. Composites were made with 10, 20, 30 and 40 wt% BF content. Fibers were coated with 4 wt% GF80 silane coupling agents (marking: GF80). For comparison composites also were made with untreated BF (marking: SN). The results of mechanical tests are shown in Table 4. Unnotched neat PA6 specimens were not broken during Charpy tests, therefore only the impact strengths of composites are shown in the last line of Table 4. Table 5 shows the residual fiber lengths in the injection molded dumbbell specimens. It can be seen in Table 4 that coupling agents considerably improve the static mechanical properties of composites. The tensile strength is increased by 40%, while flexural

Table 4. Mechanical properties of PA6 composites reinforced with untreated and 4 wt% GF80 silane coated basalt fibers

	Sizing	Fiber content				
		0 wt%	**10 wt%**	**20 wt%**	**30 wt%**	**40 wt%**
Tensile strength, σ_M [MPa]	GF80	57.8±0.3	80.5±0.3	100.0±4.0	120.0±1.1	128.4±1.4
	SN		63.7±0.1	71.3±1.2	84.2±0.2	86.9±0.1
Tensile modulus, E [MPa]	GF80	2669±180	3903±81	4849±552	7789±210	9904±403
	SN		3529±251	5172±209	7529±375	8756±266
Flexural strength, σ_{fM} [MPa]	GF80	61.0±0.5	92.4±0.8	122.8±0.4	170.3±2.1	182.5±1.5
	SN		84.1±1.5	103.9±2.2	124.7±0.2	129.8±0.2
Flexural modulus, E_f [MPa]	GF80	1790±7	2834±34	4090±14	6065±15	7223±64
	SN		2741±92	3847±118	6184±33	7717±22
α_{cN} [kJ/m^2]	GF80	21.7±0.6	6.8±0.5	6.8±1.2	12.7±0.4	12.8±1.2
	SN		4.4±0.5	5.3±0.4	5.6±0.7	7.2±0.7
α_{cU} [kJ/m^2]	GF80	–	37.5±4.0	37.9±5.1	88.4±8.2	88.9±2.2
	SN		20.3±0.1	22.3±0.3	27.3±0.3	31.1±0.3

Table 5. Residual fiber length [µm] in injection molded specimens as the function of fiber content

Fiber content [wt%]	Sizing	
	GF80	**SN**
10	0.224±0.161	0.208±0.119
20	0.217±0.166	0.201±0.129
30	0.189±0.132	0.183±0.097
40	0.157±0.110	0.152±0.102

strength is improved by 30% by the surface treatment. At the same time moduli practically were not influenced by the coupling agent. Fiber reinforcement decreases the impact strength compared to the matrix, but adding more fibers to the system causes the gradual growth of impact strength. It can be ascribed to the fact that basalt fibers increase the stiffness and rigidity of the composite, thus causing a decline of impact resistance, and can work as starting point of cracks. However, if the amount of reinforcing fiber grows considerably, the fibers rather stop crack propagation, which leads to a higher impact strength. Fiber surface treatment increased the impact strength with 100 to 200%.

Table 5 shows that during processing (compounding, grinding and injection molding) the basalt fibers are fragmented to an average length around 0.15 to 0.20 mm. The average length decreases nearly linearly with increasing fiber content, and no remarkable difference can be found between sized and unsized fibers. Scanning electron micrographs of the fracture surfaces of tensile specimens are shown in Figure 5. It can be seen in Figure 5 that a thick layer of matrix material evolves on the surface of silane coated BF during fracture. It shows excellent interfacial strength, which means that fracture occurs rather in the matrix and not on the interface, which is reinforced by primary bondings. At the same time the surface of untreated BF completely disengages from the matrix. It shows that if there is any adhesion between the fibers and the matrix, it is much weaker than the shear strength of the matrix. Figures 6 to 8 show the results of DMA tests of composites with GF80 coupling agents at different fiber contents. It can be seen in Figures 6 and 7 that fiber content strongly influences E'. The

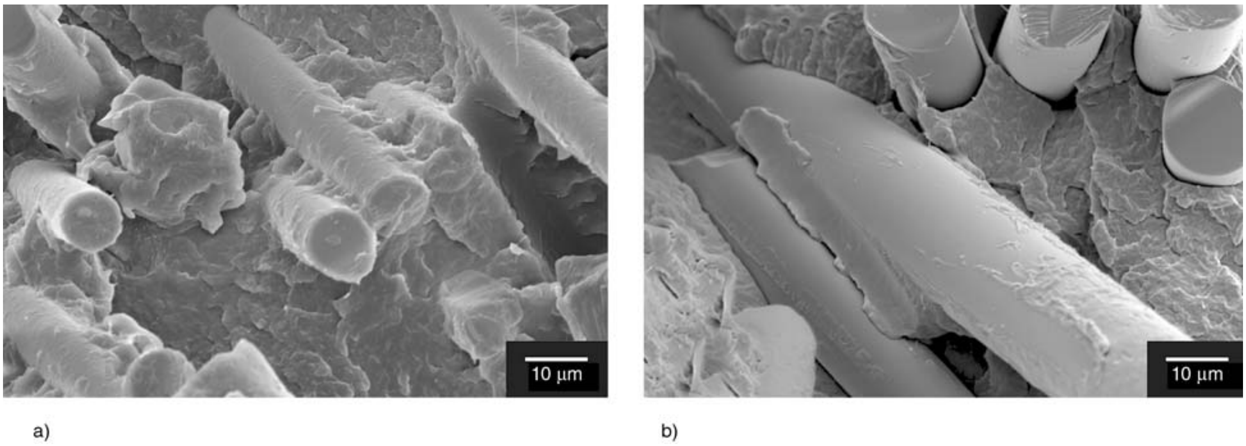

Figure 5. SEM micrographs of fracture surfaces of tensile specimens of composites, a: with 4 wt% GF80 silane coupling agent, b: unsized fibers

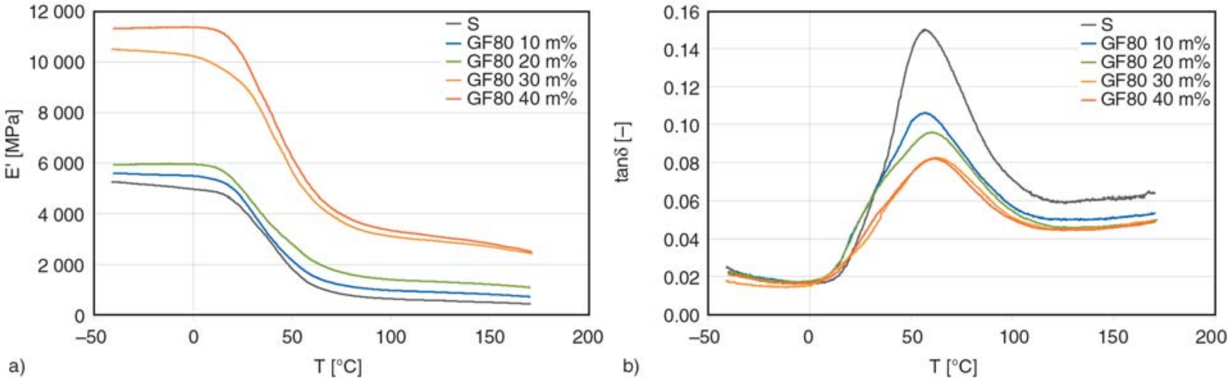

Figure 6. DMA curves of composites with GF80 coupling agent at different fiber contents (E': storage modulus, tanδ: loss factor)

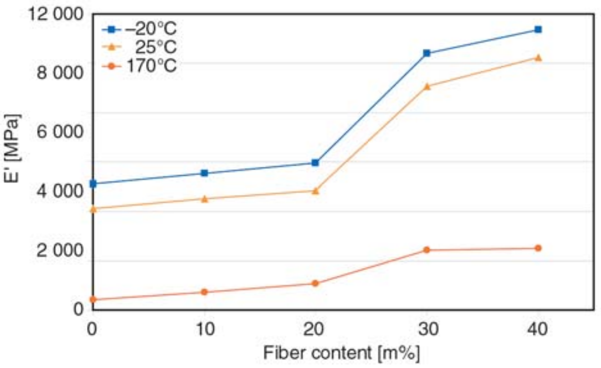

Figure 7. Storage moduli of composites with 4 wt% GF80 coupling agent at –20, 25 and 170°C temperature as the function of fiber content

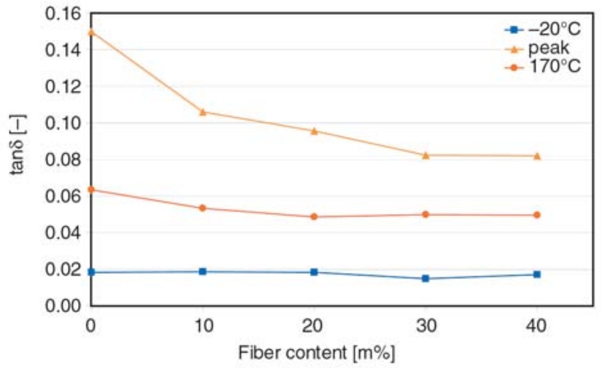

Figure 8. Loss factors of composites with 4 wt% GF80 coupling agent at –20, 25 and 170°C temperature as the function of fiber content

advances that fiber reinforcement offers for high temperatures applications is also obvious: the storage modulus of 40 wt% BF reinforced composite at 170°C is not lower than the *E′* of the matrix at room temperature. It can be concluded that DMA tests are suitable for assessing the quality of interfacial adhesion in PA matrix composites in a wide temperature range.

FTIR tests were performed on BF with GF80 coupling agent in order to prove the presence of the coupling agent on the surface of basalt fibers. The verification of the presence of coupling agents is possible by identifying atom groups which are in the coupling agents but can not be found in basalt [22]. The presence of coupling agents on the surface of fibers was proven in the wavenumber range between 2700 and 3100 cm^{-1}. Figure 9 shows the spectrum of BF sized with different concentrations of GF80 silane. ‘Calcinated’ refers to the basalt fiber which were cleaned from sizing by annealing. The peaks at 2850 and 2925 cm^{-1} are in connection with C–H bondings in aliphatic carbon chains. No distinct peaks can be seen on the curves of calcinated BF. The height of peaks in Figure 9 shows some correlation with the concentration of GF80 silane, but it must be noticed that quantitative examinations are restrictedly possible by this method. FTIR tests proved the presence the GF80 coupling agent on the surface of BF, basically by detecting the C–H bondings of the aliphatic carbon chains in the middle sections of silane molecules. The sufficient removal of the original sizing was also validated. It can be concluded that the presence of coupling agents on the BF was proven. However, the applied method could not confirm the formation of chemical bondings between the fibers and the coupling agents.

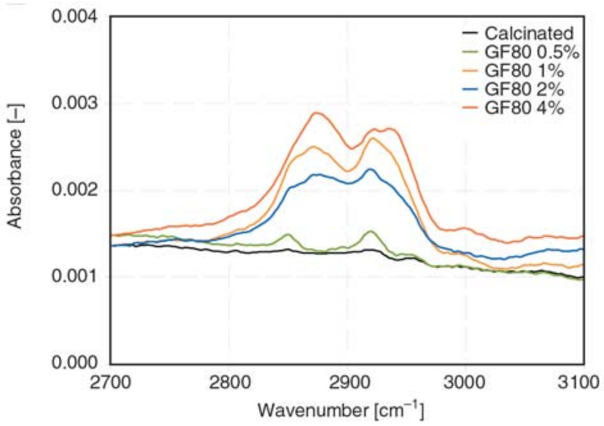

Figure 9. FTIR absorbance spectrum of basalt fibers sized with GF80 silane with different concentrations in the wavenumber range between 2700 and 3100 cm^{-1}

4. Conclusions

It was proven that silane coupling agents developed for glass fibers are applicable for basalt fibers. This is due to the approximately same structure and similar chemical composition of basalt and glass fibers. All three applied silane coupling agents influenced all investigated properties of the composites auspiciously. The optimum of concentration of coupling agents was not reached, among the given limits the application of 4 wt% of GF80 3-glycidoxypropyltrimethoxysilane gave the best results. In case of 30 wt% BF reinforced composites the tensile strength grew by 42%, the flexural strength grew by 37% and the impact strength grew by 223% compared with unsized composite. The comprehensive DMA testing of composites and the matrix revealed that this method is suitable for assessing the quality of fiber-matrix interface of thermoplastic matrix composites in a wide temperature range, from deep below 0°C up to the vicinity of the melting temperature. The loss factor curves of DMA contain much information regarding the quality of interface. The peak height of tanδ is particularly important, because it is in close relationship with the mobility of polymer molecular chain segments and side groups, hence it correlates with the number and strength of primary or secondary bondings established between the matrix and the BF. The tanδ values can be compared in the entire temperature range. Their properties make basalt fiber reinforced PA matrix composite an engineering material which can be used in the industry in all fields where glass fiber reinforced composites have gained ground.

Acknowledgements

Kamenny Vek, Wacker and Arburg are kindly acknowledged for provision of the raw materials and supporting the work. This work was supported by Hungarian Scientific Research Fund (OTKA K61424 and NI62729).

References

[1] Botev M., Betchev A., Bikiaris D., Panayiotou C.: Mechanical properties and viscoelastic behavior of basalt fiber-reinforced polypropylene. Journal of Applied Polymer Science, **74**, 523–531 (1999). DOI: 10.1002/(SICI)1097-4628(19991017)74:3<523::AID-APP7>3.0.CO;2-R

[2] Czigány T., Deák T., Tamás P.: Discontinuous basalt and glass fiber reinforced PP composites from textile prefabricates: Effects of interfacial modification on the mechanical performance. Composite Interfaces, **15**, 697–707 (2008). DOI: 10.1163/156855408786778302

[3] Hári J., Dominkovics Z., Fekete E., Pukánszky B.: Kinetics of structure formation in PP/layered silicate nanocomposites. Express Polymer Letters, **3**, 692–702 (2009). DOI: 10.3144/expresspolymlett.2009.87

[4] Lyons J. S.: Linear viscoelastic analysis of the room-temperature creep behavior of glass-reinforced aromatic and aliphatic thermoplastics. Polymer Testing, **22**, 545–551 (2003). DOI: 10.1016/S0142-9418(02)00151-4

[5] Kovács J. G., Solymossy B.: Effect of glass bead content and diameter on shrinkage and warpage of injection-molded PA6. Polymer Engineering and Science, **49**, 2218–2224 (2009). DOI: 10.1002/pen.21470

[6] Laura D. M., Keskkula H., Barlow J. W.: Effect of glass fiber surface chemistry on the mechanical properties of glass fiber reinforced, rubber-toughened nylon 6. Polymer, **43**, 4673–4687 (2002). DOI: 10.1016/S0032-3861(02)00302-6

[7] Sui G., Wong S-C., Yue C-Y.: Effect of extrusion compounding on the mechanical properties of rubber-toughened polymers containing short glass fibers. Journal of Materials Processing Technology, **113**, 167–171 (2001). DOI: 10.1016/S0924-0136(01)00627-6

[8] Deák T., Czigány T.: Chemical composition and mechanical properties of basalt and glass fibers: A comparison. Textile Research Journal, **79**, 645–651 (2009). DOI: 10.1177/0040517508095597

[9] Zweifel H.: Plastics additives handbook. Hanser, München (2001).

[10] Kumar A., Gupta R. K.: Fundamentals of polymers. McGraw-Hill, New York (1998).

[11] Noda K., Tsuji M., Takahara A.: Aggregation structure and molecular motion of (glass-fiber/matrix nylon 66) interface in short glass-fiber reinforced nylon 66 composites. Polymer, **43**, 4055–4062 (2002). DOI: 10.1016/S0032-3861(02)00200-8

[12] Hull D.: An introduction to composite materials. Cambridge University Press, Cambridge (1981).

[13] Mészáros L., Tábi T., Kovács J. G.: The effect of EVA content on the processing parameters and the mechanical properties of LDPE/ground tire rubber blends. Polymer Engineering and Science, **48**, 868–874 (2008). DOI: 10.1002/pen.21022

[14] Ragosta G., Musto P.: Polyimide/silica hybrids via the sol-gel route: High performance materials for the new technological challenges. Express Polymer Letters, **3**, 413–428 (2009). DOI: 10.3144/expresspolymlett.2009.51

[15] Fritzsche J., Das A., Jurk R., Stöckelhuber K. W., Heinrich G., Klüppel M.: Relaxation dynamics of carboxylated nitrile rubber filled with organomodified nanoclay. Express Polymer Letters, **2**, 373–381 (2008). DOI: 10.3144/expresspolymlett.2008.44

[16] Kovács J. G.: Construction of pre-deformed shapes for rapid tooling in injection molding. Macromolecular Symposia, **239**, 259–265 (2006). DOI: 10.1002/masy.200690105

[17] Keszei S., Matkó Sz., Bertalan Gy., Anna P., Marosi Gy., Tóth A.: Progress in interface modifications: From compatibilization to adaptive and smart interphases. European Polymer Journal, **41**, 697–705 (2005). DOI: 10.1016/j.eurpolymj.2004.10.039

[18] Güllü A., Özdemir A., Özdemir E.: Experimental investigation of the effect of glass fibres on the mechanical properties of polypropylene (PP) and polyamide 6 (PA6) plastics. Materials and Design, **27**, 316–323 (2006).
DOI: 10.1016/j.matdes.2004.10.013

[19] Militký J., Kovacic V., Rubnerová J.: Influence of thermal treatment on tensile failure of basalt fibers. Engineering Fracture Mechanics, **69**, 1025–1033 (2002).
DOI: 10.1016/S0013-7944(01)00119-9

[20] Bernardo E., Stoll E., Boccaccini A. R.: Novel basalt fibre reinforced glass matrix composites. Journal of Materials Science, **41**, 1207–1211 (2006).
DOI: 10.1007/s10853-005-3658-0

[21] Chou S., Lin L-S., Yeh J-T.: Effect of surface treatment of glass fibres on adhesion to phenolic resin. Polymers and Polymer Composites, **7**, 21–31 (1999).

[22] Grellmann W., Seidler S.: Polymer testing. Hanser, München (2007).

eXPRESS Polymer Letters Vol.4, No.10 (2010) 599–610
Available online at www.expresspolymlett.com
DOI: 10.3144/expresspolymlett.2010.75

Synthesis and self-assembly behavior of amphiphilic diblock copolymer dextran-block-poly(ε-caprolactone) (DEX-*b*-PCL) in aqueous media

Y. L. Zhang, X. W. Dou, T. Jin[*]

Laboratory of Drug Delivery and Biomaterials, Shanghai Jiao Tong University School of Pharmacy, Shanghai 200240, P. R. China

Received 11 April 2010; accepted in revised form 11 June 2010

Abstract. An amphiphilic diblock copolymer, dextran-block-poly(ε-caprolactone) (DEX-*b*-PCL), with a series of well-defined chain lengths of each block was prepared by conjugating a dextran chain with a PCL block via aza-Michael addition reaction under mild conditions. For the dextran block, samples with relatively uniform molecular weight, 3.5 and 6.0 kDa, were used, and the PCL blocks were prepared via ring-opening polymerization at defined ratios of ε-caprolactone to initiator in order to give copolymers with mass fraction of dextran (f_{DEX}) ranging from 0.16 to 0.45. When these copolymers were allowed to self-assemble in aqueous solution, the morphology of assembled aggregates varied as a function of f_{DEX} when characterized by transmission electron microscope (TEM), fluorescence microscope (FM) and dynamic laser scattering (DLS). As f_{DEX} decreases gradually from 0.45 to 0.16, the morphology of the copolymer assembly changes from spherical micelles to worm-like micelles and eventually to polymersomes, together with an increase in particle sizes.

Keywords: *polymer synthesis, biodegradable polymers, diblock copolymer, self-assembly, mass fraction of the hydrophilic block*

1. Introduction

Amphiphilic block copolymers have been widely reported to form particulate systems of various morphologies such as spherical or worm-like micelles, polymersomes, large compound micelles, lamellae, and numerous other aggregates [1–8]. Among these morphologies, polymersomes are particularly interesting for their potential applications as carriers of biological therapeutics and diagnostic agents [9, 10]. Polymersomes differ from polymeric particles and micelles in having a hydrophilic interior to pack biological molecules, and are superior to liposomes for their better mechanical stability and adjustable chemical properties. The thermodynamically stable morphology of block copolymer assemblies is determined by several variables, such as composition and chain length of each block, the ratio of hydrophilic to hydrophobic block, concentrations, as well as solvents, temperatures, additives and so on [11–13]. Among these variables, the chemical nature of diblock copolymers is considered to be the most essential. Discher and Eisenberg have demonstrated that volume fraction of the hydrophilic block (f) is an important factor leading to corresponding time-average shape of the copolymers (e.g. cylinder when $f = 0.35\pm0.10$, wedge when $f < 0.25$ and cone when $f > 0.45$), and these shapes are critical in determining the morphology of copolymer assemblies as polymersomes, worm-like micelles, or spherical micelles [11, 14]. Their study offered a useful guideline to prepare desired

---

[*]Corresponding author, e-mail: tjin@sjtu.edu.cn

nanostructures of poly(ethylene glycol)-block-poly(lactic acid) (PEG-PLA) copolymers. Although the *f* range of PEG-PLA may not be applicable to other block copolymers because of their different chemical natures, the demonstrated relationship between fraction of hydrophilic block, molecular shape of copolymer and particle morphology should be universal. Therefore, for each individual block copolymer, scaling relationships between the hydrophilic fraction of copolymer and various aggregate morphologies should be investigated systematically in order to prepare aimed structure of the copolymer.

While PEG has been used as hydrophilic block for most block copolymers to form polymersomes [14–17], it may inhibit bio-macromolecules from being encapsulated into polymersome interior because of its hydrodynamic nature and protein repelling habits (anti-opsonization effect) [18–20]. Because the polymersome interior is limited in space, PEG at the surface of the inner layer is highly crowded and tends to drive macromolecules out of the vesicle interior. It has been reported that the encapsulation efficiency of BSA (bovine serum albumin) into PEG-based polymersomes was only 5% [21]. To address this problem, using a protein-friendly hydrophilic block to substitute PEG in the diblock copolymers should be a reasonable approach to improve encapsulation efficiency and protein stability. In the present study, we selected dextran as the hydrophilic segment to prepare an amphiphilic diblock polymer. Dextran is widely used as blood substitution, drug carriers and aqueous phase material for protein purification because its definite biocompatibility, biodegradability, hydrophilicity and high affinity to bio-macromolecules [22, 23]. In addition, dextran possesses multiple hydroxyls which are convenient for chemical modification to endow polymersome surfaces with various desired functions such as drug-targeting and diagnostic recognition. In addition, poly(ε-caprolactone) (PCL) was chosen as the hydrophobic block of the amphiphilic copolymer for its well demonstrated biocompatibility, biodegradability, and wide utilization as a drug delivery material [24, 25]. However, there are limited studies regarding block copolymers with dextran as hydrophilic segment so far. Houga *et al.* [26] have reported self-assembly of dextran-block-polystyrene (DEX-*b*-PS) into micelles and polymersomes. Liu and co-workers have prepared a dextran-PCL block copolymer and studied its micellar characteristics [27]. A study on the polymersomes prepared by dextran-block-poly(γ-benzyl-L-glutamate) was carried out by Schatz *et al.* [28]. Hernandez *et al.* [29] have synthesized double hydrophilic block copolymers of carboxymethyl dextran-block-poly(ethylene glycol) (CMD-PEG) and studied their self-assembly behavior as a function of solution pH. Yang *et al.* [30] also prepared double hydrophilic diblock copolymer of hyaluronan-block-poly(2-ethyl-2-oxazoline) via terminal reductive amination. Very recently, Sun and his co-workers prepared disulfide-linked dextran-*b*-poly(ε-caprolactone) diblock copolymer (DEX-SS-PCL) copolymer and self-assembled into micelles with a diameter of about 60 nm [31]. To the best of our knowledge, there has not yet been a report describing polymersomes formed by dextran-*b*-PCL block copolymers.

According to literature methods, the synthetic strategies for saccharide-terminated polymers can mainly be classified into two approaches. The first approach is based on end to end coupling strategy via reductive amination or aza-Michael addition [27, 32–34]. The second approach is that the saccharides are first derivatized into macro-initiators and then initiate the controlled or living polymerization of monomers [26, 35]. The latter synthetic procedure requires several steps, including tedious protecting-deprotecting steps. Furthermore, if the hydroxyl groups on the backbone of the saccharides are not protected completely, comb-like grafted copolymers other than diblock copolymers would be obtained. For the end to end conjugation of dextran and PCL blocks, a pioneering work has been performed by Liu *et al.* [27] who coupled an amino-functionalized dextran to acryloyl-functionalized PCL with the catalyst of p-methylbenzene sulfonic acid at 120°C for 8 h. However, Moreau has indicated that high temperatures such as above 100°C are not appropriate for dextran because it could be degraded [36]. Therefore, the reaction conditions should be selected carefully to avoid degradation of reaction precursors. Because maleimide possesses two carbonyl groups conjugated to the double bond, presenting a highly electronegative property and more susceptible to reaction with nucleophiles [37], it is proved to be an appropriate reactive group in Michael addition under mild conditions [34, 38]. We report herein a mild and simplified route to synthesize the copolymer DEX-*b*-PCL, in which the precursors maleimide-terminated PCL and amino-terminated dextran were synthesized previously, followed by an end to end coupling via aza-Michael addition reaction.

In this paper, using the rationally synthesized DEX-*b*-PCL, we investigated the self-assembly behaviors of this amphiphilic diblock copolymer as a function of the structural parameters of the block copolymer. The relationship of the hydrophilic mass fractions of DEX-*b*-PCL copolymers (f_{DEX}) with their self-assembled morphologies in aqueous medium is addressed. Based on our own experiences, a predetermined f_{DEX} range within 0.16 to 0.45 was selected to cover all the three morphological forms of block copolymer assemblies. When the mass fraction of the hydrophilic chain decreases from 0.45 to 0.16, the morphological form of the copolymer assemblies vary from spherical micelles, worm-like micelles, nano-sized polymersomes to giant polymersomes accordingly.

2. Experimental

2.1. Materials

ε-Caprolactone (ε-CL) (99%) was supplied by Sigma-Aldrich, Inc. Shanghai, China. Prior to use, the ε-CL was dried over CaH_2 for 48 h and distilled under reduced pressure. Dextran T3.5 (M_w 3500 g·mol^{-1}, polydispersity index, i.e. PDI~1.5) and T6 (M_w 6000 g·mol^{-1}, PDI~1.5) were purchased from Pharmacosmos A/S, Holbaek, Denmark. Stannous octoate (95%), $Sn(Oct)_2$, was supplied by Sigma-Aldrich, Inc. Shanghai, China. Sodium cyanoborohydride ($NaCNBH_3$, 97%) was purchased from Alfa Aesar, TianJin, China. N-hydroxyethyl maleimide (HEMI) was synthesized according to the literature procedures [39, 40]. The toluene and dimethyl sulfoxide (DMSO) (analytical grade, provided by Sinopharm Chemical Reagent Co., Shanghai, China) were first dried over $CaCl_2$ and CaH_2, respectively, and then distilled prior to use. All other reagents were analytical grade and used as received.

2.2. Synthesis of HEMI-PCL

The poly(ε-caprolactone) end-capped with N-hydroxyethyl maleimide (HEMI-PCL) was prepared by ring opening polymerization of ε-caprolactone using N-hydroxyethyl maleimide as the initiator and $Sn(Oct)_2$ as a catalyst. Briefly, a predetermined amount of HEMI was introduced into a 150 ml three-necked flask connected to a vacuum/nitrogen line. After three times of nitrogen purge, 5.0 g ε-caprolactone (43.8 mmol), 0.017 g $Sn(Oct)_2$ (0.043 mmol) were dissolved in 30 ml toluene and injected into the flask under nitrogen atmosphere and allowed to react under magnetic stirring at 120°C for 15 hours. Molecular weight of HEMI-PCL was determined by the molar ratio of ε-caprolactone to HEMI. The reaction was then terminated by cooling the reactants down to room temperature, followed by precipitating the product in methanol. The obtained HEMI-PCL was further purified by three additional cycles of solubilization (in chloroform) and precipitation (in methanol). Finally, the obtained product was dried at room temperature under vacuum for 48 h.

^{1}H NMR ($CDCl_3$ 300 MHz):
δ=6.74 (s, 2H, $-C\underline{H}=C\underline{H}-$),
4.24 (t, 2H, $-N-CH_2-C\underline{H}_2-O-$),
4.07 (t, 2H, $-C\underline{H}_2-O-C(O)-$),
3.80 (t, 2H, $-N-C\underline{H}_2-$),
3.65 (t, 2H, $-C\underline{H}_2-OH$), 2.31 (t, 2H, $-C(O)-C\underline{H}_2-$),
1.71–1.61 (m, 4H, $-CH_2-C\underline{H}_2-CH_2-C\underline{H}_2-CH_2-O-$),
1.44–1.34 (m, 2H, $-CH_2-CH_2-C\underline{H}_2-CH_2-CH_2-O-$).

2.3. Synthesis of EDA-DEX

The 1,2-ethylenediamine-terminated dextran (EDA-DEX) was prepared by terminal reductive amination reaction with sodium cyanoborohydride ($NaCNBH_3$) as reducing agent according to Figure 1. Briefly, 20 mg of $NaCNBH_3$ was added into a 50 ml DMSO solution containing 5.0 g dextran and excess of 1,2-ethylenediamine (10-fold molar excess over dextran). The reactant mixture was stirred at 60°C for 7 days, and additional $NaCNBH_3$ (20 mg) was added each day. Then the reaction was terminated by cooling the reactants to room temperature, followed by pouring the mixture into methanol to precipitate. The product was then purified by three cycles of dissolving (in water) and precipitating (in methanol) treatment, and finally lyophilized prior to storage.

^{1}H NMR (DMSO-d_6 300 MHz):
δ=4.67 (s, 1H, anomeric H),

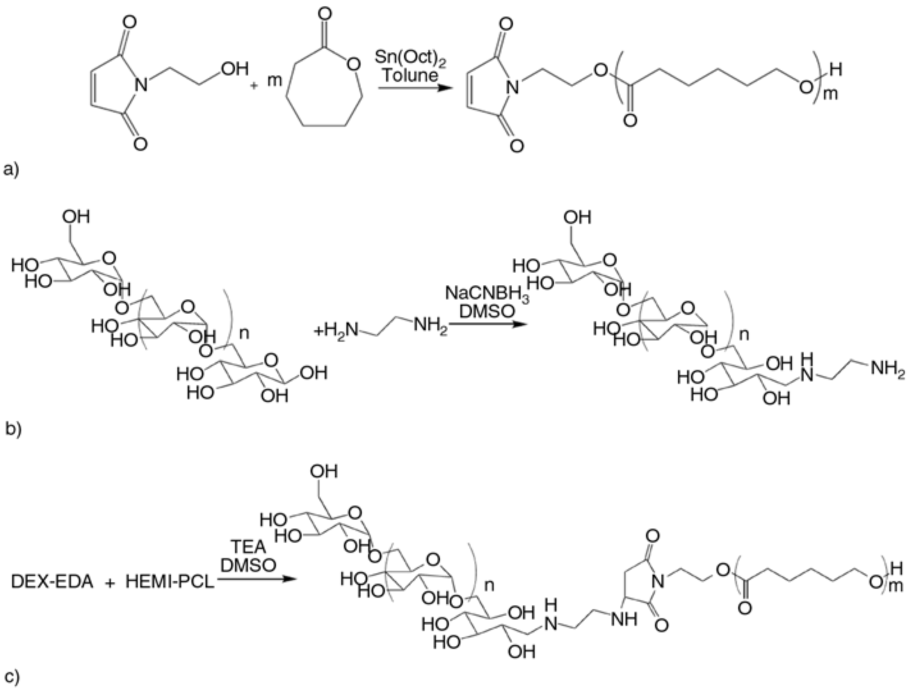

Figure 1. Synthetic route for amphiphilic diblock copolymer DEX-*b*-PCL

3.0–3.8 (m, 5H, glycosidic H),
2.92 (m, 4H, $–NH–C\underline{H}_2–C\underline{H}_2–NH_2$).

2.4. Synthesis of DEX-*b*-PCL

The dextran-block-poly (ε-caprolactone) (DEX-*b*-PCL) copolymers were prepared by end-to-end conjugation of the EDA-DEX and HEMI-PCL via aza-Michael addition described as Figure 1. HEMI-PCL (1.0 g) and extra amount of EDA-DEX (2 molar equivalents of HEMI-PCL) as well as catalytic amount of triethylamine (TEA) were dissolved in 20 ml DMSO and kept in a round-bottom flask. The reaction was performed under magnetic stirring at 70°C for 48 h. Then the reaction mixture was cooled to room temperature and DMSO was removed by evaporation under a reduced pressure. The resulting product was purified by washing with small amount of water to remove un-reacted EDA-DEX, then with tetrahydrofuran (THF) to remove the un-reacted HEMI-PCL. The obtained product was converted to white powder after lyophilization.

^1H NMR (DMSO-d_6 300 MHz):
δ=4.92 (s, 1H, glycosidic–C_4–O$\underline{H}$),
4.86 (s, 1H, glycosidic–C_3–O$\underline{H}$),
4.65 (s, 1H, anomeric H),
4.51 (s, 1H, glycosidic–C_2–O$\underline{H}$),
3.96 (t, 2H, $–C\underline{H}_2–O–$),
3.0–3.8 (m, 5H, glycosidic H),
2.45 (t, 2H, $–C(O)–C\underline{H}_2–$),
1.50 (m, 4H, $–CH_2–C\underline{H}_2–CH_2–C\underline{H}_2–CH_2–O–$),
1.27 (m, 2H, $–CH_2–CH_2–C\underline{H}_2–CH_2–CH_2–O–$).

2.5. Self-assembly of DEX-*b*-PCL

The block copolymer, DEX-*b*-PCL, of given dextran fraction was added in aqueous media at a concentration of 0.5 mg·ml$^{–1}$, followed by vortex for dispersion. The resulted suspension was then incubated at 60°C for 12–48 h. The morphology of the particulates formed from the block copolymer was characterized by TEM and DLS.

2.6. Characterization

2.6.1. ^1H NMR

Proton nuclear magnetic resonance (^1H NMR) spectra of the polymers were recorded on a NMR Spectrometer (ARX-300, Bruker, Switzerland) operating at 300 MHz at 25°C. Deuterated chloroform ($CDCl_3$) and dimethyl sulfoxide-d_6 (DMSO-d_6) were used as solvents.

2.6.2. GPC

Gel permeation chromatography (GPC) measurements were performed using a Waters HPLC system equipped with a Waters 410 refractive index

(RI) detector, a Waters 515 HPLC pump (Waters, Milford, MA, USA) and a Waters ultra-styragel column (5 µm) at 40°C. The sample, 20 µl in volume, was injected to the system and eluted with dimethylformamide mobile phase containing 0.1% lithium bromide at a flow rate of 1.0 ml min^{-1}. The calibration of molecular weight was carried out using polystyrene as standard.

2.6.3. TEM

The transmission electron microscopic (TEM) images were taken using an electron microscope system (JEM2010, JEOL, Japan) at an acceleration voltage of 120 kV. TEM samples were prepared by placing one drop of the aggregate suspension onto a copper mesh covered with carbon film. After 1 h, the excess solution was removed with a filter paper followed by negative staining with 2% [w/v] phosphotungstic acid solution (pH 7.0) for 30 s. For some samples, the staining treatment was omitted.

2.6.4. FM

The fluorescence microscopic (FM) images of the self-assembled particulate samples were taken using an inverted microscope (Olympus IX71, Olympus Optical Co. Ltd, Tokyo, Japan) equipped with 10X, 20X, 40X UPlanFL objectives, a 100w mercury bulb and a DP 70 color CCD camera, as well as Olympus DP capture software.

2.6.5. DLS

Dynamic laser scattering (DLS) measurements were performed using a 90 Plus/BI-MAS particle size analyzer (90 Plus/BI-MAS, Brookhaven Instruments Corporation, USA). The samples of self-assembled diblock copolymers were suspended in 0.01 M phosphate buffer solution (PBS, pH 7.4) at the concentration of 0.5 mg·ml^{-1} prior to measurements. Hydrodynamic radius R_h of the particles was calculated based on three repeated measurements.

3. Results and discussion

3.1. Preparation of amphiphilic diblock copolymers

The amphiphilic diblock copolymers DEX-*b*-PCL were successfully prepared by combination technologies of ROP, a reductive amination reaction and an aza-Michael addition according to Figure 1. The characteristics of the diblock copolymers and their precursors were determined by ^{1}H NMR, GPC analysis and the results were summarized in Table 1 and Table 2. In order to obtain diblock copolymers DEX-*b*-PCL with various f_{DEX}, two precursors, HEMI-PCL and EDA-DEX, of different chain

Table 1. Synthesis and characterization of HEMI-PCL by ROP

Polymer sample[a]	M/I[b]	DP[c]	M_n[d] [g/mol]	M_n[e] [g/mol]	PDI[e]	Yield[f] [%]
HEMI-PCL$_{7.5k}$	65	66	7500	12000	1.12	92
HEMI-PCL$_{9.2k}$	80	80	9200	13200	1.15	89
HEMI-PCL$_{11.9k}$	100	105	11900	18400	1.14	94
HEMI-PCL$_{18.9k}$	165	166	18900	23400	1.19	90

[a]The polymerization was catalyzed by Sn(Oct)$_2$ in toluene at 120°C for 15 h;
[b]Molar ratio of monomer to initiator; [c]DP was calculated from ^{1}H NMR spectroscopy; [d]M_n was determined by ^{1}H NMR spectroscopy;
[e]M_n and PDI were determined by GPC analysis with linear polystyrene as standards; [f]Yields were determined by gravimetry

Table 2. Synthesis and characterization of amphiphilic diblock copolymers DEX-*b*-PCL

Polymer sample[a]	EDA-DEX[a]	HEMI-PCL[a]	M_n[b] [g/mol]	PDI[b]	f_{DEX}[c]	Yield[d] [%]
DEX$_{6.0k}$-*b*-PCL$_{7.5k}$	T6	HEMI-PCL$_{7.5k}$	17500	1.74	0.45	37
DEX$_{6.0k}$-*b*-PCL$_{9.2k}$	T6	HEMI-PCL$_{9.2k}$	20600	2.08	0.40	63
DEX$_{3.5k}$-*b*-PCL$_{7.5k}$	T3.5	HEMI-PCL$_{7.5k}$	17800	2.04	0.32	44
DEX$_{3.5k}$-*b*-PCL$_{9.2k}$	T3.5	HEMI-PCL$_{9.2k}$	18600	1.89	0.28	57
DEX$_{3.5k}$-*b*-PCL$_{11.9k}$	T3.5	HEMI-PCL$_{11.9k}$	24200	2.12	0.23	71
DEX$_{3.5k}$-*b*-PCL$_{18.9k}$	T3.5	HEMI-PCL$_{18.9k}$	31400	2.01	0.16	46

[a]Aza-Michael addition was carried out in DMSO at 70°C for 48 h;
[b]M_n and PDI were determined by GPC analysis with linear polystyrene as standards;
[c]The dextran mass fraction (f_{DEX}) was calculated by the molecular weight of dextran block divided by the molecular weight of DEX-*b*-PCL;
[d]Yields were determined by gravimetry

lengths were prepared firstly. For HEMI-PCL, desired chain length was attained by adjusting the ratio of ε-caprolactone to the initiator of HEMI. For EDA-DEX, dextran of two defined molecular weights, 3.5 and 6.0 kDa were used in terminal hydroxyl activation. The ^{1}H NMR spectra in Figure 2 represents one of the copolymers DEX$_{3.5k}$-*b*-PCL$_{9.2k}$, in which the molecular weight of PCL chain is 9.2 kDa (ε-caprolactone/HEMI = 80/1) and the molecular weight of dextran chain is 3.5 kDa.

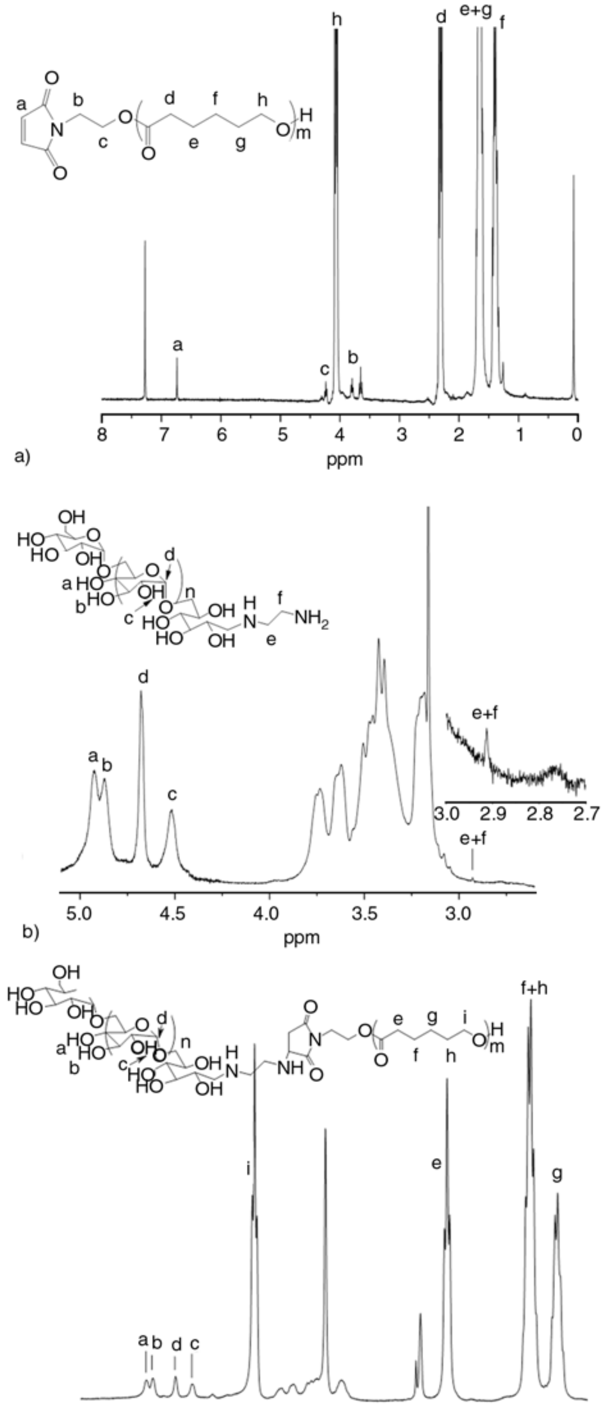

Figure 2. ^{1}H NMR spectra of (a) HEMI-PCL$_{9.2k}$ (solvent $CDCl_3$), (b) EDA-DEX$_{3.5k}$ (solvent DMSO-d_6) and (c) DEX$_{3.5k}$-*b*-PCL$_{9.2k}$ (solvent DMSO-d_6)

The chemical shifts at 6.74, 4.07 and 2.31 ppm in the ^{1}H NMR spectrum of HEMI-PCL (Figure 2a) are attributed to the characteristic proton signals of –C$\underline{H}$=C$\underline{H}$–, –C$\underline{H}_2$–O–C(O)– and –C(O)–C$\underline{H}_2$-, respectively. The chemical shifts of the alkane protons, –C–C$\underline{H}_2$C$\underline{H}_2$C$\underline{H}_2$–C–, are below 2.0 ppm. All the expected peaks from HEMI and PCL have been identified in the ^{1}H NMR spectrum shown in Figure 2a, indicating that the expected HEMI-PCL was formed. The degree of polymerization (DP) of the polymer is calculated from the ratio of the ^{1}H NMR peak areas at $\delta = 2.31$ ppm to that at $\delta = 6.74$ ppm. The results are listed in Table 1. These ratios are in agreement with the feed ratio of ε-CL to HEMI in reactants, indicating a high conversion. The polydispersity indices (PDI) of HEMI-PCL measured by GPC are listed in Table 1, which shows a narrow distribution in the range of 1.12–1.19. Therefore, the HEMI-PCL blocks of various chain lengths were successfully synthesized.

The formation of EDA-DEX, an amino-terminated dextran, was confirmed by the ^{1}H NMR spectrum shown in Figure 2b. The characteristic anomeric hydrogen of each dextran ring (–O–C$\underline{H}$–O–) is assigned to the chemical shift at $\delta = 4.67$ ppm (peak d), and the chemical shifts of the hydroxyl protons of dextran are divided to two groups at 4.87–4.92 ppm (peak a, b) and 4.52 ppm (peak c), respectively. The weak resonance peak (peak e+f) at $\delta = 2.92$ ppm is assigned to the methylene protons of ethylenediamine conjugated to the end of dextran, indicating the terminal reductive amination was reacted successfully. However, since the peak e+f is considerably less intensive as compared with those of the dextran sugar ring, we presume that amination of dextran was incomplete. The calculated conversion of dextran to EDA-DEX is approximately 15–31%, which was used to set up the next step of synthesis, conjugation of EDA-DEX with HEMI-PCL. There were extra amount of EDA-DEX (with consideration of un-conjugated dextran) in the reaction system to ensure sufficient yield of DEX-*b*-PCL. Un-conjugated dextran itself does not react with HEMI-PCL and could be removed in the purification process. The reasons for the limited conversion may be that only 0.024% of the terminal hydroxyls in dextran take the reactive free aldehyde form in a neutral solution under equilibrium due to the mutarotation phenomenon [22], and that the imine formation is a reversible and slow reaction which limited the overall reaction rate [41].

The last step of DEX-*b*-PCL synthesis, aza-Michael addition between the amino group at the end of EDA-DEX block and the maleimide group at the end of HEMI-PCL block, was rather straightforward. The reaction proceeded with EDA-DEX in extra at 70°C for 48 h under catalysis by TEA. Figure 2c shows the ^{1}H NMR spectrum of a block copolymer with given chain lengths, $\mathrm{DEX}_{3.5k}$-*b*-$\mathrm{PCL}_{9.2k}$. Both the peaks of PCL segment at 3.96, 2.45, 1.50, 1.27 ppm and those of dextran segment at 4.92, 4.86, 4.65, 3.0–3.8 ppm are identified. Moreover, the chemical shift of the maleimido protons at $\delta = 6.80$ ppm completely disappeared, indicating that the maleimido C=C double bonds of HEMI-PCL were all conjugated with the primary amine of EDA-DEX. These results verify the successful conjugation of EDA-DEX to the HEMI-PCL.

Based on these GPC curves of the DEX-*b*-PCL diblock copolymers (Figure 3), weight-average molecular weight (M_w) and number-average molecular weight (M_n) and polydispersity index (PDI) for each of the copolymers were obtained and summarized in Table 2. When the f_{DEX} of diblock copolymers decreased from 0.45 to 0.16, the curves gradually shift to a higher molecular weight region, and the peaks of DEX segment in NMR spectrum steadily decreased compared to those of PCL segment. In addition, the yield of the DEX-*b*-PCL product ranging from 37 to 71% is relatively low, which is probably due to the three times of purification with water. During this process, the excess dextran was removed but part of the DEX-*b*-PCL product may also be removed, especially for the copolymers with high f_{DEX} and thus with relatively large solubility in water. The lowest yield of the $\mathrm{DEX}_{6.0k}$-*b*-$\mathrm{PCL}_{7.5k}$ may be attributed to its highest f_{DEX}.

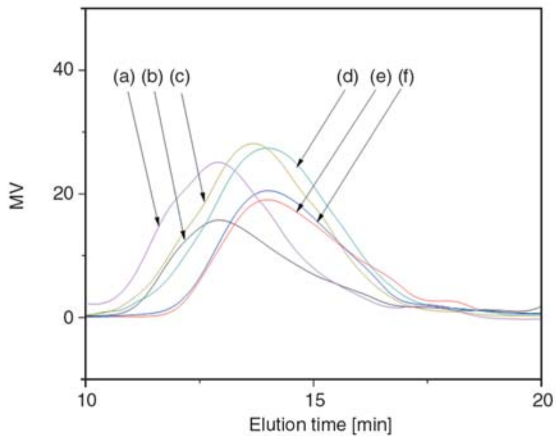

Figure 3. GPC curves of DEX-*b*-PCL diblock copolymers. (a) $\mathrm{DEX}_{3.5k}$-*b*-$\mathrm{PCL}_{18.9k}$, (b) $\mathrm{DEX}_{3.5k}$-*b*-$\mathrm{PCL}_{11.9k}$, (c) $\mathrm{DEX}_{6.0k}$-*b*-$\mathrm{PCL}_{9.2k}$, (d) $\mathrm{DEX}_{3.5k}$-*b*-$\mathrm{PCL}_{9.2k}$, (e) $\mathrm{DEX}_{3.5k}$-*b*-$\mathrm{PCL}_{7.5k}$, (f) $\mathrm{DEX}_{6.0k}$-*b*-$\mathrm{PCL}_{7.5k}$

3.2. Self-assembly of the amphiphilic diblock copolymers

We investigated the self-assembly of amphiphilic diblock copolymers DEX-*b*-PCL with different ratios of hydrophilic to hydrophobic block lengths in neutral aqueous solutions. It was shown, in previous studies, that micelles were made from dextran-PCL copolymer with $f_{DEX} = 0.57$ [27] and dextran-SS-PCL copolymer with $f_{DEX} = 0.66$ by solvent exchange method [31]. Based on the general empirical law proposed by Discher and Ahmed [11, 14], further decreasing the f_{DEX} of diblock copolymers might result in the formation of vesicles or inverted nanostructures. Therefore, in this study, a series of diblock copolymers with f_{DEX} in the range of 0.16 to 0.45 were used to investigate the effect of the relative hydrophilic block lengths on their self-assembly behaviors. All self-assembled aggregates in the study were prepared in PBS solution (pH 7.4, 0.01 M) by bulk hydration method, and the solution samples at a concentration of 0.5 mg·ml^{-1} were analyzed by TEM. For given dextran chain length, smaller f_{DEX} means larger hydrophobic block as well as larger overall molecular weight of the copolymer.

Figure 4 shows that the morphological forms of the block copolymers, DEX-*b*-PCL, change from spherical micelles, worm-like micelles to polymersomes by varying f_{DEX} from 0.45 to 0.16 correspondingly. At a high f_{DEX} (0.45), the copolymer ($\mathrm{DEX}_{6.0k}$-*b*-$\mathrm{PCL}_{7.5k}$) formed spherical micelles with diameters of 25±5 nm (Figure 4a, samples were not stained). As f_{DEX} decreased to the range of 0.40 and 0.32 ($\mathrm{DEX}_{6.0k}$-*b*-$\mathrm{PCL}_{9.2k}$ and $\mathrm{DEX}_{3.5k}$-*b*-$\mathrm{PCL}_{7.5k}$), worm-shaped micelles were formed together with spherical micelles (Figure 4b). The size of spherical micelles formed from $\mathrm{DEX}_{3.5k}$-*b*-$\mathrm{PCL}_{7.5k}$ ($f_{DEX} = 0.32$) was larger than those from

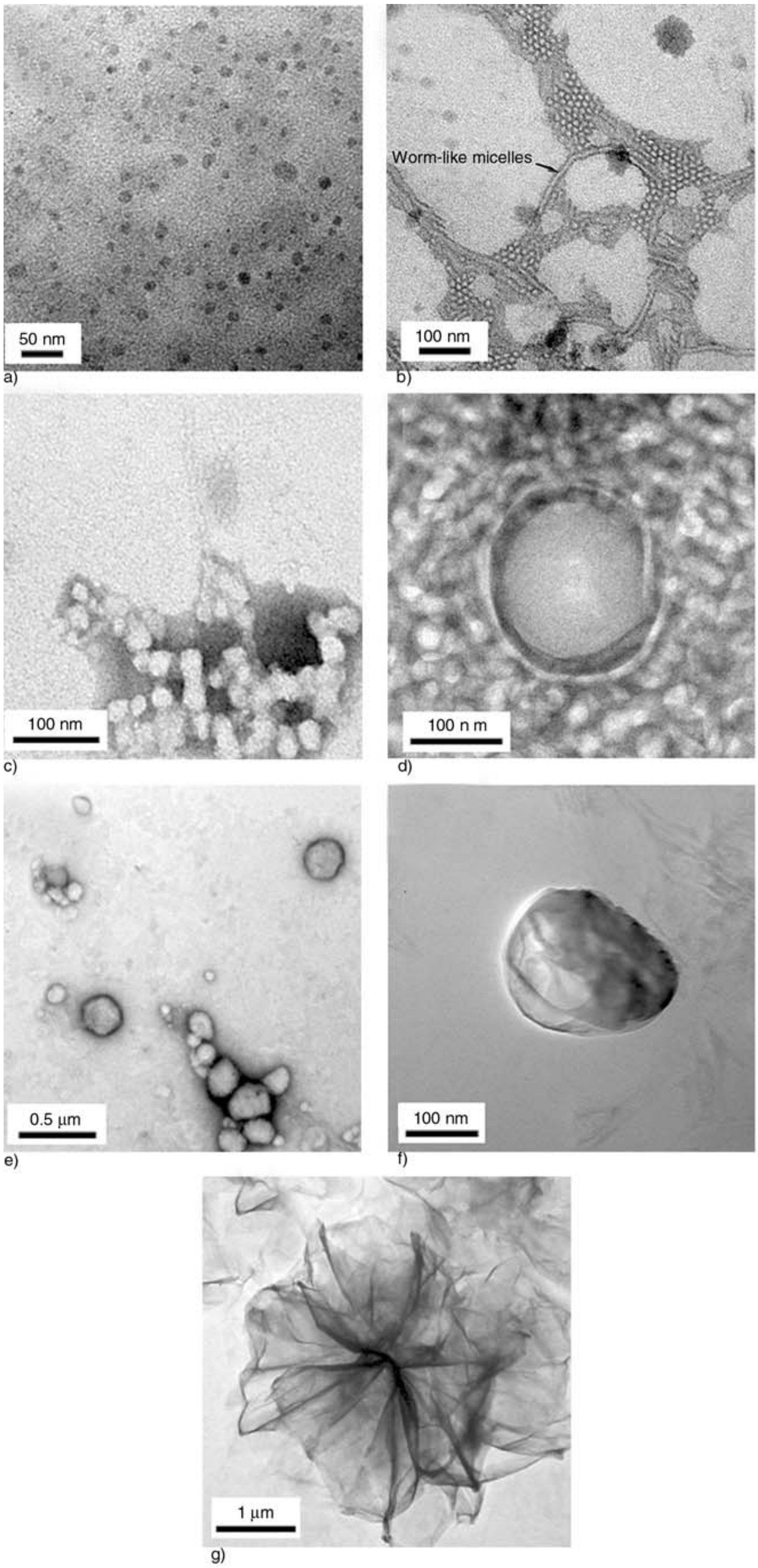

Figure 4. TEM images of structures formed by (a) DEX$_{6.0k}$-*b*-PCL$_{7.5k}$, (b) DEX$_{6.0k}$-*b*-PCL$_{9.2k}$, (c) DEX$_{3.5k}$-*b*-PCL$_{7.5k}$, (d) DEX$_{3.5k}$-*b*-PCL$_{9.2k}$, (e) DEX$_{3.5k}$-*b*-PCL$_{11.9k}$, (f) DEX$_{3.5k}$-*b*-PCL$_{11.9k}$ and (g) DEX$_{3.5k}$-*b*-PCL$_{18.9k}$ in aqueous media. The samples were negatively stained with phosphotungstic acid solution except for a, f and g.

$DEX_{6.0k}$-*b*-$PCL_{9.2k}$ ($f_{DEX} = 0.40$), with corresponding diameters of 40±5 and 30±5 nm, respectively (Figure 4b, 4c). As the f_{DEX} value further decreased to 0.28 and 0.23, the copolymers ($DEX_{3.5k}$-*b*-$PCL_{9.2k}$ and $DEX_{3.5k}$-*b*-$PCL_{11.9k}$) self-assembled to polymersomes 120±20 and 300±100 nm in diameters (Figure 4d, 4e, 4f), respectively. The interior of the aggregates has a pronouncedly lower electron density compared to the wall, suggesting vesicle morphology. The polymersomes shown in Figure 4e and Figure 4f were formed from the same diblock copolymer $DEX_{3.5k}$-*b*-$PCL_{11.9k}$, but differed in TEM sample preparation procedures by staining (Figure 4e) or not staining (Figure 4f) with phosphotungstic acid solution. Comparison of the two images suggests that staining may not be an essential treatment for imaging polymersomes under TEM. The wrinkles on the surface and the altered spherical shape of the particle in Figure 4f should be the result of polymersome shrinking due to dehydration.

Interestingly, the copolymer having larger hydrophobic block ($DEX_{3.5k}$-*b*-$PCL_{18.9k}$, $f_{DEX} = 0.16$) formed a large, flower-like structure (Figure 4g). The overall size of the 'flower' was 3.5±0.5 µm, considerably larger than the particulate forms assembled by less hydrophobic copolymers (Figure 4a–4f). Further increase in the hydrophobic chain length of the block copolymer ($DEX_{3.5k}$-*b*-$PCL_{40.0k}$, $f_{DEX} = 0.08$) lead to large, insoluble, and irregular particles (image not shown). It appeared that they were precipitated copolymers because the hydrophilicity was too low for the diblock copolymer to form stable aggregates in water.

For the observation of the flower-like structure formed by $DEX_{3.5k}$-*b*-$PCL_{18.9k}$ at $f_{DEX} = 0.16$, we speculate that they may be giant polymersomes by nature. This speculation was examined by loading a hydrophobic fluorescent dye, Nile red, into self-assembled solution of $DEX_{3.5k}$-*b*-$PCL_{18.9k}$, followed by observation under a fluorescent microscope (FM) without dehydration. The results, as shown in Figure 5, indicated that the block copolymer formed large polymersomes with diameters around 5.4±1.2 µm, supportive to the speculation that giant polymersomes were the precursor of the flower-like structure observed under TEM (Figure 4g). When a hydrated polymersome was dehydrated, its overall shape should be collapsed and rumpled to give a reduced size. In addition, Nile red was added to aggregates formed from $DEX_{3.5k}$-*b*-$PCL_{9.2k}$ and $DEX_{3.5k}$-*b*-$PCL_{11.9k}$, but no giant polymersomes were identified under FM.

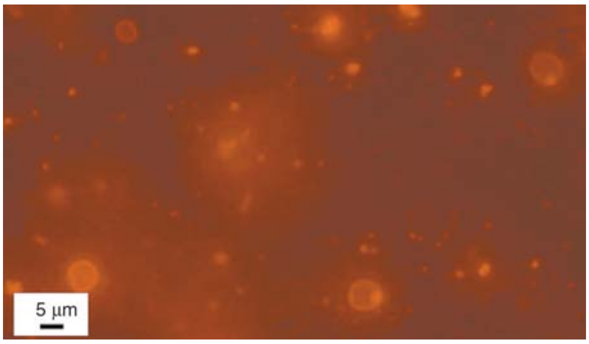

Figure 5. FM image of polymersomes formed by $DEX_{3.5k}$-*b*-$PCL_{18.9k}$ incorporated with nile red in aqueous media

$DEX_{3.5k}$-*b*-$PCL_{18.9k}$ at $f_{DEX} = 0.16$ can form polymersomes, which is out of the range of 0.25–0.42 and does not correspond to the theory of Discher. But it is in agreement with the reports of Houga, *et al.* [26] that polymersomes can be prepared by DEX-*b*-PS of $f_{DEX} = 0.08$. Due to the rod conformation of dextran with molecular weight below 2000 $g\cdot mol^{-1}$ [42] and the dextran T3.5 we used, most $DEX_{3.5k}$-*b*-PCL probably exhibit rod-coil conformation. Therefore, these results suggest that the rod-coil type diblock copolymers can form polymersomes at lower f_{DEX}.

As shown in Table 2, PDI of these copolymers ranges between 1.74 and 2.12. Although most amphiphilic block copolymers reported in literatures were of low polydispersities (i.e. PDI < 1.2) for studying their self-assembly behaviors [4, 7, 8, 43], our work indicate that a relatively high polydispersity does not preclude their efficient self-assembly into different morphologies. However, it should be pointed out that the PDI of hydrophilic block can affect the size of aggregates [44–46]. Previous investigations reported by Choucair *et al.* [44], who studied the influencing factors of poly(acrylic acid)-block-polystyrene (PAA-*b*-PS) vesicle size, suggested that increasing the PDI of copolymer favor the formation of smaller vesicles by preferential segregation of shorter hydrophilic chains (e.g. PAA) to the interior surface of the vesicle and longer chains to the exterior surface.

The size distributions of the diblock copolymer assemblies were also measured by DLS. Each DLS curve was analyzed by the Log Normal method, which featured as a population peak indicating the

Table 3. The self-assembly structures formed of diblock copolymers in aqueous solution and their diameters

Polymer sample	Diameter[a] [nm]	Diameter[b] [nm]	Structure[c]
$DEX_{6.0k}$-*b*-$PCL_{7.5k}$	45.3±2.7	25±5	Spherical micelle
$DEX_{6.0k}$-*b*-$PCL_{9.2k}$	49.0±3.6	30±5	Spherical micelle and rod-like micelle
$DEX_{3.5k}$-*b*-$PCL_{7.5k}$	75.9±8.3	40±5	Spherical micelle
$DEX_{3.5k}$-*b*-$PCL_{9.2k}$	195.9±15.2	120±20	Polymersome
$DEX_{3.5k}$-*b*-$PCL_{11.9k}$	381.3±32.7	300±100	Polymersome
$DEX_{3.5k}$-*b*-$PCL_{18.9k}$	5400±1200[d]	3500±500	Flower-like structure (Large polymersome[d])

[a]Diameter of self-assembly structure was measured by DLS;
[b]Diameter of self-assembly structure was measured by TEM; [c]Self-assembly structure was observed by TEM;
[d]The morphology and diameter of self-assembly structure of $DEX_{3.5k}$-*b*-$PCL_{18.9k}$ were determined by FM

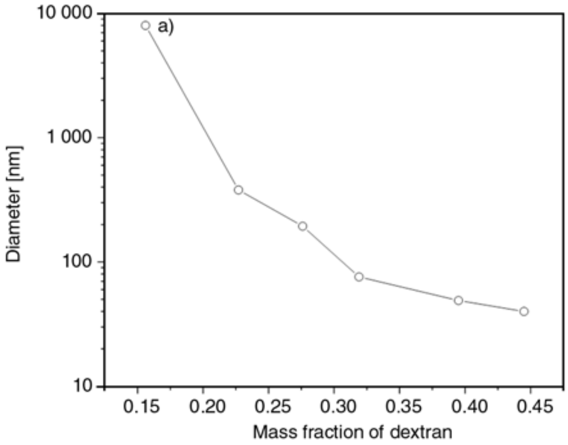

Figure 6. Plot of aggregate sizes determined by DLS vs. f_{DEX} of DEX-*b*-PCL diblock copolymers in aqueous media. [a]This size was determined by FM.

mean diameter. Table 3 shows the size distributions of the self-assembled aggregates ranged from 45.3 to 381.3 nm. The particle sizes of diblock copolymer assemblies were plotted against f_{DEX} of the copolymers in Figure 6, which shows a reversed correlation between the two factors. Table 3 lists the particle sizes and morphological forms of the assemblies of various DEX-*b*-PCL copolymers. In addition, the particle sizes measured by DLS were larger than those measured by TEM for each self-assembled aggregate, which can be attributed to the dehydration shrinkage of the particles during the TEM sample preparation.

4. Conclusions

Dextran and poly(ε-caprolactone) were conjugated together to prepare DEX-*b*-PCL diblock copolymer by aza-Michael addition under a mild condition. In order to achieve the end-to-end diblock conjugation, both DEX and PCL blocks were functionalized by modifying their terminal groups. Diblock copolymer, DEX-*b*-PCL, may self-assemble into particles of various morphological forms as a function of mass fraction of its hydrophilic block (f_{DEX}). As f_{DEX} decrease from 0.45 to 0.16, the copolymer assembled to spherical micelles, worm-like micelles, small polymersomes and giant polymersomes accordingly.

Acknowledgements

We thank the Analytical and Measured Center of Shanghai Jiao Tong University for technical support. This study was financially supported by the BioPharm Solutions, Inc., and partially supported by National Grand New Drug Program (No. 2009ZX09310-007).

References

[1] Su W., Han K., Luo Y., Wang Z., Li Y., Zhang Q.: Formation and photoresponsive properties of giant microvesicles assembled from azobenzene-containing amphiphilic diblock copolymers. Macromolecular Chemistry and Physics, **208**, 955–963 (2007).
DOI: 10.1002/macp.200600628

[2] Zhu Y. J., Tan Y. B., Du X.: Preparation and self-assembly behavior of polystyrene-block-poly (dimethylaminoethyl methacrylate) amphiphilic block copolymer using atom transfer radical polymerization. Express Polymer Letters, **2**, 214–225 (2008).
DOI: 10.3144/expresspolymlett.2008.26

[3] Lu X. J., Meng L. Z., Zhong X. X.: Novel fluorescent amphiphilic block copolymers: Photophysics behavior and interactions with DNA. Express Polymer Letters, **1**, 356–363 (2007).
DOI: 10.3144/expresspolymlett.2007.50

[4] Ghoroghchian P. P., Li G., Levine D. H., Davis K. P., Bates F. S., Hammer D. A., Therien M. J.: Bioresorbable vesicles formed through spontaneous self-assembly of amphiphilic poly(ethylene oxide)-*block*-polycaprolactone. Macromolecules, **39**, 1673–1675 (2006).
DOI: 10.1021/ma0519009

[5] Geng Y., Ahmed F., Bhasin N., Discher D. E.: Visualizing worm micelle dynamics and phase transitions of a charged diblock copolymer in water. Journal of Physical Chemistry B, **109**, 3772–3779 (2005).
DOI: 10.1021/jp0459559

[6] Discher B. M., Won Y-Y., Ege D. S., Lee J-C., Bates F. S., Discher D. E., Hammer D. A.: Polymersomes: Tough vesicles made from diblock copolymers. Science, **284**, 1143–1146 (1999).
DOI: 10.1126/science.284.5417.1143

[7] Liu F., Eisenberg A.: Preparation and pH triggered inversion of vesicles from poly(acrylic acid)-block-polystyrene-block-poly(4-vinyl pyridine). Journal of the American Chemical Society, **125**, 15059–15064 (2003).
DOI: 10.1021/ja038142r

[8] Schmitz C., Mourran A., Keul H., Möller M.: Synthesis and association behaviour of linear block copolymers with different microstructures but the same composition. Macromolecular Chemistry and Physics, **209**, 1859–1871 (2008).
DOI: 10.1002/macp.200800205

[9] Christian D. A., Cai S., Bowen D. M., Kim Y., Pajerowski J. D., Discher D. E.: Polymersome carriers: From self-assembly to siRNA and protein therapeutics. European Journal of Pharmaceutics and Biopharmaceutics, **71**, 463–474 (2009).
DOI: 10.1016/j.ejpb.2008.09.025

[10] Zhou W., Meng F., Engbers G. H. M., Feijen J.: Biodegradable polymersomes for targeted ultrasound imaging. Journal of Controlled Release, **116**, e62–e64 (2006).
DOI: 10.1016/j.jconrel.2006.09.051

[11] Discher D. E., Ahmed F.: Polymersomes. Annual Review of Biomedical Engineering, **8**, 323–341 (2006).
DOI: 10.1146/annurev.bioeng.8.061505.095838

[12] Pitsikalis M., Woodward J., Mays J. W., Hadjichristidis N.: Micellization of model graft copolymers in dilute solution. Macromolecules, **30**, 5384–5389 (1997).
DOI: 10.1021/ma970428r

[13] Rodríguez-Hernández J., Chécot F., Gnanou Y., Lecommandoux S.: Toward ‘smart’ nano-objects by self-assembly of block copolymers in solution. Progress in Polymer Science, **30**, 691–724 (2005).
DOI: 10.1016/j.progpolymsci.2005.04.002

[14] Ahmed F., Discher D. E.: Self-porating polymersomes of PEG-PLA and PEG-PCL: Hydrolysis-triggered controlled release vesicles. Journal of Controlled Release, **96**, 37–53 (2004).
DOI: 10.1016/j.jconrel.2003.12.021

[15] Meng F., Hiemstra C., Engbers G. H. M., Feijen J.: Biodegradable polymersomes. Macromolecules, **36**, 3004–3006 (2003).
DOI: 10.1021/ma034040+

[16] Zhou W., Feijen J.: Biodegradable polymersomes for controlled drug release. Journal of Controlled Release, **132**, e35–e36 (2008).
DOI: 10.1016/j.jconrel.2008.09.022

[17] Lin J. J., Silas J. A., Bermudez H., Milam V. T., Bates F. S., Hammer D. A.: The effect of polymer chain length and surface density on the adhesiveness of functionalized polymersomes. Langmuir, **20**, 5493–5500 (2004).
DOI: 10.1021/la036417a

[18] Kingshott P., Thissen H., Griesser H.: Effects of cloud-point grafting, chain length, and density of PEG layers on competitive adsorption of ocular proteins. Biomaterials, **23**, 2043–2056 (2002).
DOI: 10.1016/S0142-9612(01)00334-9

[19] McPherson T., Kidane A., Szleifer I., Park K.: Prevention of protein adsorption by tethered poly(ethylene oxide) layers: Experiments and single-chain mean-field analysis. Langmuir, **14**, 176–186 (1998).
DOI: 10.1021/la9706781

[20] Cismaru L., Hamaide T., Popa M.: Itaconic anhydride based amphiphilic copolymers: Synthesis, characterization and stabilization of carboxyl functionalized, PEGylated nanoparticles. European Polymer Journal, **43**, 4843–4851 (2007).
DOI: 10.1016/j.eurpolymj.2007.09.023

[21] Lee J. C-M., Bermudez H., Discher B. M., Sheehan M. A., Won Y-Y., Bates F. S., Discher D. E.: Preparation, stability, and in vitro performance of vesicles made with diblock copolymers. Biotechnology and Bioengineering, **73**, 135–145 (2001).
DOI: 10.1002/bit.1045

[22] Heinze T., Liebert T., Heublein B., Horning S.: Functional polymers based on dextran. Advances in Polymer Science, **205**, 199–291 (2006).
DOI: 10.1007/12_100

[23] Diamond A., Hsu J.: Protein partitioning in PEG/dextran aqueous two-phase systems. AICHE Journal, **36**, 1017–1024 (1990).
DOI: 10.1002/aic.690360707

[24] Lu Y., Chen S.: Micro and nano-fabrication of biodegradable polymers for drug delivery. Advanced Drug Delivery Reviews, **56**, 1621–1633 (2004).
DOI: 10.1016/j.addr.2004.05.002

[25] Goldberg D.: A review of the biodegradability and utility of poly(caprolactone). Journal of Polymers and the Environment, **3**, 61–67 (1995).
DOI: 10.1007/BF02067481

[26] Houga C., Giermanska J., Lecommandoux S., Borsali R., Taton D., Gnanou Y., Le Meins J-F.: Micelles and polymersomes obtained by self-assembly of dextran and polystyrene based block copolymers. Biomacromolecules, **10**, 32–40 (2009).
DOI: 10.1021/bm800778n

[27] Liu J-Y., Zhang L-M.: Preparation of a polysaccharide-polyester diblock copolymer and its micellar characteristics. Carbohydrate Polymers, **69**, 196–201 (2007).
DOI: 10.1016/j.carbpol.2006.09.009

[28] Schatz C., Louguet S., Le Meins J-F., Lecommandoux S.: Polysaccharide-*block*-polypeptide copolymer vesicles: Towards synthetic viral capsids. Angewandte Chemie International Edition, **48**, 2572–2575 (2009).
DOI: 10.1002/anie.200805895

[29] Hernandez O. S., Soliman G. M., Winnik F. M.: Synthesis, reactivity, and pH-responsive assembly of new double hydrophilic block copolymers of carboxymethyldextran and poly(ethylene glycol). Polymer, **48**, 921–930 (2007).
DOI: 10.1016/j.polymer.2006.12.036

[30] Yang Y. L., Kataoka K., Winnik F. M.: Synthesis of diblock copolymers consisting of hyaluronan and poly(2-ethyl-2-oxazoline). Macromolecules, **38**, 2043–2046 (2005).
DOI: 10.1021/ma047439m

[31] Sun H., Guo B., Li X., Cheng R., Meng F., Liu H., Zhong Z.: Shell-sheddable micelles based on dextran-SS-poly(ε-caprolactone) diblock copolymer for efficient intracellular release of doxorubicin. Biomacromolecules, **11**, 848–854 (2010).
DOI: 10.1021/bm1001069

[32] Bosker W. T. E., Ágoston K., Stuart M. A. C., Norde W., Timmermans J. W., Slaghek T. M.: Synthesis and interfacial behavior of polystyrene-polysaccharide diblock copolymers. Macromolecules, **36**, 1982–1987 (2003).
DOI: 10.1021/ma020925u

[33] Loos K., Stadler R.: Synthesis of amylose-block-polystyrene rod-coil *block* copolymers. Macromolecules, **30**, 7641–7643 (1997).
DOI: 10.1021/ma971022h

[34] Xu N., Lu F-Z., Du F-S., Li Z-C.: Synthesis of saccharide-terminated poly(ε-caprolactone) via Michael addition and 'click' chemistry. Macromolecular Chemistry and Physics, **208**, 730–738 (2007).
DOI: 10.1002/macp.200600533

[35] Kakuchi T., Narumi A., Miura Y., Matsuya S., Sugimoto N., Satoh T., Kaga H.: Glycoconjugated polymer. 4. Synthesis and aggregation property of well-defined end-functionalized polystyrene with β-cyclodextrin. Macromolecules, **36**, 3909–3913 (2003).
DOI: 10.1021/ma021295z

[36] Moreau M.: Method for the reductive amination of polysaccharides. U.S. Patent 6596861 B1, USA (2003).

[37] Mather B. D., Viswanathan K., Miller K. M., Long T. E.: Michael addition reactions in macromolecular design for emerging technologies. Progress in Polymer Science, **31**, 487–531 (2006).
DOI: 10.1016/j.progpolymsci.2006.03.001

[38] Xu N., Du F-S., Li Z-C.: Synthesis of poly(L-lysine)-*graft*-polyesters through Michael addition and their self-assemblies in aqueous solutions. Journal of Polymer Science Part A: Polymer Chemistry, **45**, 1889–1898 (2007).
DOI: 10.1002/pola.21949

[39] Mantovani G., Lecolley F., Tao L., Haddleton D. M., Clerx J., Cornelissen J., Velonia K.: Design and synthesis of *N*-maleimido-functionalized hydrophilic polymers via copper-mediated living radical polymerization: A suitable alternative to PEGylation chemistry. Journal of the American Chemical Society, **127**, 2966–2973 (2005).
DOI: 10.1021/ja0430999

[40] Zentz F., Valla A., Le Guillou R., Labia R., Mathot A-G., Sirot D.: Synthesis and antimicrobial activities of *N*-substituted imides. Il Farmaco, **57**, 421–426 (2002).
DOI: 10.1016/S0014-827X(02)01217-X

[41] Borch R. F., Bernstein M. D., Durst H. D.: Cyanohydridoborate anion as a selective reducing agent. Journal of the American Chemical Society, **93**, 2897–2904 (1971).
DOI: 10.1021/ja00741a013

[42] Gekko K.: Solution properties of dextran and its ionic derivatives. in 'Solution properties of polysaccharides' (ed.: Brant D. A.) ACS Publications, Washington, Vol 150, 415–438 (1981).
DOI: 10.1021/bk-1981-0150.ch029

[43] Sun J., Shi Q., Chen X., Guo J., Jing X.: Self-assembly of a hydrophobic polypeptide containing a short hydrophilic middle segment: Vesicles to large compound micelles. Macromolecular Chemistry and Physics, **209**, 1129–1136 (2008).
DOI: 10.1002/macp.200800018

[44] Choucair A., Lavigueur C., Eisenberg A.: Polystyrene-*b*-poly(acrylic acid) vesicle size control using solution properties and hydrophilic block length. Langmuir, **20**, 3894–3900 (2004).
DOI: 10.1021/la035924p

[45] Terreau O., Luo L., Eisenberg A.: Effect of poly (acrylic acid) block length distribution on polystyrene-*b*-poly(acrylic acid) aggregates in solution. 1. Vesicles. Langmuir, **19**, 5601–5607 (2003).
DOI: 10.1021/la0269715

[46] Luo L., Eisenberg A.: Thermodynamic stabilization mechanism of block copolymer vesicles. Journal of the American Chemical Society, **123**, 1012–1013 (2001).
DOI: 10.1021/ja005824v

eXPRESS Polymer Letters Vol.4, No.10 (2010) 611–620
Available online at www.expresspolymlett.com
DOI: 10.3144/expresspolymlett.2010.76

Polypropylene/calcium carbonate nanocomposites – effects of processing techniques and maleated polypropylene compatibiliser

M. Y. A. Fuad[1*], *H. Hanim*[1], *R. Zarina*[1], *Z. A. Mohd. Ishak*[2], *Azman Hassan*[3]

[1]Plastics Technology Group, Advanced Materials Research Centre, SIRIM Berhad, P.O. Box 7035, 40911 Shah Alam, Malaysia
[2]School of Materials and Mineral Resources Engineering, Engineering Campus, Universiti Sains Malaysia, Seri Ampangan, 14300 Nibong Tebal, Penang, Malaysia
[3]Faculty of Chemical and Natural Resources Engineering, Universiti Teknologi Malaysia, Skudai, Johor, Malaysia

Received 8 April 2010; accepted in revised form 17 June 2010

Abstract. The mechanical properties and crystalline characteristics of polypropylene (PP) and nano precipitated calcium carbonate (NPCC) nanocomposites prepared via melt mixing in an internal mixer and melt extrusion in a twin screw extruder, were compared. The effect of maleic anhydride grafted PP (PP-g-MAH) as a compatibiliser was also studied using the internal mixer. At low filler concentration of 5 wt%, impact strength was better for the nanocomposites produced using the internal mixer. At higher filler loading of more than 10 wt%, the extrusion technique was more effective to disperse the nanofillers resulting in better impact properties. The impact results are consistent with the observations made from Scanning Electron Microscope (SEM) morphology study. As expected, the flexural modulus of the nanocomposites increased with filler concentration regardless of the techniques utilised. At a same filler loading, there was also no significant difference in the moduli for the two techniques. The tensile strength of the mixed nanocomposites were found to be inferior to the extruded nanocomposites. Introduction of PP-g-MAH improved the impact strength, tensile strength and modulus of the mixed nanocomposites. The improvements may be attributed to better interfacial adhesion, as evident from the SEM micrographs which displayed better dispersion of the NPCC in the presence of the compatibiliser. Though NPCC particles have weak nucleating effect on the crystallization of the PP, addition of PP-g-MAH into the mixed nanocomposites has induced significant crystallization of the PP.

Keywords: *nanocomposites, polypropylene, mechanical properties, nano-sized calcium carbonate, melt compounding*

1. Introduction

The development of polymer nanocomposites (PNCs) can be regarded as a significant technological advancement in the plastics industry over the past few years. PNCs are formed from blends of nanometer sized fillers with either thermoplastics or thermosetting polymers. Numerous benefits of PNCs have been described which include improvements in mechanical properties, barrier properties, heat resistance, dimensional stability and flame retardancy [1–4]. There are many types of nano-sized fillers being used among which include nanofibres such as carbon nanotubes or cellulose whiskers, nanoplatelets such as layered silicate and nano-sized isotropic particles such as silica or calcium carbonate ($CaCO_3$) [5–8].

$CaCO_3$ is one of the most commonly used fillers in thermoplastics, especially polyolefins. It is inexpensive and can be used at high loadings. Originally used as a cheap extender, fine grades of

---

[*]Corresponding author, e-mail: fuad@sirim.my

precipitated $CaCO_3$ is now being produced in nanometer size and this nano precipitated $CaCO_3$ (NPCC) has the potential to be an important functional filler in polypropylene composites [9–12]. The surface of the NPCC filler is usually treated with fatty acids such as stearic acid, to modify the filler surface to become hydrophobic. The main purpose for this surface coating is to reduce moisture absorption and hence particle agglomeration during storage, as well as to improve dispersibility of the polar filler when incorporated into non-polar polymer melts [13]. Improved dispersion of the nanofillers within the polymer matrix is a prerequisite for any improvement in mechanical properties, particularly impact strength.

Polypropylene (PP) is a very versatile and adaptable polymer whereby its properties can readily be enhanced with the inclusion of various types of fillers. The advantages gained in price/volume/performance relations have resulted in PP composites successfully penetrating fields traditionally occupied by other engineering materials [14]. Generally, the properties of particle-filled PP are strongly dependent on the characteristics of the filler particles. Due to its non-polar chemical structure, PP interacts poorly with the typically polar fillers such as $CaCO_3$, and optimum dispersion is normally difficult to achieve. Compatibilisers are frequently used to improve the interfacial adhesion between $CaCO_3$ and PP, in order to gain the envisaged enhancement in mechanical properties. Bi-functional molecules such as maleic-anhydride grafted PP (PP-g-MAH) are commonly used as a compatibilisers for PP and $CaCO_3$ [15, 16].

Besides filler surface modification and addition of suitable compatibilisers, the choice of processing techniques also plays an important role to achieve the desired improvement in the properties of interest. The efficiency of the processing techniques to disperse the fillers becomes critical, especially with nanofillers which have very strong tendency to agglomerate due to their high surface energies. The two common melt-processing techniques employed to produce nanocomposites are melt mixing using an internal mixer and melt extrusion using a twin screw extruder. Compared to an internal mixer, a twin screw extruder is more convenient to compound nanocomposites in larger quantity and continuous process. It has been reported nanocomposites of PP with nano-sized $CaCO_3$ have been successfully prepared via melt mixing by Chan *et al.* [17]. The good filler dispersion obtained using the internal mixer has resulted in significant improvements in modulus and impact strength with only a slight lowering of the tensile strength.

Wang *et al.* [18] used three kinds of compatibilizers to study the effect of interfacial interaction on the crystallization and mechanical properties of polypropylene (PP)/nano-$CaCO_3$ composites. The compatibilizers were PP grafted with maleic anhydride (PP-g-MA), ethylene-octene copolymer grafted with MA (POE-g-MA), and ethylene-vinyl acetate copolymer grafted with MA (EVA-g-MA). They noted that only the former compatibilizer resulted in significant improvement the dispersion of nano-$CaCO_3$ particles, favoured the nucleation effect of nano-$CaCO_3$, increased the tensile strength and modulus. The ductility and impact strength of composites were however compromised as trade-off to the improvement of the other mechanical properties.

The objective of this study is to compare the properties of PP filled with NPCC prepared via two different routes viz. melt mixing in an internal mixer and melt extrusion in a twin screw extruder. The mechanical properties of the nanocomposites are evaluated using impact, flexural and tensile tests. Thermal and crystallisation characteristics are analysed using a Differential Scanning Calorimeter (DSC) while filler dispersion is observed using a Scanning Electron Microscope (SEM). In addition, the effect of adding PP-g-MAH as a compatibiliser for the PP/NPCC nanocomposites is also studied using the internal mixer.

2. Experimental

2.1. Materials and sample preparation

The grade of PP used was Titanpro 6331 produced by Titan Polymers Malaysia Sdn. Bhd (Kuala Lumpur, Malaysia). The homoploymer PP has a density of 0.899 g/cm^3 and a melt flow rate of 14 g/10 minutes (2.16 kg at 230°C). The nano calcium carbonate used was NPCC 201 supplied by NanoMaterials Pty. Ltd. The stearic acid coated nanofiller has a measured average primary particle size of about 50 nm. The grade of PP-g-MAH added as a compatibiliser was Orevac CA 100 from

Atofina, with a maleic anhydride content of 1%. The anti-oxidant used was Irganox 1010 from Ciba Specialty Chemicals Inc.

The NPCC and PP-g-MAH were dried in a vacuum oven at 80°C for at least 2 hours and allowed to cool down to room temperature in a desiccator prior to use. For the melt extrusion technique, the PP/NPCC was compounded in a Berstoff (ZE-25) co-rotating twin-screw extruder ($L/D = 33$) with a barrel temperature profile ranging from 180°C near the hopper to 200°C at the die and a screw speed of 150 rpm (rotation per minute). NPCC powder at 5, 10 and 15 wt% loadings and the anti-oxidant at 1 wt% of total compound weight were added into the molten PP via a secondary side feeder. Since the extruder is primarily designed to compound micron size fillers, the nanocomposites were compounded twice to improve and ensure homogeneous mixing. The estimated total residence time for the nanocomposites during the melt extrusion process was about 8 minutes since the nanocomposites were compounded twice by extruder.

For the melt mixing technique, mixing was carried out in batches using a Haake Rheomix 3000p internal mixer with a mixing temperature of 180°C and a rotor speed of 60 rpm. The PP and antioxidant were first mixed for 5 minutes before the NPCC at 5, 10 and 15 wt% was added slowly into the mixing chamber over a period of 10 minutes. Mixing was continued for a further 5 minutes and the homogeneous mixture was discharged from the internal mixer and later reduced into small pieces using a crusher. For the experiments using compatibiliser, the PP-g-MAH was added at a fixed amount of 10 wt% into the mixing chamber together with the PP and the anti-oxidant. The total residence time of the mixing process was 20 minutes.

The crushed pellets from the melt mixing technique and the pelletised extrudates from the melt extrusion technique were injection moulded into ISO multi-purpose test specimens using an Arburg 75 tonne injection moulding machine at 190°C melt temperature and 40°C mould temperature.

2.2. NPCC filler content and filler dispersion

The actual amount of filler present in the nanocomposites was determined using a thermogravimetric analyser (TGA). The analysis was performed on the samples using a Mettler Toledo TGA 851. The samples, obtained from the gate-section, mid-section and end-section of the tensile dumbell specimen, were heated from 25 to 550°C in an inert atmosphere of nitrogen at a heating rate of 20°C/min. The average amount of NPCC which remained at the end of the TGA scan were obtained from the thermograms to compare the amount of filler added and the actual amount present in the tested specimens.

The filler dispersion in the nanocomposites was examined using a Hitachi S-2500 Scanning Electron Microscope (SEM). The impact fractured specimens were coated with gold prior to examination under the electron beam. An operating voltage of 10 kV and a magnification of 5000 times were used. The average size of the dispersed NPCC filler was measured on the micrographs using the Roentec ScanVision software.

2.3. Mechanical properties evaluation

Tensile properties were determined using an Instron 5556 Universal Testing Machine in accordance to ISO-527-1. The crosshead speed used for the modulus and tensile strength determination were 1 and 50 mm/min. respectively. Flexural properties were also measured using the same machine in accordance to ISO 178 at a crosshead speed of 2 mm/min. The notched Izod impact strength was determined using a CEAST Resil Impactor according to ISO 180 at ambient temperature. All test specimens were conditioned in accordance to ISO 291 at 25 ± 2°C and 55 ± 5% relative humidity for at least 16 hours before being tested.

To calculate the predicted modulus of composites, the weight fraction is converted to the volume fraction indicated in Equation (1):

$$\phi_f = \frac{\rho_c}{\rho_f} W_m \qquad (1)$$

where ϕ_f is filler volume fraction, ρ_c is density of composite, ρ_f is density of filler and W_m is filler weight fraction.

2.4. Thermal and crystallisation studies

The melting and crystallisation behaviour of the nanocomposites were studied using a Mettler Toledo Differential Scanning Calorimeter (DSC 822e). About 10 mg of each sample was scanned from 25 to 250°C at a heating rate of 20°C per minute in an inert atmosphere of nitrogen (N_2). The N_2 flow rate was set at 50 ml/min. The samples were then annealed at 250°C for 5 minutes before being cooled to 50°C at a cooling rate of 20°C per minute. A second heating scan was performed on the cooled samples using the same parameters as the first heating cycle. The peak melting temperature (T_m) and the enthalpy of fusion (ΔH) for the nanocomposites were obtained from the second heating curve while the peak crystallisation temperature (T_c) was taken from the crystallisation curve. The relative crystallinity was calculated from the enthalpy value, ΔH and the enthalpy value for a theoretically 100% crystalline PP, taken as 209 J/g [19].

3. Results and discussions

3.1. NPCC filler content and dispersion

The TGA results for the nanocomposites are given in Table 1. From the Table, the amount of NPCC measured on the specimens was also found to be close to the actual amount added during compounding and mixing.

The evaluation of filler dispersion is important as only well dispersed nanoparticles can lead to the expected improvement in mechanical properties. For the nanocomposites to possess good impact toughness, it is critical that the filler dispersion in the polymer matrix be very uniform to avoid creation of crack-initiating large agglomerates [20].

Figures 1a, 1b show the SEM micrographs of the impact-fractured surface of the nanocomposites prepared via the extruder while Figures 1 c, 1d are nanocomposites prepared via the internal mixer. At low NPCC content, the number of large agglomerates appeared more in the nanocomposites prepared via extrusion compared to that prepared via mixing. At higher NPCC levels, the reverse phenomenon was observed where the nanocomposites prepared by mixer have larger agglomerates compared to the extruded nanocomposites. One possible reason for this observation is that at high filler concentration, the interparticle distance between the nanofillers becomes smaller, leading to flocculation of the NPCC nanoparticles after the mixing process in the internal mixer is stopped [16]. Thus, in this study, that melt extrusion appears to be a better technique for dispersing nanofiller when the filler concentration used is high, while the internal mixer is effective for preparing nanocomposites with low filler content.

Figures 1e, 1f shows the filler dispersion of the nanocomposites prepared using the internal mixer with 10 wt% of PP-g-MAH added as a compatibiliser. Overall, better filler dispersion was observed in the presence of PP-g-MAH, especially at low NPCC. With PP-g-MAH, the NPCC particles appeared more encapsulated within the PP matrix, indicating that better interfacial adhesion has possibly been established between the filler and the polymer phase with the aid of the compatibiliser. Without the compatibiliser, the NPCC in the micrographs appeared more as discrete particles within the PP matrix, as shown in Figures 1c, 1d. Nevertheless, for both techniques used and even with the addition of compatibiliser, the average particle size of NPCC particles measured from the SEM micrographs were still much larger than the average primary particle size of the NPCC used in this study.

3.2. Mechanical properties

Figure 2 shows the effect of NPCC content on the notched Izod impact strength of the nanocomposites prepared using the internal mixing and extruder. It can be seen that for both techniques, the addition of NPCC increased the impact strength of the neat PP. However, there is a difference in the trend of increment for the two techniques. At low NPCC loading of 5 wt%, greater increment was observed for the nanocomposites prepared via the mixer when compared to the extruder. The mixed nanocomposites appear to have smaller agglomerates, resulting in better impact improvement when compared to the composites made by melt extrusion. Nevertheless, further increase in the filler content

Table 1. TGA results of PP nanocomposites

Sample composition [wt% PP/NPCC]	NPCC content [weight%]		
	Melt extrusion	Melt mixing	Melt mixing with 10 wt% PP-g-MAH
95/5	4.6	4.7	4.9
90/10	9.7	9.4	9.3
85/15	14.0	14.1	14.7

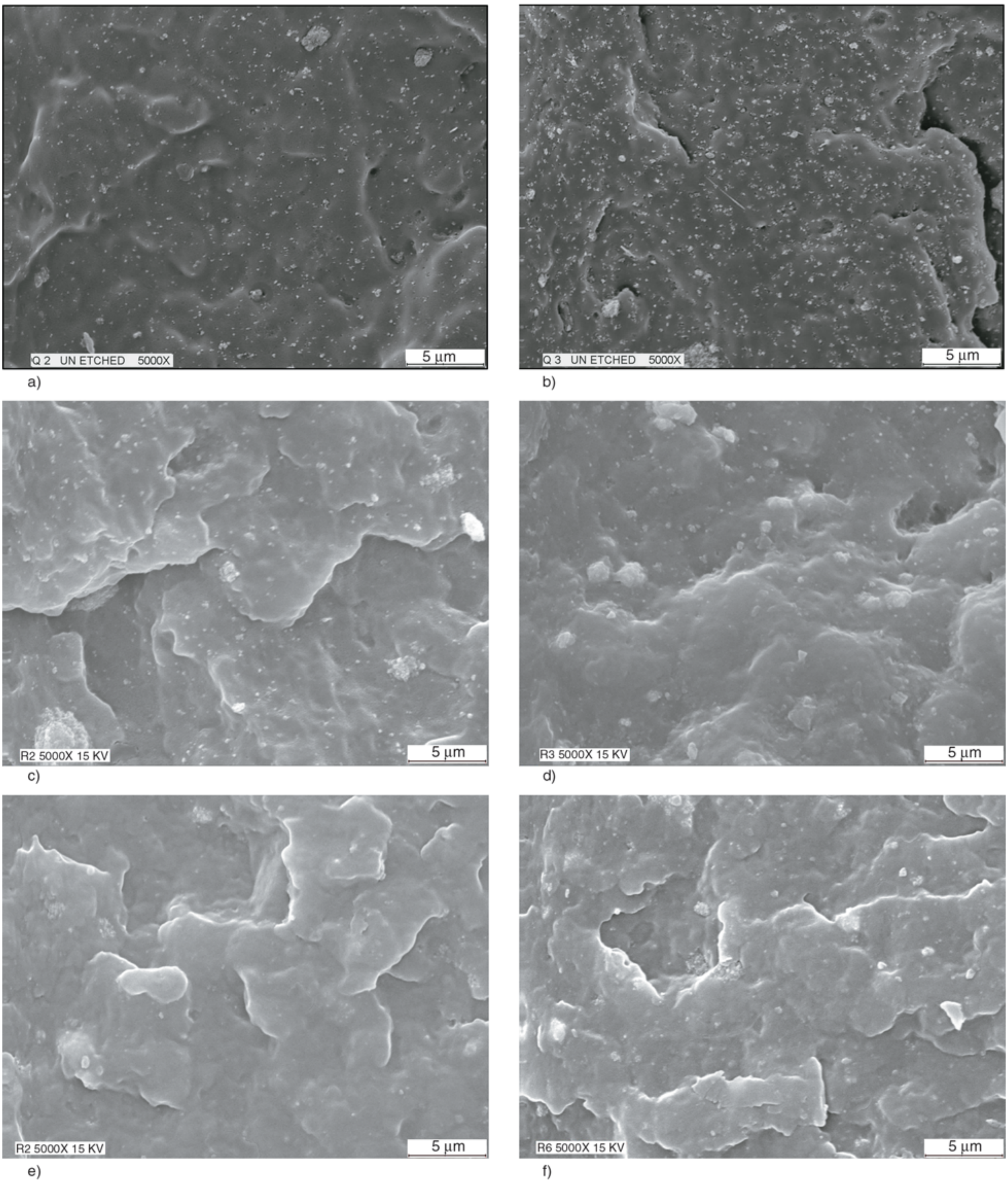

Figure 1. SEM micrographs of (a) 90PP/10NPCC and (b) 85PP/15NPCC prepared using melt extrusion technique; (c) 90PP/10NPCC and (d) 85PP/15NPCC prepared using melt mixing technique and (e) 90PP/10NPCC and (f) 85PP/15NPCC prepared using melt mixing technique with 10 wt% PP-g-MAH as compatibiliser

for the mixed nanocomposites caused no significant changes to the impact strength. For the extruded nanocomposites, increased in impact strength was observed until addition of up to 10 wt% of NPCC with no further improvement observed thereafter. The result of the impact strength is consistent with the SEM micrographs results shown earlier in Figures 1a–1d).

It can also be seen that addition of PP-g-MAH has improved the impact strength of PP at all filler loadings. However, the same trend is observed whereby after filler loading of 5 wt%, the impact

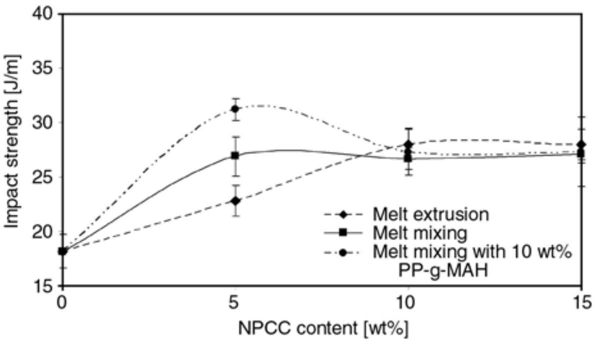

Figure 2. Effect of NPCC and preparation techniques on the impact strength of nanocomposites

strength drops, even in the presence of the compatibiliser. As indicated earlier, at higher concentrations, the mixer does no longer provide effective mixing, thus the addition of the compatibizer does not improve the impact strength. The SEM micrographs as shown in Figures 1e, 1f support the impact results. At higher filler loading, the number of large agglomerates was more apparent and thus contributing to the lowering of the impact strength. The effect of NPCC on the flexural modulus of the mixed and extruded nanocomposites is shown in Figure 3. Predictably, the stiffness of PP increased gradually with increasing filler weight fraction. There also appears to be no significant difference between the flexural modulus of the nanocomposites prepared using the two different techniques, indicating that the modulus of the nanocomposites is not significantly affected by the presence of filler agglomerates. Presence of PP-g-MAH in the mixed nanocomposites has also significantly improved the modulus further, This may be attributed to the improved interfacial adhesion between the filler particles and the PP matrix.

The effect of NPCC on the tensile strength of the nanocomposites prepared via mixing and extrusion is shown in Figure 4. In general, the tensile strength of the nanocomposites prepared by both techniques decreases with increasing amount of NPCC and from among the two techniques, the drop in tensile strength was higher for the mixed nanocomposites compared to the extruded nanocomposites. In the presence of the 10 wt% PP-g-MAH as a compatibiliser, the tensile strength of the nanocomposites did not deteriorate with increasing NPCC concentration. According to Liang [24], the strength of particulate-filled polymer composites depends, to a great extent, on the interfacial adhesion between the matrix and the filler which will facilitate the transfer of a small section of stress to the filler particle during deformation.

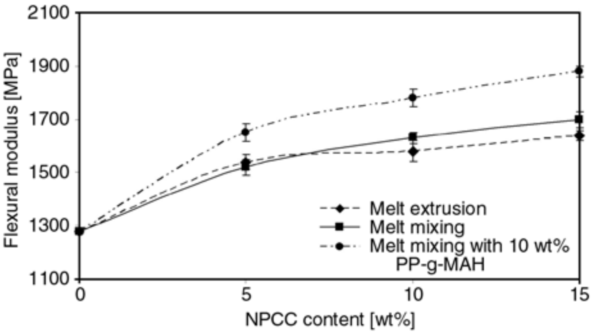

Figure 3. Effect of NPCC and preparation techniques on the flexural modulus of nanocomposites

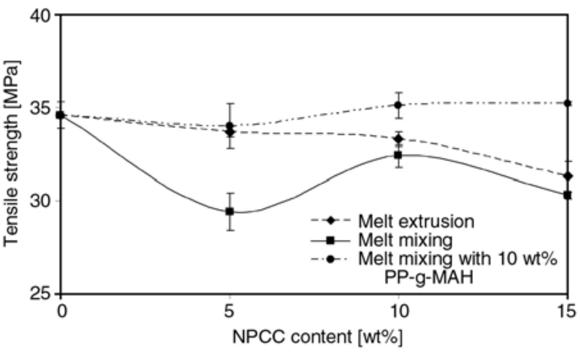

Figure 4. Effect of NPCC and preparation techniques on the tensile strength of nanocomposites

An equation which is commonly used to predict the modulus of composites containing a certain amount of spherical fillers developed by Guth [22] is shown as Equation (2):

$$E_c = E_m(1 + 2.5\phi_f + 14.1\phi_f^2) \tag{2}$$

where E_c is the Young's modulus of the composite, E_m is the matrix Young's modulus and ϕ_f is the volume fraction of the filler. It has been reported that Equation (1) is only applicable to composites filled with a certain amount of spherical fillers. If the filler concentration is higher than 10 vol%, the modulus increases much more rapidly than Equation (2) would predict, attributed to the formation of a network by the spherical filler chains [23]. The modulus of particle-filled composites may also be predicted using Equations (3) or (4) [18]:

$$E_c = E_p\phi_p + E_f\phi_f \tag{3}$$

$$E_c = \frac{E_pE_f}{E_p\phi_f + E_f\phi_p} \tag{4}$$

where E_c is the modulus of the composites, E_p and E_f are the moduli of the polymer matrix and the filler respectively, ϕ_p and ϕ_f are the volume fraction of the polymer and filler respectively. Equation (3), based on the rule of mixtures, is appropriate when strong adhesion exists between the filler and the polymer and the filler has a large aspect ratio. Equation (4), the inverse rule of mixtures equation, is applicable to rigid spherical particles.

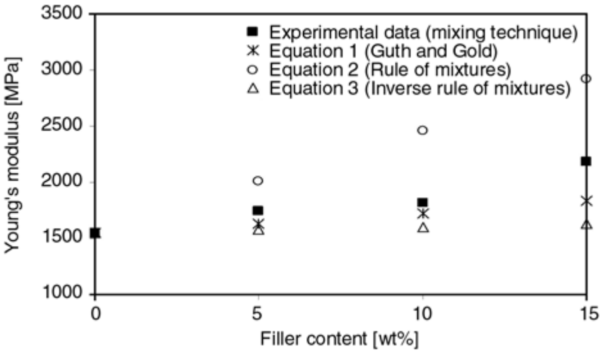

Figure 5. The calculated (theoretical) and measured (experimental) moduli of PP/NPCC nanocomposites prepared via melt extrusion as a function of filler content. Note: The modulus of NPCC is taken as 26 GPa [16].

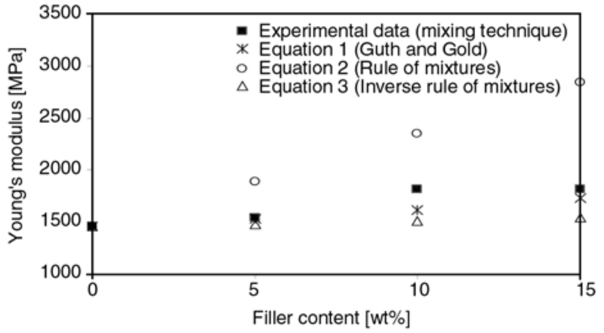

Figure 6. The calculated (theoretical) and measured (experimental)moduli of PP/NPCC nanocomposites prepared via melt mixing as a function of filler content

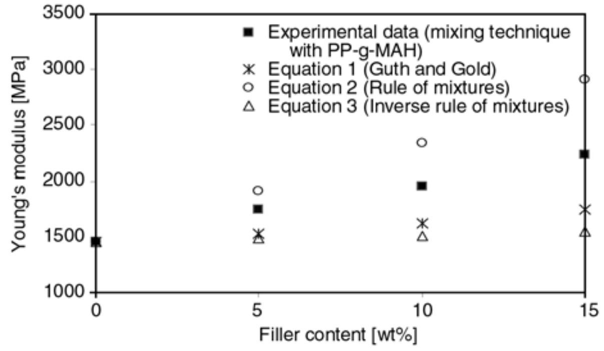

Figure 7. The calculated (theoretical) and measured (experimental) moduli of PP/NPCC nanocomposites prepared via melt mixing with PP-g-MAH as a function of filler content

Figures 5–7 illustrate the experimental and calculated modulus based on the above equations for the extruded, mixed and mixed with PP-g-MAH nanocomposites, respectively. It can be seen from Figure 5 that the experimental moduli of the extruded nanocomposites agree quite well with Equations (2) and (4) up till a filler content of 10 wt%. Equation (3) was found to be the most inaccurate to predict the moduli of the nanocomposites, indicating that the law of mixtures is invalid in this case as the equation is only applicable when the filler has a large aspect ratio and there is a strong bonding between the matrix and the filler. A similar observation is made for the mixed nanocomposites in Figure 6, where the experimental plots closely follow Equations (2) and (4), and deviate from Equation (3). However, it is interesting to note that the experimental moduli of the mixed nanocomposites still follow Equations (2) and (3) even at high filler loadings of 15 wt%. For the mixed nanocomposites with PP-g-MAH, the experimental moduli, as shown in 8, were found to deviate from Equations (2) and (4) and showed tendency to move towards Eqquation (3). These results indicate that better adhesion has occurred between the NPCC and the PP matrix, as Equation (3) is appropriate when strong adhesion exist between the filler and the polymer.

3.3. Thermal and crystallisation behaviour

The DSC melting curves for the nanocomposites are shown in Figures 8a–8c, and their corresponding melting temperatures (T_m) are listed in Table 2. From the DSC curves, the T_m of the neat PP was found to be 163°C while the T_m of the nanocomposites ranged from 161 to 164°C. Thus, incorporation of NPCC did not result in a significant shift in the T_m of PP, as the small variation of observed is within the experimental error of the instrument used.

However, it is interesting to note that the DSC curves for PP filled with 10 and 15 wt% of NPCC prepared with PP-g-MAH using the internal mixer displayed a small melting depression at about 150°C. This small endothermic transition is possibly associated with the melting of the β-phase crystallites of PP [17, 25, 26]. PP is a polymorphic

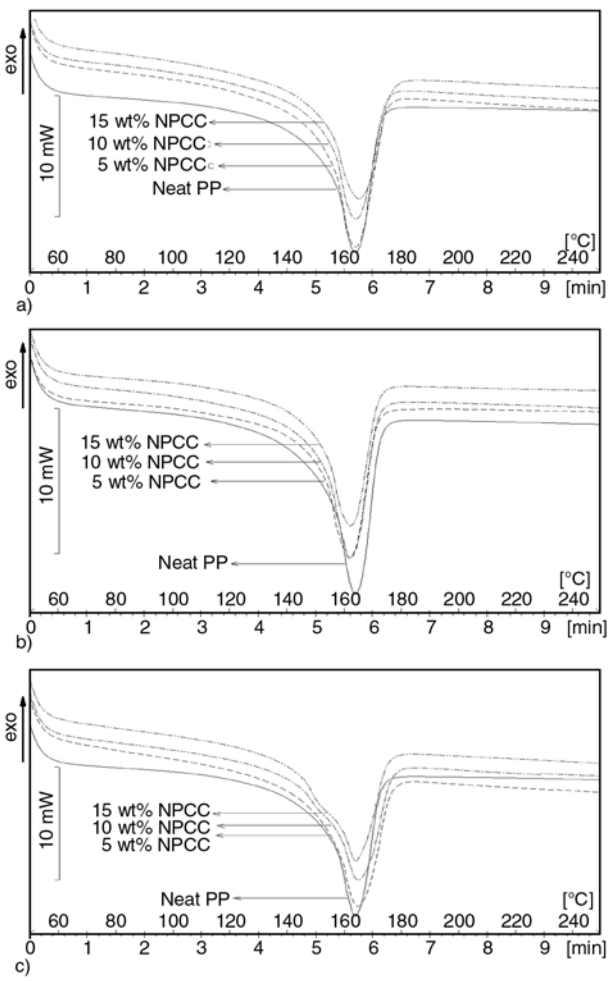

Figure 8. DSC melting curves for nanocomposites prepared via (a) melt extrusion, (b) melt mixing and (c) melt mixing with 10 wt% PP-g-MAH compatibiliser

material and is capable of crystallising in three different crystal forms; the α, or monoclinic form, the β, or pseudo-hexagonal form, and the γ, or triclinic form. The most stable and prevalent form is the α-phase. This phase, which melts at around 160°C, is the main crystalline structure formed under normal processing conditions while the β-phase is obtained if the melt undergoes high shear forces during processing [26]. The β-phase PP could also be formed in the presence of nucleating agents. Thus, the PP-g-MAH compatibiliser has possibly improved the nucleating activity of the NPCC and hence promoting the formation of the β-phase PP, which was not present in the mixed compound prepared without the compatibiliser.

Results of the enthalpy of fusion (ΔH) obtained from the melting curves for the PP and the nanocomposites are listed in Table 2. It should be noted that the ΔH values shown have been corrected for filler content, thus expressed in J/g polymer (PP). The relative crystallinity of the nanocomposites were then calculated using the ΔH values, taking 209 J/g as the theoretical enthalpy value for a 100% crystalline PP [19]. Overall, it is observed that the crystallinity of PP is not appreciably affected by the addition of the NPCC filler, as the ±2% variation in the crystallinity values observed is within the experimental error of the instrument used.

The DSC crystallisation curves for PP and the nanocomposites are shown in Figures 9a–9c and the peak crystallisation temperature (T_c) values are listed in Table 2. For the nanocomposites prepared via extrusion and mixing without the presence of PP-g-MAH as compatibiliser, there appears to be minimal shift in the T_c, indicating again the weak nucleating effect of NPCC particles on the crystallisation of PP. However, addition of PP-g-MAH into the mixed nanocomposites has induced crystallisation of PP to occur at higher temperatures resulting in higher T_c. Thus, these DSC results suggest that PP-g-MAH has improved the nucleation

Table 2. DSC results for the nanocomposites

Sample composition [wt% PP/NPCC]	Melting temperature, T_m [°C]	Enthalpy of fusion corrected for filler content, ΔH_c [J/g PP]	Percentage crystallinity, X_c [%]	Crystallisation temperature, T_c [°C]
100/0	163	78	37	109
		Melt extrusion		
95/5	161	74	35	110
90/10	161	73	35	111
85/15	162	73	35	112
		Melt mixing		
95/5	162	79	38	115
90/10	163	80	38	113
85/15	164	81	39	112
		Melt mixing with PP-g-MAH		
95/5	164	76	36	118
90/10	164	78	37	118
85/15	163	80	38	120

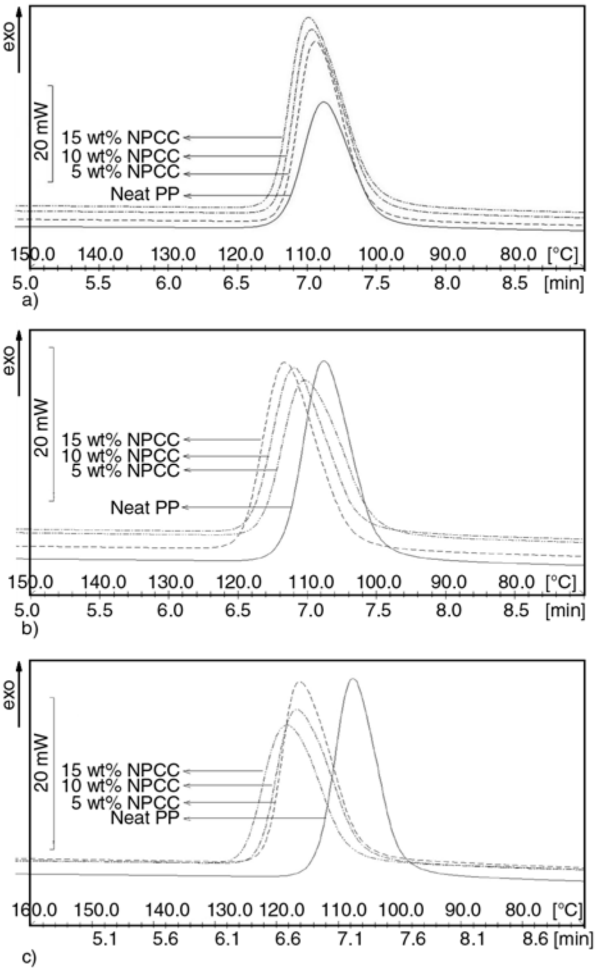

Figure 9. DSC crystallisation curves for nanocomposites prepared via (a) melt extrusion, (b) melt mixing and (c) melt mixing with 10 wt% PP-g-MAH compatibiliser

effect of the nano NPCC particles. In the presence of the compatibiliser, closer interaction between the NPCC particles and the PP matrix has possibly been established and the better dispersed particles has provided more sites for the nucleation of PP to begin.

4. Conclusions

The choice of processing technique has some influence on the properties of the PP/NPCC nanocomposites. The extrusion technique was found to be more effective to disperse the nanofillers when the filler concentration is high, resulting in slightly better impact and tensile strength. Better impact strength was found to be associated with less amount of filler agglomeration as evident from the SEM micrographs. The use of internal mixer was found to be more suitable when the filler concentration used is low. There was no significant difference in the flexural modulus of the nanocomposites using the two different techniques, indicating that the modulus is not significantly affected by the presence of filler agglomerates.

Introduction of PP-g-MAH as compatibiliser for the nanocomposites prepared via mixing improved the filler dispersion, resulting in better impact, modulus and tensile strength. The improvement in impact strength is most likely attributed to the better filler dispersion while the increased tensile strength and modulus may be due to better interfacial adhesion between the filler and the PP matrix. DSC results show that the PP-g-MAH has also improved the nucleating activity of the NPCC, inducing crystallisation of PP to occur at higher temperatures.

Acknowledgements

The authors would like to thank the Ministry of Science, Technology and Innovation (MOSTI), Malaysia for the IRPA research grant (project no.03-01-01-0052-EA001). The authors would also like to thank Zalena Saem and Azura Ruhan for their kind assistance in conducting the SEM analysis.

References

[1] Krawczak P.: Compounding and processing of polymer nanocomposites: From scientific challenges to industrial stakes. Express Polymer Letters, **1**, 188 (2007).
DOI: 10.3144/expresspolymlett.2007.29

[2] Jordan J., Jacob K. I., Tannenbaum R., Sharaf M. A., Jasiuk I.: Experimental trends in polymer nanocomposites – A review. Materials Science and Engineering A, **393**, 1–11 (2005).
DOI: 10.1016/j.msea.2004.09.044

[3] Kaempfer D., Thomann R., Mülhaupt R.: Melt compounding of syndiotactic polypropylene nanocomposites containing organophilic layered silicates and in situ formed core/shell nanoparticles. Polymer, **43**, 2909–2916 (2002).
DOI: 10.1016/S0032-3861(02)00113-1

[4] Rong M. Z., Zhang M. Q., Zheng Y. X., Zeng H. M., Friedrich K.: Improvement of tensile properties of nano-SiO_2/PP composites in relation to percolation mechanism. Polymer, **42**, 3301–3304 (2001).
DOI: 10.1016/S0032-3861(00)00741-2

[5] Yang K., Yang Q., Li G., Sun Y., Feng D.: Morphology and mechanical properties of polypropylene/calcium carbonate nanocomposites. Materials Letters, **60**, 805–809 (2006).
DOI: 10.1016/j.matlet.2005.10.020

[6] López D. G., Picazo O., Merino J. C., Pastor J. M.: Polypropylene-clay nanocomposites: Effect of compatibilizing agents on clay dispersion. European Polymer Journal, **39**, 945–950 (2003).
DOI: 10.1016/S0014-3057(02)00333-6

[7] Wu C. L., Zhang M. Q., Rong M. Z., Friedrich K.: Tensile performance improvement of low nanoparticles filled-polypropylene composites. Composites Science and Technology, **62**, 1327–1340 (2002).
DOI: 10.1016/S0266-3538(02)00079-9

[8] Kashiwagi T., Grulke E., Hilding J., Harris R., Awad W., Douglas J.: Thermal degradation and flammability properties of polypropylene-carbon nanotube composites. Macromolecular Rapid Communications, **23**, 761–765 (2002).
DOI: 10.1002/1521-3927(20020901)23:13<761::AID-MARC761>3.0.CO;2-K

[9] Gorna K., Hund M., Vucak M., Gröhn F., Wegner G.: Amorphous calcium carbonate in form of spherical nanosized particles and its application as fillers for polymers. Materials Science and Engineering A, **477**, 217–225 (2008).
DOI: 10.1016/j.msea.2007.05.045

[10] Liang J. Z.: Evaluation of dispersion of nano-$CaCO_3$ particles in polypropylene matrix based on fractal method. Composites Part A: Applied Science and Manufacturing, **38**, 1502–1506 (2007).
DOI: 10.1016/j.compositesa.2007.01.011

[11] Xie X-L., Liu Q-X., Li R. K-Y., Zhou X-P., Zhang Q-X., Yu Z-Z., Mai Y-W.: Rheological and mechanical properties of PVC/$CaCO_3$ nanocomposites prepared by in situ polymerization. Polymer, **45**, 6665–6673 (2004).
DOI: 10.1016/j.polymer.2004.07.045

[12] Di Lorenzo M. L., Errico M. E., Avella M.: Thermal and morphological characterization of poly(ethylene terephthalate)/calcium carbonate nanocomposites. Journal of Materials Science, **37**, 2351–2358 (2002).
DOI: 10.1023/A:1015358425449

[13] Gilbert M.: Surface treatments for particulate fillers in plastics. in 'Plastics additives: An A-Z reference' (ed.: Pritchard G.) Chapman and Hall, London, 590–603 (1998).

[14] Pukánszky B.: Particulate filled polypropylene: Structure and properties. in 'Polypropylene: structure, blends and composites' (ed.: Karger-Kocsis J.) Chapman and Hall, London, 2–70 (1995).

[15] Roberts D., Constable R. C.: Chemical coupling agents for filled and grafted polypropylene composites. in 'Handbook of polypropylene and polypropylene composites' (ed.: Karian H. G.) Marcel Decker, New York, 28–68 (2003).

[16] Chen J. H., Rong M. Z., Ruan W. B., Zhang M. Q.: Interfacial enhancement of nano-SiO_2/polypropylene composites. Composites Science and Technology, **69**, 252–259 (2008).
DOI: 10.1016/j.compscitech.2008.10.013

[17] Chan C-M., Wu J., Li J-X., Cheung Y-K.: Polypropylene/calcium carbonate nanocomposites. Polymer, **43**, 2981–2992 (2002).
DOI: 10.1016/S0032-3861(02)00120-9

[18] Wang Y., Shen H., Li G., Mai K.: Effect of Interfacial interaction on the crystallization and mechanical properties of PP/nano-$CaCO_3$ composites modified by compatibilizers. Journal of Applied Polymer Science, **113**, 1584–1592 (2009).
DOI: 10.1002/app.30057

[19] Galeski A.: Crystallization. in 'Polypropylene: An A-Z reference' (ed.: Karger-Kocsis J.) Kluwer, Dordrecht, 135–141 (1999).

[20] Thio Y. S., Argon A. S., Cohen R. E., Weinberg M.: Toughening of isotactic polypropylene with $CaCO_3$ particles. Polymer, **43**, 3661–3674 (2002).
DOI: 10.1016/S0032-3861(02)00193-3

[21] Zhang Q-X., Yu Z-Z., Xie X-L., Mai Y-W.: Crystallization and impact energy of polypropylene/$CaCO_3$ nanocomposites with nonionic modifier. Polymer, **45**, 5985–5994 (2004).
DOI: 10.1016/j.polymer.2004.06.044

[22] Guth E. J.: Theory of filler reinforcement. Journal of Applied Physics, **16**, 20–25 (1945).
DOI: 10.1063/1.1707495

[23] Wu Y-P., Jia Q-X., Yu D-S., Zhang L-Q.: Modeling Young's modulus of rubber-clay nanocomposites using composite theories. Polymer Testing, **23**, 903–909 (2004).
DOI: 10.1016/j.polymertesting.2004.05.004

[24] Liang J-Z.: Toughening and reinforcing in rigid inorganic particulate filled poly(propylene): A review. Journal of Applied Polymer Science, **83**, 1547–1555 (2001).
DOI: 10.1002/app.10052

[25] Mudra I.: Structure formation in crystalline polymers in presence of nucleating agents. PhD Thesis, Technical University of Budapest, Hungary (1996).

[26] Lozano T., Lafleur P. G., Grmela M., Thibodeau C.: Effect of filler dispersion on polypropylene morphology. Polymer Engineering and Science, **44**, 880–890 (2004).
DOI: 10.1002/pen.20079

eXPRESS Polymer Letters Vol.4, No.10 (2010) 621–631
Available online at www.expresspolymlett.com
DOI: 10.3144/expresspolymlett.2010.77

Effect of gas saturation conditions on the expansion ratio of microcellular poly(lactic acid)/wood-flour composites

L. M. Matuana[*1,2], *O. Faruk*[2]

[1]School of Packaging,Michigan State University, East Lansing, Michigan 48824, USA
[2]Department of Forestry, Michigan State University, East Lansing, Michigan 48824, USA

Received 9 April 2010; accepted in revised form 20 June 2010

Abstract. Poly(lactic acid) or PLA and PLA/wood-flour composites were microcellular foamed with CO_2 through a batch foaming process. Specifically, the gas saturation pressure and time varied during processing to produce PLA foams with a high expansion ratio. A ten fold expansion ratio resulted in microcellular foamed PLA over unfoamed counterpart. The foaming conditions associated with such a high expansion ratio involved a lower gas saturation pressure up to 2.76 MPa, which corresponds to a critical gas concentration of approximately 9.4%. Beyond this critical value, foam expansion decreased significantly. Investigations also studied the effect of incorporating wood flour on the foamability of the resulting PLA/wood-flour composites. The addition of wood flour into the PLA matrix significantly affected the expansion ratio of PLA/wood-flour composite foams.

Keywords: *biopolymers, biocomposites, microcellular foam, wood plastic composites, cell morphology*

1. Introduction

Poly(lactic acid) or PLA, a plant-based biodegradable plastic, exhibits many properties equivalent to or better than many petroleum-based plastics. However, few commercial applications exist not only due to its lower impact resistance and higher cost than synthetic plastics, but also to having a narrow processing window [1].

Blending PLA with various additives such as lubricant, plasticizer or a second polymer assists in broadening its applications [2, 3]. Unfortunately, this approach could increase the manufacturing cost given the additional expenses associated with the additives [4]. Previous efforts to overcome the cost of PLA included blending with fillers such as cellulosic fibers [5]. However, the lowered cost due to filler addition is usually achieved at the expense of other properties such as the ductility (lower elongation at break) and lower impact resistance, because the incorporated brittle cellulosic fibers alter the ductile mode of failure of the matrix, making the composites more brittle than neat polymer [6–8]. Continuous efforts seek to further reduce the cost of PLA while enhancing its flexibility and toughness. Recently, Wong *et al.* [9] reported that plastics are one of the most consumed materials in the world and in typical plastics manufacturing processes, the material cost account for 50–70% of the total production cost. Therefore, there is a significant economic interest to reduce material usage. The widely recognized foaming process, which includes microcellular plastics as an example, enhances the ductility and impact resistance of the polymer matrix, in addition to providing a significant expansion ratio and weight reduction in plastic parts [10, 11]. The high expansion ratio induced by foaming succeeds in reducing the material cost and consumption in mass-produced plastic parts without a major compromise to the required properties [10, 11]. Recently the production of microcellular-

---

[*]Corresponding author, e-mail: matuana@msu.edu

foamed structures in the polymer through a batch and continuous foaming processes has addressed several of the hindrances associated with PLA [4, 12–20].

Over the past years, several in-depth studies have examined the effects of the processing conditions and formulations on the foamability of PLA in a batch process [4, 12–20]. Fujimoto and coworkers described the foam processing of neat PLA and two different types of PLA/layered silicate nanocomposites using supercritical CO_2 as a foaming agent [12]. The nanocomposite foams showed smaller cell size and larger cell-population density compared to neat PLA owing to the dispersed silicate particles which acted as nucleating sites for cell nucleation [12]. The concentration of organically modified layered silicates has also been shown to strongly affect the cell size and cell-population density of PLA and PLA nanocomposites [18, 19]. Compared with neat PLA, the nanocomposites foamed at 110°C using a 20:80 blend of CO_2:N_2 mixture as the blowing agent exhibited reduced cell size and increased cell-population density, due to the presence of the heterogeneous bubble nucleation sites. However, nanocomposites with higher organoclay content (10%) was poorly foamed due to the intrinsically high viscosity and elasticity, caused by organoclay exfoliation and chain extension/branching, which reduce the cell growth [18].

Conditioning PLA with CO_2 has been reported to induce crystallinity in the polymer and the degree of crystallinity of PLA increases with increasing saturation pressure [14, 15]. The greatest increases in crystallinity under room temperature conditions was observed at pressures between 2.1 and 2.8 MPa, and this induced crystallinity significantly affected the PLA foamability. In fact, Hu *et al.* [15] reported that lower saturation pressure (up to 2.8 MPa) leads to more uniform microcellular structures whereas foam structures become inhomogeneous with an increase in saturation pressure, owing to the rapid diffusion of CO_2 out of the polymer.

Attempts have also been made to enhance the foamability of PLA by controlling the melt rheology of PLA through increasing the molecular weight to compensate for the molecular weight decrease caused by processing degradation and to increase the melt viscosity [19, 20]. PLA modified with chain extenders showed enhanced melt viscosity and elasticity, resulting in the production of foamed PLA with smaller cell size, higher cell-population density, and lower foam density compared to the unmodified counterpart [19, 20]

In addition to the ingredients used in the PLA formulations, processing variables also affect the foamability of PLA. Investigations have shown that the foaming time and/or the foaming temperature are important process variables for controlling the density and porous morphology of PLA foams owing to their effects on the visco-elastic properties of the polymer [4]. Studying the dependence of the foam density on the foaming temperature under different CO_2 pressures (14–30 MPa) for both neat PLA and PLA-based nanocomposites, Ema *et al.* [13] reported that the critical foaming temperature is around 140°C where the morphology of foamed samples changes from nanocellular to a microcellular structure. The competition between cell nucleation and cell growth accounts for these two distinct trends. Cell nucleation dominates at the low foaming temperature (up to 140°C), owing to a large supply of CO_2 molecules in the system coupled with the high viscosity of the matrix, which suppresses cell growth. By contrast, cell growth and coalescence occurs at higher foaming temperature (>150°C) due to the low viscosity of the system [13].

Our previous study showed significant improvements in the volume expansion ratio (a two-fold expansion over unfoamed PLA), impact resistance (up to four-fold increase over unfoamed PLA), strain at break (up to two-fold increase over unfoamed PLA), and toughness (up to four-fold increase over unfoamed PLA) by creating foamed microcells in PLA samples. The results imply that foamed PLA exhibits enhanced ductility and impact resistance owing to the presence of microcells [4].

Although previous study indicates the successful creation of microcellular structures in PLA [4], a higher expansion ratio (greater than two-fold expansion over unfoamed PLA) remained unobtainable. The reasoning behind this result lays in the fact that some critical foaming conditions such as saturation pressure and time, which exert a strong influence on the foaming ability of the polymer matrix, stayed constant in our previous study [4]. Therefore, investigating the feasibility of producing a larger expansion ratio in PLA requires further studies. This study aims to investigate other parameters, in order to achieve the desired expansion ratio.

Furthermore, while demonstrations that clearly illustrate the importance of generating microcellular foamed structures in neat PLA as a means to improve its impact strength and reduce material consumption (through expansion) exist, the effect of incorporating cellulosic fibers on the foamability of the resulting PLA/wood-flour composites lacked investigation in our previous study. Improvements in the toughness of PLA by microcellular foaming resulted at the expense of the strength and stiffness, implying the need for using fibers to strengthen foamed samples. Therefore, this study also aimed at understanding the foamability of PLA filled with wood flour.

2. Experimental

2.1. Materials

The matrix consisted of a commercial grade PLA resin (PLA 8302D from NatureWorks® LLC, Minnetonka, MN, USA). The properties of this resin measured by the authors [21] include the following (a density of 1.257 g/cm^3, a percent crystallinity of 1.2%, and a melt flow index of 6.5 g/10 min (190°C, 2.16 kg dead load). Carbon dioxide acted as the foaming agent (commercial 99.5% min). Wood flour from hardwood maple species (40-mesh size) supplied by American Wood Fibers (Schofield, WI, USA) was used as filler. Gamma-aminopropyltriethoxysilane (SCA 1100) supplied by Struktol (Stow, OH, USA) was used as coupling agent.

2.2. Treatment of wood flour

The use of coupling agents, which are important ingredients in the formulations of plastic/wood-fiber composites, also has a significant effect during the foaming process of the composites [22]. Surface modification of wood fiber with a coupling agent has strong effects on both the concentration of gas molecules absorbed by the composites and the cell morphology of the foamed composites produced through a batch foaming process [6, 22]. Previous studies showed that a microcellular-foamed structure was better developed in the composites with treated wood fibers than in the composites with untreated fibers because the addition of coupling agent into the formulation helped encapsulate the gas in the composites for the cell growth [6, 22]. Consequently, silane was used as a coupling agent to enhance the adhesion between the matrix and the filler.

The silane coupling agent was mixed with wood flour in a 60 ml electrically heated three-piece internal mixer/measuring head (3:2 gear ratio) with roller style mixing blades (C. W. Brabender Instruments Inc., South Hackensack, NJ, USA). The mixing process ran at a constant mixer temperature of 100°C for 3 minutes. The rotor speed ran at 50 rpm with the weight charge set at 20 g. A 5 kg dead weight rested on the top of the ram throughout the experiments. The silane coupling agent content remained at 1%, based on the weight of wood flour in the composites [23].

2.3. Manufacture of PLA and PLA/wood-flour composite films

PLA and wood-flour treated with silane were directly blended in a kitchen mixer (Blender MX1050XTS from Warning Commercial Xtreme, Torrington, CT, USA) at 22 000 rpm for 1 minute. The amount of wood flour into the composites varied from 10 to 40 wt% based on the total weight of the composites. The compounded materials (60 g) were then fed into the internal mixer as described above for melt blending at 180°C for 5 minutes. The melted composites were then compression-molded into panels (Erie Mill Co., Erie, Pennsylvania, USA) at 180°C and 3 MPa constant pressure for 1 minute. The thickness of the panels measured around 1.5–2 mm. Manufacturing neat PLA films followed a similar process.

2.4. Sorption and foaming experiments

Sorption experiments performed on neat PLA used a gravimetric method as described in previous papers [6, 22]. The main purpose of sorption experiments involves estimating the amount of gas absorbed in a polymer (or estimated gas solubility), one of the important factors in the gas foaming process [6, 22]. During the foaming experiments, the number of bubbles nucleated depends strongly on the concentration of gas dissolved in the molten polymer matrix [6, 22].

Compression-molded samples were cut into 1.27 cm×2.54 cm rectangular specimens. The original weights of these samples were measured using a digital balance readable to 0.0001 g. The samples were then placed in a pressure chamber and saturated with CO_2 at various pressures (1.38 to 5.52 MPa or 200 to 800 psi) at room temperature for various periods of time (1–10 days). At the end of the saturation, the CO_2-saturated samples were removed from the pressure chamber and rapidly weighed again on the balance to determine the amount of CO_2 absorbed (measured solubility). The weight gain percent of CO_2 was obtained by calculating the difference between the two weights. It should be pointed out that the loss of blowing agent in a batch foam processing used in this study is unavoidable. Nevertheless, the weight gain was measured within few seconds after removing saturated samples from the pressure vessel to minimize the gas escape to the environment.

Producing microcellular-foamed structures in the neat PLA samples required subjecting the CO_2-saturated samples to a rapid pressure drop and a rapid temperature increase that resulted in nucleation and growth of gas nuclei. This was achieved by taking the specimens out of the pressure chamber and heating them above their glass transition temperature using a well-controlled temperature bath at 150°C for 5 seconds. After foaming, the samples were kept in air for 10 seconds for cell growth and then immediately dipped into a water bath to freeze the foam structure and minimize the deterioration of cells through cell coalescence during bubble growth [4, 6, 22].

Composite samples were also foamed at 150°C for 5 seconds, but the samples were saturated at 2.76 MPa (400 psi) for 4 days based on sorptions isotherms, which will be discussed later on.

2.5. Characterization of microcellular foamed samples

The densities of the unfoamed (ρ_u) and foamed (ρ_f) samples measured according to ASTM standard D792 (Buoyancy method) involved measuring the weights of at least five randomly selected samples for each formulation in the air (m_1) and in n-hexane (m_2). Determining the density of the material (Equation 1), the void fraction (V_f) (Equation 2) or equivalently the density reduction, and the volume expansion ratio (ϕ) (Equation 3) used the following equations, respectively:

$$\text{density} = \frac{m_1 \cdot \rho_{FL}}{m_1 - m_2} \tag{1}$$

$$V_f = \frac{\rho_u - \rho_f}{\rho_u} \cdot 100 \tag{2}$$

$$\phi = \frac{\rho_u}{\rho_f} = \frac{1}{1 - V_f} \tag{3}$$

with ρ_{FL} as the density of n-hexane (0.6594 g/cm^3). Scanning electron microscope (SEM) images obtained from a JEOL 6300F FESEM at 10 kV aided in observing and analyzing the cellular morphology of the foamed PLA samples. Gold-coating the fractured surfaces of foamed samples preceded to SEM analysis.

3. Results and discussion

3.1. Sorption behaviors of CO_2 in PLA

Although the aim of this study was to produce microcellular foam in PLA/wood-flour composites, it is paramount to first understand the effect of saturation conditions on the foamability of neat PLA since the gas does not dissolve in wood particles, i.e., PLA is the only component of the composite that can be foamed.

The amount of sorbed CO_2 in neat PLA was determined as a function of the saturation pressures (from 1.38 to 5.52 MPa or from 200 to 800 psi) and times (1–10 days) at room temperature. Figures 1a and 1b show the sorption isotherms obtained in these experiments and the effect of the gas saturation pressure (10 days saturation time) on the amount of gas dissolved in the matrix, respectively. The gas content in the polymer followed Henry's law and remained directly proportional to the gas pressure (Figure 1) [4]. This trend was expected because by increasing pressure, the gas molecules are forced between polymer chains, expanding the space between molecules and thus increasing their mobility, which allow more gas molecules to be absorbed [24]. The amount of CO_2 (or measured solubility of CO_2) in PLA measured significantly higher (21.1%) when compared to other glassy matrices such as PVC (8.6%) and PS (0.8%) [4]. The Lewis acid-base intermolecular interactions where the carbonyl groups of PLA act as an elec-

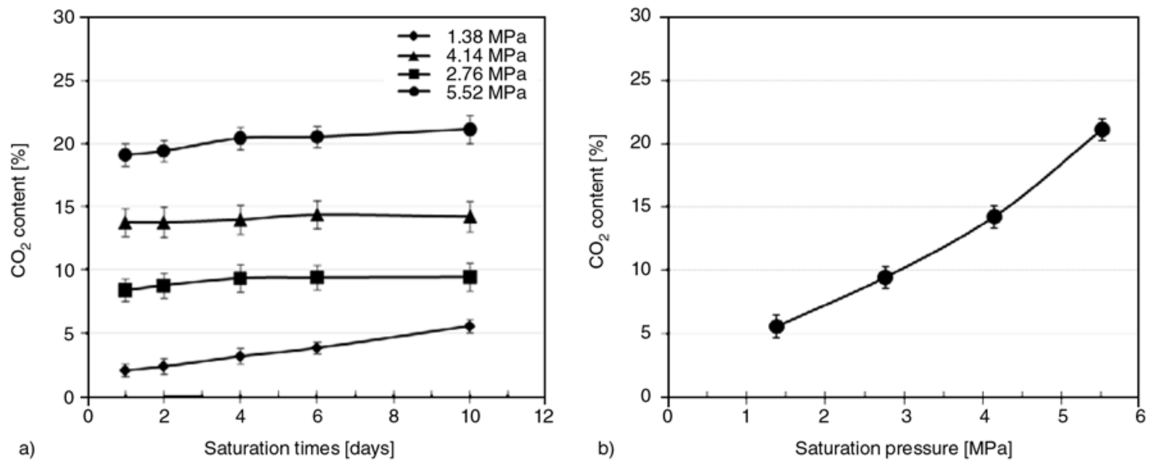

Figure 1. (a) CO_2 concentration in PLA as function of saturation pressure (1.38 to 5.52 MPa) and saturation time (1–10 days) and (b) CO_2 content vs. saturation pressure (10 days saturation time) measured at room temperatures. The trend line option in Figure 1b was set as linear and intercept at zero.

tron donor and carbon dioxide acts as an electron acceptor produced this anticipated effect. Moreover, this type of interaction where the polar groups in the polymers provide more sites for CO_2 molecules was previously shown by other investigators [24–28].

Although the amount of CO_2 dissolved in PLA increased as the saturation pressure increased, irre-

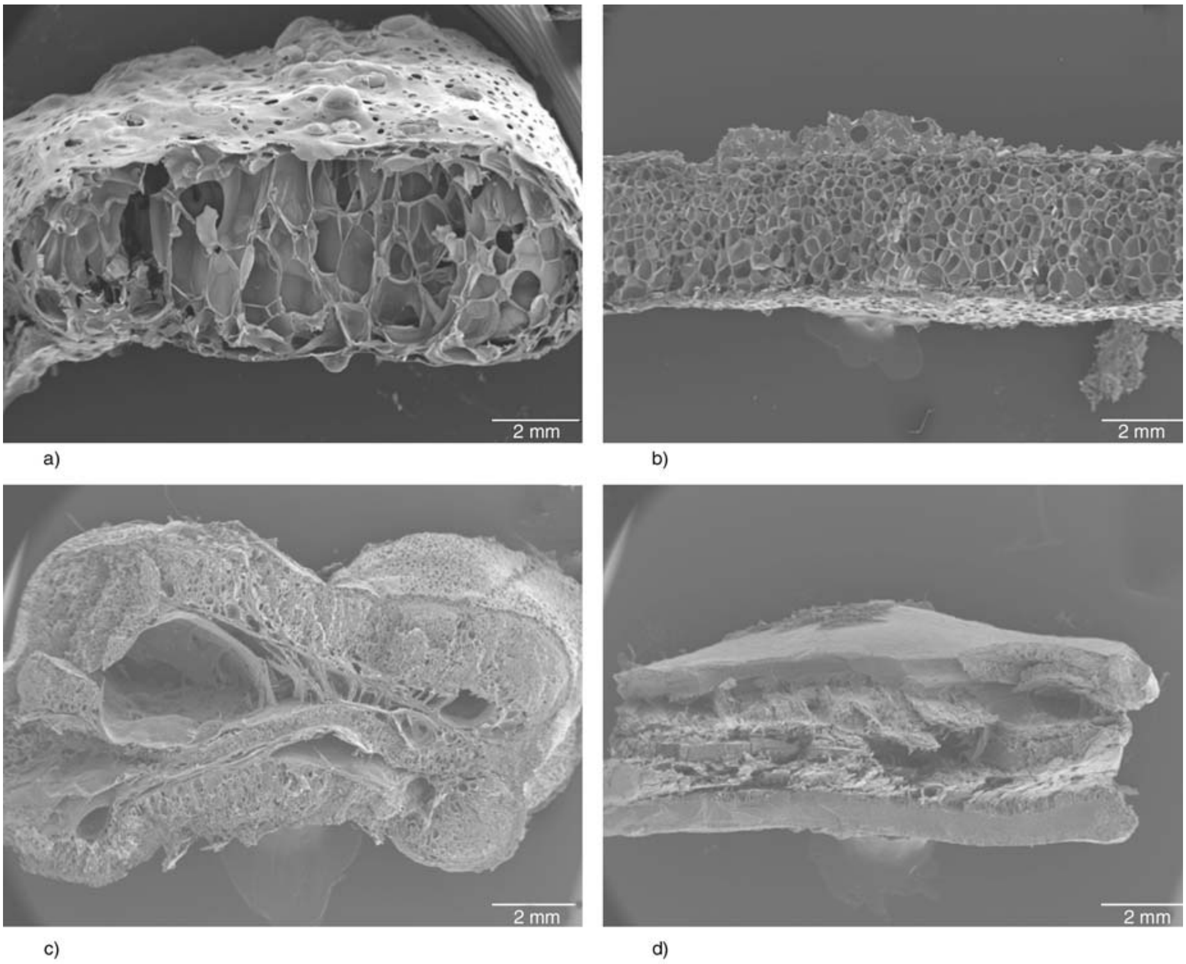

Figure 2. Effect of saturation pressure on the cellular structures of PLA: (a) 1.38 MPa, (b) 2.76 MPa, (c) 4.14 MPa, (d) 5.52 MPa for 10 days, magnification (10×)

spective of the saturation duration (Figure 1a), the amount of CO_2 absorbed by neat PLA, however, only acted as a strong function of saturation time at lower saturation pressures (up to 2.76 MPa or 400 psi). Absorbing the large amount of CO_2 when saturated at lower pressure required a longer saturation time for PLA. As seen in Figure 1a, the CO_2 content in the PLA at 1.38 MPa (200 psi) doubled when the saturation time increased from 1 to 10 days, implying that the longer the polymer is exposed to CO_2, the greater the absorbed CO_2 amount by the polymer as expected from the Fick's law of diffusion [22]. Similar trends were reported by other investigators [29].

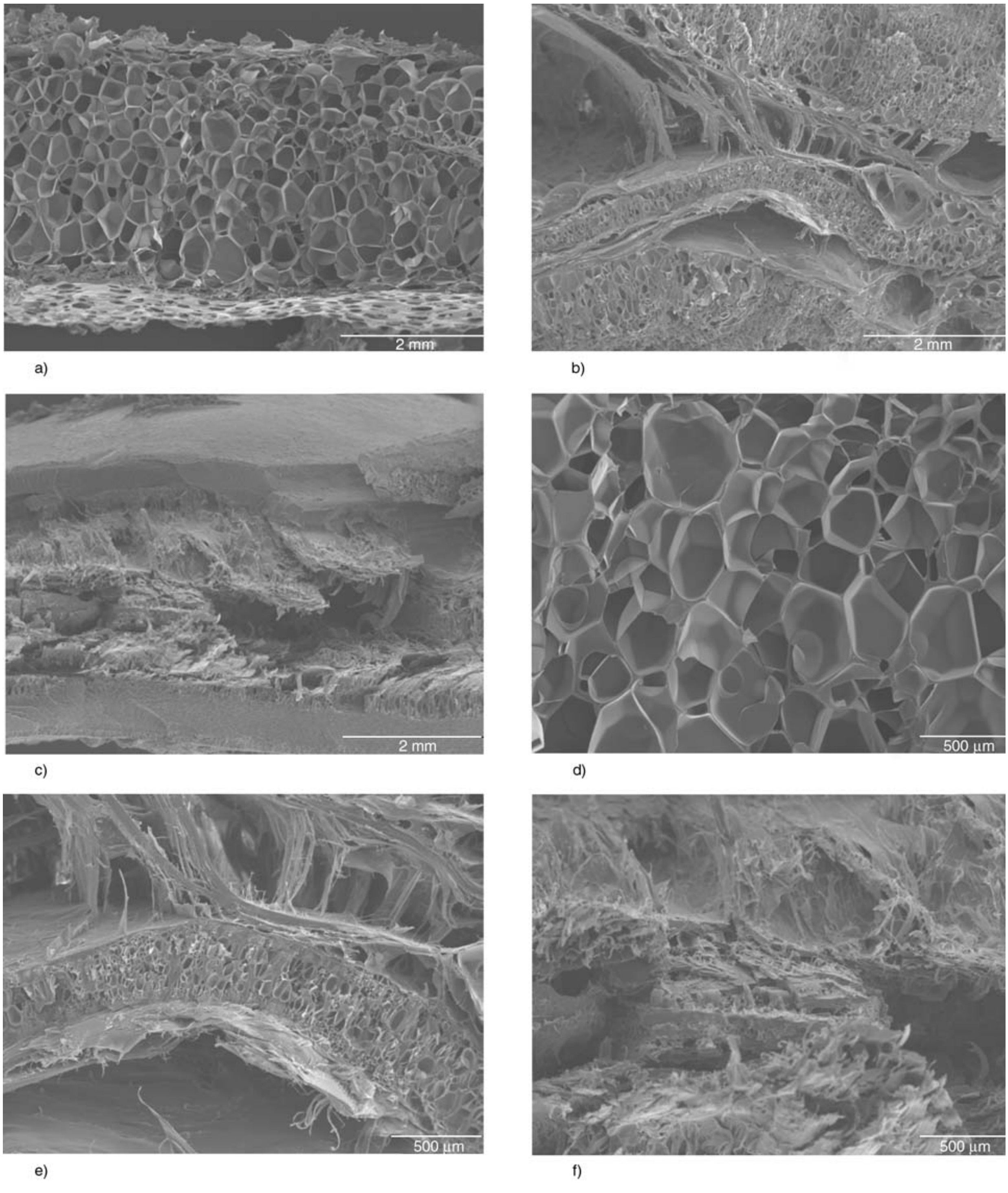

Figure 3. Effect of saturation pressure on the cellular structures of PLA: (a, d) 2.76 MPa, (b, e) 4.14 MPa, (c, f) 5.52 MPa for 10 days. SEM for images a, b, c and for images d,e, f were taken at low magnification (20×) and high magnification (50×), respectively

3.2. Morphology and expansion ratio of microcellular neat PLA

Figures 2 and 3 illustrate the effect of CO_2 saturation pressure on the cellular morphology of microcellular foamed neat PLA. A lower saturation pressure (1.38 MPa) produced larger cells compared to higher saturation pressures. Overall, the lower saturation pressures (up to 2.76 MPa) resulted in more uniform microcellular structures. Higher saturation pressure resulted in the structures becoming inhomogeneous and drastically deteriorated, owing to the polymer's rapid diffusion of CO_2 and the CO_2-induced crystallization in PLA from the plasticizing effect of gas at high concentrations [15, 30].

These results correlated with those reported by other investigators who found that an optimal saturation pressure for foaming PLA exists. For example, Hu and coworkers [15] measured the degree of crystallinity of PLA [a copolymer of poly-L-lactic acid (PLLA) and poly-DL-lactic acid (PDLLA)] conditioned with CO_2 at room temperature and pressures up to 5.8 MPa. They found that the degree of crystallinity increases with increasing saturation pressure [15]. In fact, lower saturation pressure (up to 2.8 MPa) led to more uniform microcellular structures with cell diameters on the order of 30–40 µm and a cell density of $7.93 \cdot 10^7$ cell/cm^3. By contrast, foam structures became inhomogeneous and cell size decreased with an increase in saturation pressure, owing to the rapid diffusion of CO_2 out of the polymer. As a result, the density of the foamed sample was almost similar to that of unfoamed material [15, 30].

Furthermore, it is recognized that the solubility and diffusivity of gas in semi-crystalline polymers are a function of the degree of crystallinity because gas does not dissolve in the crystallites [22, 31–33]. Increasing the mass fraction of crystallite in the polymer leads to the reduction of the amorphous matrix mass fraction. As a result, the solubility and diffusivity of gas are reduced since the gas does not dissolve in the crystallites, and the crystallites tend to obstruct the movement of gas molecules in the polymer [22]. Since the crystal domains in semi-crystalline polymer do not absorb gas, induced crystallinity in PLA by increasing the gas saturation pressure may have reduced the amount of gas available in the amorphous region due to the lower amorphous volume fraction, thus affecting the morphology developed in the foamed PLA samples saturated at higher pressure (Figures 2c and 2d).

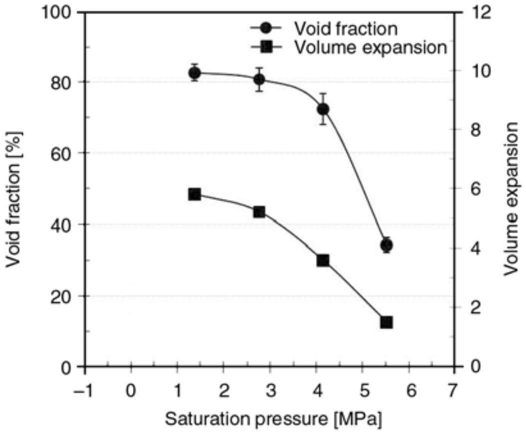

Figure 4. Influence of saturation pressure on the void fraction and volume expansion ratio of neat PLA foams. Samples were saturated for 10 days. Error bars did not appear in the graph due to the smaller values of standard deviations.

Figure 4 shows the effect of saturation pressure on the void fraction and volume expansion ratio. Higher volume fraction and expansion ratio were achieved, but they remained almost constant as the gas saturation pressure increased up to 2.76 MPa. However, above 2.76 MPa, both the void fraction and the expansion ratio were directly proportional to the gas pressure; they decreased as the gas saturation pressure increased. The results suggest the need for a critical gas concentration of approximately 9.4% for significant foam expansion to occur. Increasing the concentration of CO_2 beyond this critical value had a deleterious effect on the volume expansion, i.e., foam expansion remained low. The results imply the potential for achieving a higher expansion ratio in microcellular PLA foams conditioned at lower saturation pressure (e.g., up to 2.76 MPa) that corresponds to a critical gas concentration of approximately 9.4%. At this condition, the saturation time of 4 days will be required for CO_2 diffusion in the samples (Figure 1a).

3.3. Morphology and expansion ratio of microcellular foamed PLA/wood-flour composites

Figures 5 and 6 illustrate the effect of wood flour content on the cellular structures of PLA/wood-flour composites, whereas Figure 7 shows the influence of wood flour content on the void fraction and volume expansion ratio. The samples were saturated at 2.76 MPa (400 psi) for 4 days and foamed at 150°C for 5 sec. Lower saturation pressure was selected since it produced foamed PLA specimens with homogeneous morphology (Figures 2 and 3) and high volume expansion (Figure 4).

All microcellular foamed PLA/wood-flour composite samples had cells with finer average size than their neat PLA counterpart (Figures 5 and 6). The cell size decreased further as the wood flour content increased in the matrix. The incorporation of wood flour into the PLA matrix produced this expected effect, as it increased the melt viscosity of the matrix and made the composites stiffer than the unfilled PLA, which provided high resistance to the cell growth in the polymer matrix [6, 34–38].

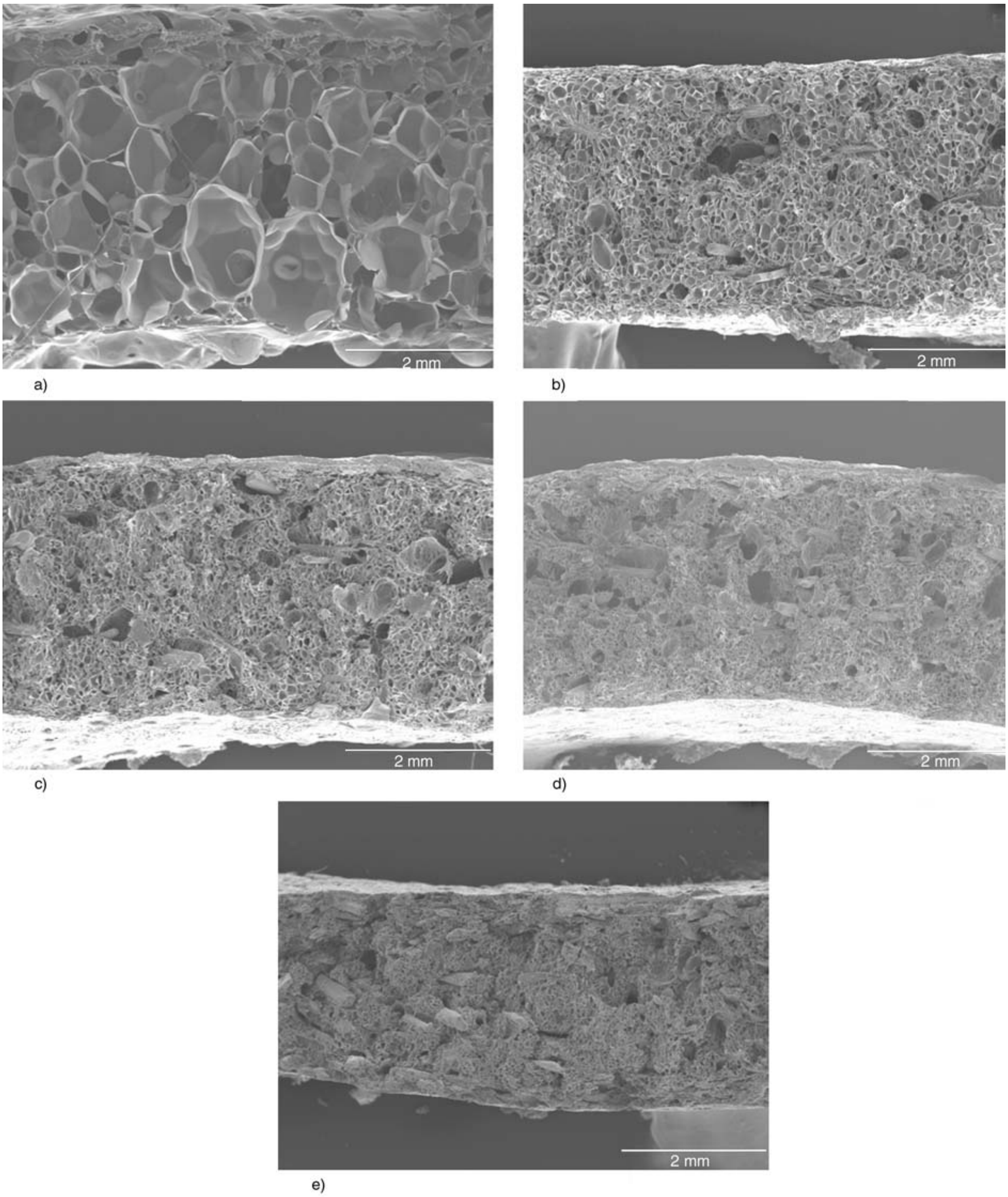

Figure 5. Effect of wood flour content on the cellular structures of PLA: (a) 0 wt%, (b) 10 wt%, (c) 20 wt%, (d) 30 wt%, (e) 40 wt%, saturation pressure 2.76 MPa for 4 days, magnification (20×)

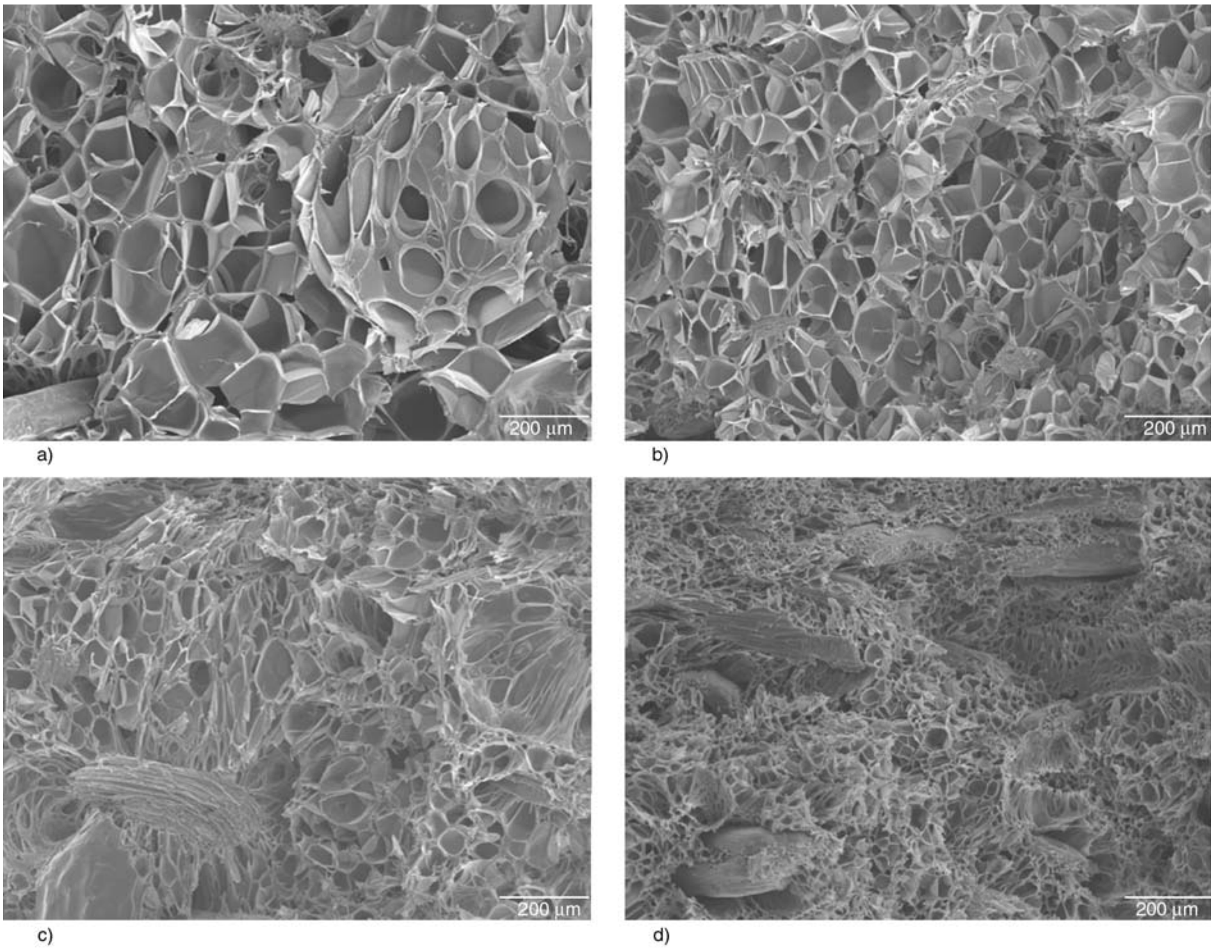

Figure 6. Effect of wood fiber content on the cellular structures of PLA: (a) 10 wt%, (b) 20 wt%, (c) 30 wt%, (d) 40 wt%, saturation pressure 2.76 MPa for 4 days, magnification (100×)

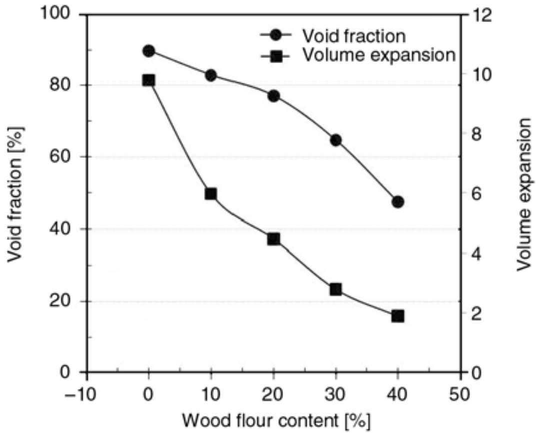

Figure 7. Effect of wood fiber content on the void fraction and volume expansion ratio of PLA/wood-flour composites foams. Samples were saturated at 2.76 MPa for 4 days.

Observations also suggest that the addition of wood flour into the PLA matrix significantly affected the expansion ratio (void fraction) of PLA/wood-flour composite foams. As illustrated in Figure 7, increasing the wood flour content in the PLA matrix tended to noticeably decrease the expansion ratio of PLA in foamed samples. The anticipation of this tendency can be attributed not only to the number of nucleated cells and their growth, which controls the volume expansion ratio (or void fraction) during the foaming process but also to the strong dependency on the amount of gas molecules dissolved in the material as well as the volume fraction of the matrix in the composite [6, 34–38]. Our previous study showed that increasing wood flour content in the composites tends to decrease the volume fraction of the matrix in the composites [22]. Consequently, with a noticeably lowered amount of gas absorbed by the composite samples during foaming than that absorbed by neat plastic [6, 34, 37], coupled with the decreased fraction of the matrix available for gas diffusion, the volume expansions in the composites also remained far inferior to those in the unfilled PLA foams.

4. Conclusions

The influence of gas saturation conditions was assessed to produce microcellular foamed PLA with a high expansion ratio. In addition, this study examined the effect of incorporating wood flour on the foamability of the resulting PLA/wood-flour composites. The experimental results produce the following conclusions:

Microcellular PLA foams have the potential for a larger void fraction (up to 82% density reduction) and higher expansion ratio (ten fold expansion over unfoamed PLA). The foaming conditions associated with such an elevated expansion ratio involved a lower gas saturation pressure up to 2.76 MPa, which corresponds to a critical gas concentration of approximately 9.4%. Increasing the concentration of CO_2 beyond this critical value had a deleterious effect on the volume expansion, i.e., foam expansion decreased significantly.

The addition of wood flour into the PLA matrix significantly affected the expansion ratio (void fraction) of PLA/wood-flour composite foams. Increasing the wood flour content in the PLA tended to noticeably decrease the expansion ratio of PLA in foamed samples.

Acknowledgements

This project was partially supported by the National Research Initiative of the USDA Cooperative State Research, Education and Extension Service, grant number 2006-35504-17414.

References

[1] Kramschuster A., Pilla S., Gong S., Chandra A., Turng L-S.: Injection molded solid and microcellular polylactide compounded with recycled paper shopping bag fibers. International Polymer Processing, **22**, 436–445 (2007).
DOI: 10.3139/217.2063

[2] Mihai M., Huneault M. A., Favis B. D., Li H.: Extrusion foaming of semi-crystalline PLA and PLA/thermoplastic starch blends. Macromolecular Bioscience, **7**, 907–920 (2007).
DOI: 10.1002/mabi.200700080

[3] Baiardo M., Frisoni G., Scandola M., Rimelen M., Lips D., Ruffieux K., Wintermantel E.: Thermal and mechanical properties of plasticized poly(L-lactic acid). Journal of Applied Polymer Science, **90**, 1731–1738 (2003).
DOI: 10.1002/app.12549

[4] Matuana L. M.: Solid state microcellular foamed poly(lactic acid): Morphology and property characterization. Bioresource Technology, **99**, 3643–3650 (2008).
DOI: 10.1016/j.biortech.2007.07.062

[5] Pilla S., Gong S., O'Neil E., Rowell R. M., Krzysik A. M.: Polylactide-pine wood flour composites. Polymer Engineering and Science, **48**, 578–587 (2008).
DOI: 10.1002/pen.20971

[6] Matuana L. M., Park C. B., Balatinecz J. J.: Processing and cell morphology relationships for microcellular foamed PVC/wood-fiber composites. Polymer Engineering and Science, **37**, 1137–1147 (1997).
DOI: 10.1002/pen.11758

[7] Matuana L. M., Park C. B., Balatinecz J. J.: The effect of low levels of plasticizer on the rheological and mechanical properties of polyvinyl chloride/newsprint-fiber composites. Journal of Vinyl and Additive Technology, **3**, 265–273 (1997).
DOI: 10.1002/vnl.10204

[8] Matuana L. M., Woodhams R. T., Balatinecz J. J., Park C. B.: Influence of interfacial interactions on the properties of PVC/cellulosic fiber composites. Polymer Composites, **19**, 446–455 (1998).
DOI: 10.1002/pc.10119

[9] Wong A., Leung S. N., Hasan M. M., Park C. B.: The foamability of polypropylene copolymer blown with argon, nitrogen and helium. in 'SPE ANTEC Technical Papers, Milwaukee, USA' 2551–2555 (2008).

[10] Martini-Vvedensky J. E., Waldman F. A., Suh N. P.: The production and analysis of microcellular thermoplastic foam. in 'SPE ANTEC Technical Papers, San Francisco, USA' 674–676 (1982).

[11] Martini J. E., Suh N. P., Waldman F. A.: Microcellular closed cell foams and their method of manufacture. U.S. Patent 4473665, USA (1984).

[12] Fujimoto Y., Ray S. S., Okamoto M., Ogami A., Yamada K., Ueda K.: Well-controlled biodegradable nanocomposite foams: From microcellular to nanocellular. Macromolecular Rapid Communications, **24**, 457–461 (2003).
DOI: 10.1002/marc.200390068

[13] Ema Y., Ikeya M., Okamoto M.: Foam processing and cellular structure of polylactide-based nanocomposites. Polymer, **47**, 5350–5359 (2006).
DOI: 10.1016/j.polymer.2006.05.050

[14] Liao X., Nawaby A. V., Whitfield P., Day M., Champagne M., Denault J.: Layered open pore poly(L-lactic acid) nanomorphology. Biomacromolecules, **7**, 2937–2941 (2006).
DOI: 10.1021/bm060738u

[15] Hu X., Nawaby A. V., Naguib H. E., Day M., Ueada K., Liao X.: Polylactic acid (PLA)-CO_2 foams at subcritical conditions. in 'SPE ANTEC Technical Papers, Boston, USA' 2670–2673 (2005).

[16] Wang X., Kumar V., Li W.: Low density sub-critical CO_2-blown solid-state PLA foams. Cellular Polymers, **26**, 11–35 (2007).

[17] Matuana L. M., Diaz C. A.: Study of cell nucleation in microcellular poly(lactic acid) foamed with supercritical CO_2 through a continuous-extrusion process. Industrial and Engineering Chemistry Research, **49**, 2186–2193 (2010).
DOI: 10.1021/ie9011694

[18] Di Y., Iannace S., Di Maio E., Nicolais L.: Poly(lactic acid)/organoclay nanocomposites: Thermal, rheological properties and foam processing. Journal of Polymer Science Part B: Polymer Physics, **43**, 689–698 (2005).
DOI: 10.1002/polb.20366

[19] Marrazzo C., Di Maio E., Iannace S.: Foaming of synthetic and natural biodegradable polymers. Journal of Cellular Plastics, **43**, 123–133 (2007).
DOI: 10.1177/0021955X06073214

[20] Di Y., Iannace S., Di Maio E., Nicolais E.: Reactively modified poly(lactic acid): Properties and foam processing. Macromolecular Materials and Engineering, **290**, 1083–1090 (2005).
DOI: 10.1002/mame.200500115

[21] Matuana L. M., Faruk O., Diaz C. A.: Cell morphology of extrusion foamed poly(lactic acid) using endothermic chemical foaming agent. Bioresource Technology, **100**, 5947–5954 (2009).
DOI: 10.1016/j.biortech.2009.06.063

[22] Matuana-Malanda L., Park C. B., Balatinecz J. J.: Characterization of microcellular PVC/cellulosic-fibre composites. Journal of Cellular Plastics, **32**, 449–469 (1996).
DOI: 10.1177/0021955X9603200503

[23] Matuana L. M., Balatinecz J. J., Park C. B., Sodhi R. N. S.: X-ray photoelectron spectroscopy study of silane-treated newsprint-fibers. Wood Science and Technology, **33**, 259–270 (1999).
DOI: 10.1007/s002260050114

[24] Aionicesei E., Škerget M., Knez Z.: Measurement of CO_2 solubility and diffusivity in poly(L-lactide) and poly(D,L-lactide-co-glycolide) by magnetic suspension balance. The Journal of Supercritical Fluids, **47**, 296–301 (2008).
DOI: 10.1016/j.supflu.2008.07.011

[25] Nalawade S. P., Picchioni F., Marsman J. H., Janssen L. P. B. M.: The FT-IR studies of the interactions of CO_2 and polymers having different chain groups. The Journal of Supercritical Fluids, **36**, 236–244 (2006).
DOI: 10.1016/j.supflu.2005.06.005

[26] Nalawade S. P., Picchioni F., Marsman J. H., Grijpma D. W., Feijen J., Janssen L. P. B. M.: Intermolecular interactions between carbon dioxide and the carbonyl groups of polylactides and poly(ε-caprolactone). Journal of Controlled Release, **116**, 38–40 (2006).
DOI: 10.1016/j.jconrel.2006.09.038

[27] Kazarian S. G., Vincent M. F., Bright F. V., Liotta C. L., Eckert C. A.: Specific intermolecular interaction of carbon dioxide with polymers. Journal of the American Chemical Society, **118**, 1729–1736 (1996).
DOI: 10.1021/ja950416q

[28] Shieh Y-T., Liu K-H.: The effect of carbonyl group on sorption of CO_2 in glassy polymers. The Journal of Supercritical Fluids, **25**, 261–268 (2003).
DOI: 10.1016/S0896-8446(02)00145-6

[29] Goel S. K., Beckman E. J.: Generation of microcellular polymeric foams using supercritical carbon dioxide. I: Effect of pressure and temperature on nucleation. Polymer Engineering and Science, **34**, 1137–1147 (1994).
DOI: 10.1002/pen.760341407

[30] Hao A., Geng Y., Xu Q., Lu Z., Yu L.: Study of different effects on foaming process of biodegradable PLA/starch composites in supercritical/compressed carbon dioxide. Journal of Applied Polymer Science, **109**, 2679–2686 (2008).
DOI: 10.1002/app.27861

[31] Michaels A. S., Bixler H. J.: Solubility of gases in polyethylene. Journal of Polymer Science, **50**, 393–412 (1961).
DOI: 10.1002/pol.1961.1205015411

[32] Michaels A. S., Bixler H. J.: Flow of gases in polyethylene. Journal of Polymer Science, **50**, 413–439 (1961).
DOI: 10.1002/pol.1961.1205015412

[33] Van Krevelen D. W.: Properties of polymers. Elesevier Science Publishers, New York (1990).

[34] Li Q., Matuana L. M.: Foam extrusion of high density polyethylene/wood-flour composites using chemical foaming agent. Journal of Applied Polymer Science, **88**, 3139–3150 (2003).
DOI: 10.1002/app.12003

[35] Matuana L. M., Li Q.: A factorial design applied to the extrusion foaming of polypropylene/wood-flour composite foams. Cellular Polymers, **20**, 115–130 (2001).

[36] Matuana L. M., Li Q.: Statistical modeling and response surface optimization of extruded HDPE/wood-flour composite foams. Journal of Thermoplastics Composite Materials, **17**, 185–199 (2004).
DOI: 10.1177/0892705704035404

[37] Mengeloglu F., Matuana L. M.: Foaming of rigid PVC/wood-flour composites through a continuous extrusion process. Journal of Vinyl and Additive Technology, **7**, 142–148 (2001).
DOI: 10.1002/vnl.10282

[38] Matuana L. M., Mengeloglu F.: Manufacture of rigid PVC/wood-flour composite foams using moisture contained in wood as foaming agent. Journal of Vinyl and Additive Technology, **8**, 264–270 (2002).
DOI: 10.1002/vnl.10373

eXPRESS Polymer Letters Vol.4, No.10 (2010) 632–643
Available online at www.expresspolymlett.com
DOI: 10.3144/expresspolymlett.2010.78

Dielectric properties of poly(vinylidene fluoride)/ $CaCu_3Ti_4O_{12}$ nanocrystal composite thick films

P. Thomas[1,2], *S. Satapathy* [3], *K. Dwarakanath*[1], *K. B. R. Varma*[2*]

[1]Dielectric Materials Division, Central Power Research Institute, Bangalore 560080, India
[2]Materials Research Centre, Indian Institute of Science, Bangalore 560012, India
[3]Laser Materials Development & Devices Division, Raja Ramanna centre for Advanced Technology, Indore 452013, India

Received 24 March 2010; accepted in revised form 21 June 2010

Abstract. The poly(vinylidene fluoride)/$CaCu_3Ti_4O_{12}$ (CCTO) nanocrystal composite films (thickness ≈ 85 μm) with relatively high dielectric permittivity (90 at 100 Hz) were prepared by the solution casting followed by spin coating technique. The structural, the microstructural and the dielectric properties of the composites were studied using X-ray diffraction, Scanning Electron Microscope, and Impedance analyzer respectively. The effective dielectric permittivity (ε_{eff}) of the composite increased with increase in the volume fraction of CCTO at all the frequencies (100 Hz to 1 MHz) under investigation. The room temperature dielectric permittivity which is around 90 at 100 Hz, has increased to about 290 at 125°C (100 Hz). These results may be exploited in the development of high energy density capacitors.

Keywords: *polymer composites, poly(vinylidene fluoride), $CaCu_3Ti_4O_{12}$ oxide, nanocomposite, electrical properties*

1. Introduction

Recently, the high dielectric permittivity composite materials have been considered to be potential candidates for integration into electronic devices. Owing to the continuous development towards the miniaturization of electronics, newer dielectric materials were sought which would enable to achieve high energy density for capacitor applications. Ceramics possessing very high dielectric permittivity are being used as voltage capacitors due to their high breakdown voltages. However, they are brittle, suffer from poor mechanical strength and hence cannot be exposed to high fields. Polymer films such as polyester, polycarbonate, polypropylene, polystyrene and polyethylenesulphide are being used in the fabrication of low leakage capacitors. Though polymers possess relatively low dielectric permittivity, they can withstand high fields, are flexible and easy to process. By combining the advantages of both, one can fabricate new hybrid materials with high dielectric permittivity, and high breakdown voltages to achieve high volume efficiency and energy storage density for applications in capacitors as electric energy storage devices [1–7]. In order to enhance the dielectric permittivity of polymers, ceramic powders such as $Pb(Mg_{1/3}Nb_{2/3})O_3$-$PbTiO_3$(PMNT), $Pb(Zr,Ti)O_3$(PZT), $BaTiO_3$ (BT) [8–13] were used as fillers due to their high dielectric permittivity. Recently, $CaCu_3Ti_4O_{12}$ (CCTO) ceramic which has centrosymmetric *bcc* structure (space group Im3, lattice parameter $a \approx 0.7391$ nm, and $Z = 2$), has been used as a filler and studied to explore the possibility of obtaining high dielectric permittivity composites for potential capacitor applications [14–21]. It was reported that, the dielectric permittivity as high as 740 at 1 kHz was achieved for a composition of fixed concentration: 50 vol% CCTO and 50 vol% PVDF-TrFE [14]. The dielectric permittivity increases as the CCTO content increases

---

[*]Corresponding author, e-mail: kbrvarma@mrc.iisc.ernet.in

in the polymer and decreases as the frequency increases [15–17]. The reason for increased low frequency dielectric dispersion was attributed to high interfacial polarization triggered by high dielectric loss associated with CCTO [15].

The electrical properties of polymers can be altered/modified by the addition of inorganic nano fillers. Nanoscale particles are more attractive due to their intriguing properties arising from their size associated with large surface area. The insertion of nanoscale fillers may improve the electrical and dielectric properties of the host polymers and the properties can be tailored to a particular performance requirement [22]. But the final properties of a nanocomposite depend on the method of preparation, particle size and the effective dispersion of ceramic particles in the polymer matrix [23–26].

PVDF based composites are being studied in great detail [27–30] because of their better thermal stability, they are tough and can be easily processed by solution casting/injection moulding/melt technique. It is also a non-toxic material, exhibiting resistance to heat and chemicals and low water absorption characteristics which make it more suitable for making electronic components. PVDF, a semi-crystalline polymer exists in four different crystalline forms depending on the preparation conditions like solvent, melt temperature, method of casting, stretching of thin films and annealing conditions. The β-phase is the desirable phase owing to its ferroelectric nature. Phase I (β-phase) has a planar TTTT (all trans) zigzag chain conformation which has space group Cm2m (orthorhombic, $a = 0.858$ nm, $b = 0.491$ nm, $c = 0.256$ nm) [31–33].

In this work, we report the fabrication and characterization of PVDF/CCTO nano composite system, in which nanocrystallites of CCTO have been dispersed in PVDF solution (dimethyl sulfoxide) followed by spin coating technique for the first time. The composite thus developed has improved dielectric properties which perhaps could be exploited for the development of high energy density capacitors.

2. Experimental

2.1. Characterization

X-ray powder diffraction (XRD) studies were carried out using an XPERT-PRO Diffractometer (Philips, Netherlands) with CuK$_{\alpha1}$ radiation (λ = 0.154056 nm) in a wide range of 2θ (5°≤ 2θ ≤ 85°). The microstructure and morphology of the samples were characterized by using scanning electron microscope (FEI Thermal Field Emission SEM Sirion). Transmission Electron Microscopy (TEM) were carried out using FEI-Technai TEM (G-F30, Hillsboro, USA). For the electrical characterization, the films were cut into small pieces of 5×5 mm and gold electrodes with 3 mm radii were sputtered at the centre on both sides of each sample. The dielectric studies were carried out using an impedance gain-phase analyzer (HP4194A) as a function of frequency (100 Hz–1 MHz). The contacts were taken from both sides of the free standing films. The data generated from the instrument were collected through an interface between instrument and the computer using a software (developed in our laboratory). The measurement accuracy of the instrument is better than 5%. The dielectric permittivity was evaluated using the standard relation $\varepsilon_r = C{\cdot}d/\varepsilon_0 A$, where C = capacitance, d is the thickness of the sample, $\varepsilon_0 = 8.854{\cdot}10^{-12}$ F/m and A is the effective area of the sample. Dielectric strength measurements were carried out as per the procedure outlined in ASTM D 149.

2.2. Preparation of $CaCu_3Ti_4O_{12}$ nanoparticles

$TiCl_4$ (titanium tetrachloride, 99.98%) (Merck, Germany), calcium carbonate (BDH; A.R. grade, India), cupric chloride (Fluka, pro analysi grade, India), oxalic acid (s.d.fine-chem Ltd, A.R. grade, India), NH_4Cl and NH_4OH(aq) (BDH; A.R. grade, India) ethanol or acetone (Nice chemicals pvt ltd, India; 99.5% pure), dimethylacetamide (DMD) (Merck, Germany) and Poly vinylidene fluoride (PVDF), molecular weight of M_w 530 000, supplied by Sigma-Aldrich Chemicals pvt ltd, India. $CaCu_3Ti_4O_{12}$ (CCTO) nanoparticles were synthesized using complex oxalate precursor method [34]. In a typical preparation, titania gel was prepared from the aqueous $TiOCl_2$ (0.05 M) by adding NH_4OH(aq) (at 25°C) till the pH reached ~8.0 and NH_4Cl was washed off on a filter funnel. This gel was added to 0.4 or 0.8 moles of oxalic acid (2 M solution) (1:1 or 1:2 ratio of Ti:$C_2O_4^{2-}$) which was kept warm (~40°C). To the clear solution obtained, calcium carbonate was added in aliquots and stirred. An aqueous solution containing titanyl oxalic acid together with calcium titanyl oxalate remained clear without any precipitate formation.

This solution was cooled to 10°C to which cupric chloride dissolved in acetone along with water (80/20) was added and stirred continuously. The thick precipitate was separated out by further addition of acetone. Subsequently, the precipitate was filtered, washed several times with acetone to make it chloride-free and dried in air. The precursor was isothermally heated around 700°C to get nanocrystals (20–75 nm) of phase-pure calcium copper titanate, $CaCu_3Ti_4O_{12}$ as confirmed by X-ray diffraction and TEM studies.

2.3. Preparation of PVDF-$CaCu_3Ti_4O_{12}$ nanocrystal composite films

The composite was prepared by solution casting method. The PVDF polymer was dissolved in dimethyl sulfoxide (DMSO) and an appropriate amount of CCTO nanocrystals was added to the solution, which was thoroughly mixed with the solvent. The suspension was then poured onto a glass plate and then spun. The free standing composite films of thickness 85 µm were obtained and these were annealed at 90°C for 5 hours which would enable the crystallization of the β-phase of PVDF. The film thus obtained was then heated in a vacuum oven at 80°C for 12 h to remove any remaining traces of the solvent. Composite films with different volume percentages (5 to 30 vol%) of CCTO were prepared.

3. Results and discussion

3.1. X-ray diffraction studies

The X-ray diffraction patterns of PVDF, CCTO and series of PVDF/CCTO composites with different volume percents are shown in Figure 1. The diffraction peaks at 20.7° (200) and 20.8° (110) indicate that the PVDF exists in the β-phase [35]. Figure 1b shows the X-ray diffraction pattern obtained for the pure CCTO nano crystalline powder compared well with the ICDD data (01-075-1149) and with the pattern reported earlier [34]. The X-ray diffraction patterns obtained for the PDVF-CCTO (Figures 1c and 1d), reflect their composite nature. However, the peak intensity for β-phase of PVDF has decreased as compared to that of CCTO in the composites as the volume percent of CCTO increased in PVDF.

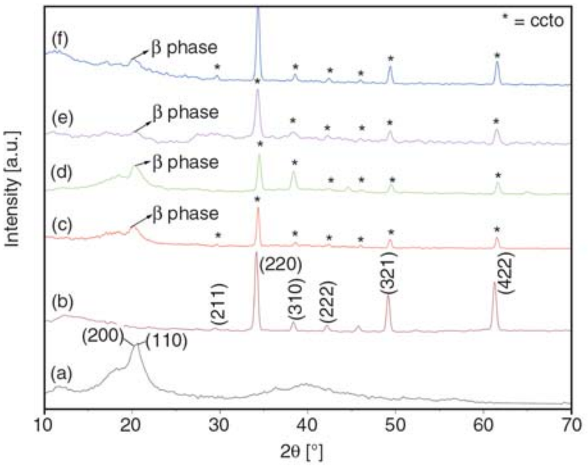

Figure 1. The XRD diffraction patters for: (a) PVDF, (b) CCTO nanocrystalline powder and PVDF-CCTO nanocrysta composites of various concentrations (c) 5 vol%, (d) 10 vol%, (e) 20 vol% and (f) 30 vol%

3.2. Morphology study by SEM/TEM

Figures 2a and 2b shows the bright field TEM image of nano powders of CCTO and the corresponding SAED pattern. Figure 2a presents the bright field TEM image of the CCTO nano powders obtained from the oxalate precursor and the size of the crystallite is in the range of 20–75 nm.

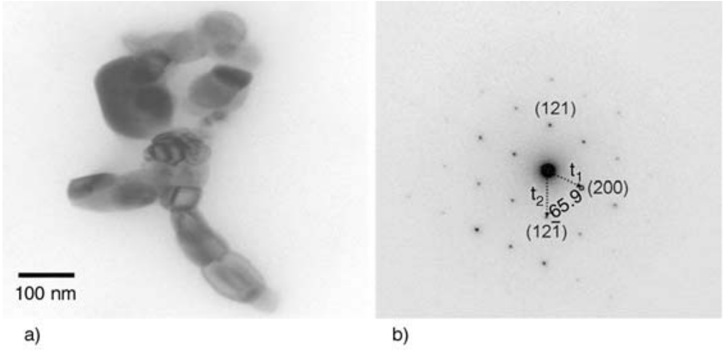

Figure 2. a) Bright field TEM images of CCTO nanocrystals with dimensions ranging from 20–75 nm, b) SAED pattern with the zone axis of [012], $t_2/t_1 = 1.229$

Figure 2b shows the selected area electron diffraction (SAED) pattern with the [012] zone axis. SAED pattern confirms the crystalline nature. The ratio of the reciprocal vectors (t_2/t_1) is around 1.229, approaching the calculated value of 1.225 for the bcc lattice.

Figure 3 shows the microstructure of the composite recorded for PVDF+30 vol% CCTO composite and the inset is for the PVDF+5 vol% CCTO composite. It is clear that the CCTO crystallites are uniformly distributed in this composite (inset). As the concentration is increased to 30 vol%, the CCTO nano crystallites have the tendency to agglomerate and its size is about 2 µm. Though the sizes of the CCTO crystallites remain the same in all the composites, only the size of the agglomerate is different. As revealed by SEM microstructure, the nanoparticles have the tendency to form clusters, which results in non-uniform distribution of the ceramic powder in the polymer matrix. Therefore, the present work has been restricted to 30 vol% of ceramic powder.

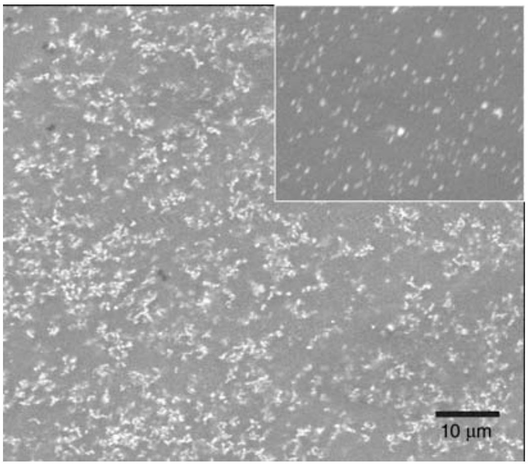

Figure 3. Scanning electron micrographs of PVDF+CCTO-30% nanocrystal composite exhibiting agglomerated CCTO nano crystallite. The inset is for PVDF+CCTO-5% composites with no agglomeration.

3.3. Frequency dependence of room temperature dielectric permittivity

The room temperature dielectric permittivity (ε_r') and the loss (tanδ) recorded as a function of frequency for PVDF/CCTO nanocomposites are shown in Figures 4a and 4b. The dielectric permittivity (Figure 4a) increases as the ceramic loading increases from 0 to 30% by volume at all the frequencies under study. It is clearly indicated that the introduction of CCTO nano crystallites in PVDF, increases the dielectric permittivity of the PVDF from 18 to 87 for 30 vol% of CCTO at 100 Hz. The dielectric permittivity decreases as the frequency increases from 100 Hz to 1 MHz. In all the cases, the dielectric permittivity values obtained are higher than that of pure PVDF, but much lower than that of pure CCTO [34]. The higher dielectric permittivity obtained in ceramic/polymer composites are attributed to the presence of CCTO nanocrystallites in the PVDF matrix and enhanced

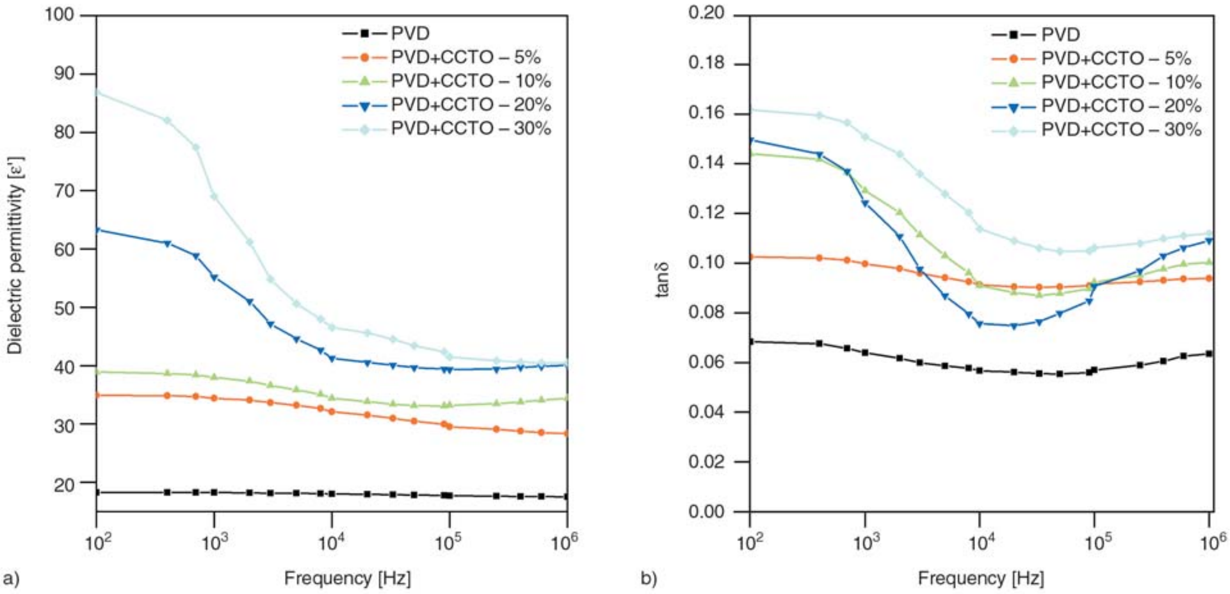

Figure 4. Frequency dependent (a) dielectric permittivity and (b) dielectric loss (tanδ) of PVDF-CCTO nanocomposite as a function of volume percent of CCTO at 300 K

polarization from dipole-dipole interaction of closely packed crystallites. The agglomeration formation is attributed to the van der Waals force existing among fine ceramic powders. The dielectric loss (Figure 4b) increases with the inclusion of CCTO nanocrystallites in the PVDF matrix. The composite with 30 vol% of CCTO nanocrystallites has the loss value of 0.16 (100 Hz). The dielectric loss decreases as the frequency increases. The dielectric loss is considerably higher especially at low frequencies, which is mainly attributed to inhomogeneous conduction vis-à-vis interfacial polarization.

3.4. Temperature dependence of dielectric properties

The temperature dependence of dielectric properties of PVDF and PVDF+CCTO-30% composites were studied and illustrated in Figures 5 and 6 respectively. Figure 5 shows the frequency dependent dielectric permittivity and loss at different temperatures for pure PVDF. Both the dielectric permittivity and the loss increase with increase in temperature, but decreases as the frequency increases. In the low frequency regime, the dielectric permittivity increased from 24 to 34 when the temperature is increased from 75 to 100°C and increased further (to 45) when the temperature is increased to 125°C. This sudden increase in dielectric permittivity that is observed at 100 Hz may be assigned to the space charge/interfacial polarization effects. The dielectric loss (Figure 5b) has increased from 0.063 to 0.49 as the temperature increased from 30 to 125°C. Similar observations were reported in the literature for pure PVDF [30].

Figures 6a and 6b) shows the frequency dependence of dielectric permittivity and the dielectric loss for PVDF+30 vol% CCTO composite at different temperatures (30 to 125°C). The dielectric permittivity increases with increase in temperature but decreases as the frequency increases. The room temperature dielectric permittivity is 87 at 100 Hz, which has increased to about 290 at 125°C (100 Hz). The value at 1 kHz is around 65, which has increased to 141 when the temperature is increased from 30 to 125°C. But the rise in dielectric permittivity with rise in temperature has decreased with increase in the frequency as shown in the Figure 6a. This behaviour is akin to that of pure PVDF except it has higher dielectric permittivity values as a result of the presence of CCTO nanocrystallites. The most visible change is noticed in the low frequency region (100 Hz–10 kHz) indicating the strong influence of interfacial polarization mechanism. The inset shows the variation (though it is not that significant as in the previous case) in dielectric permittivity in the 10 kHz to 1 MHz frequency range with respect to temperature. The PVDF/CCTO composite exhibits similar dielectric behaviour to that of pure PVDF. The frequency dependent dielectric loss at various temperatures is depicted in the Figure 6b. The dielectric loss increased from 0.17 to 0.53 as the temperature is increased from 30 to 125°C at 1 kHz.

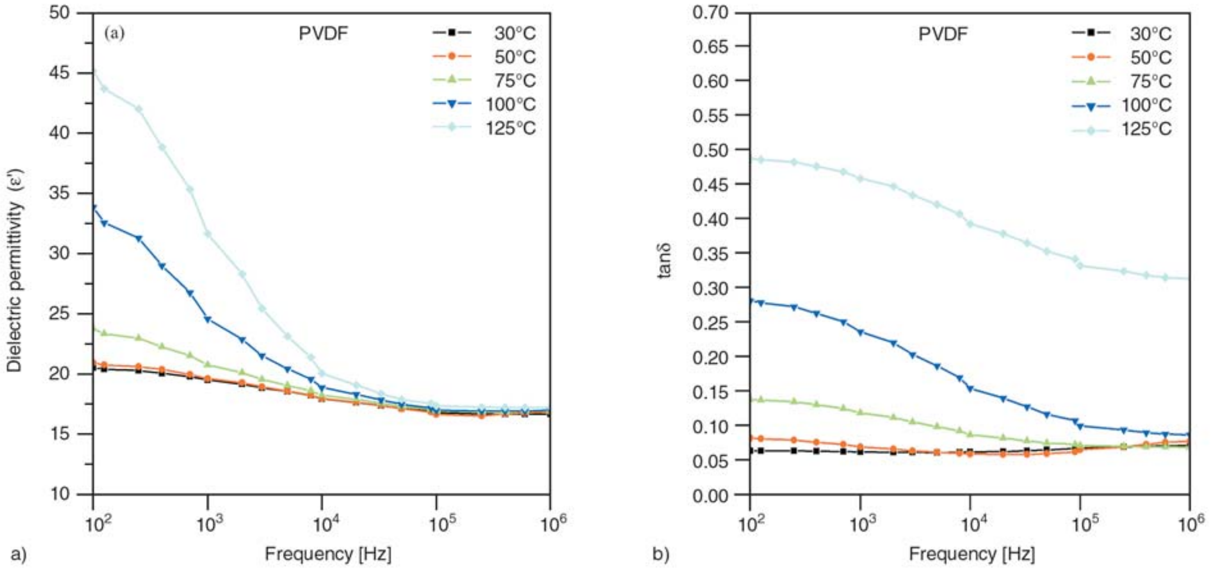

Figure 5. Frequency dependent (a) dielectric permittivity and (b) dielectric loss (tanδ) at various temperatures for PVDF

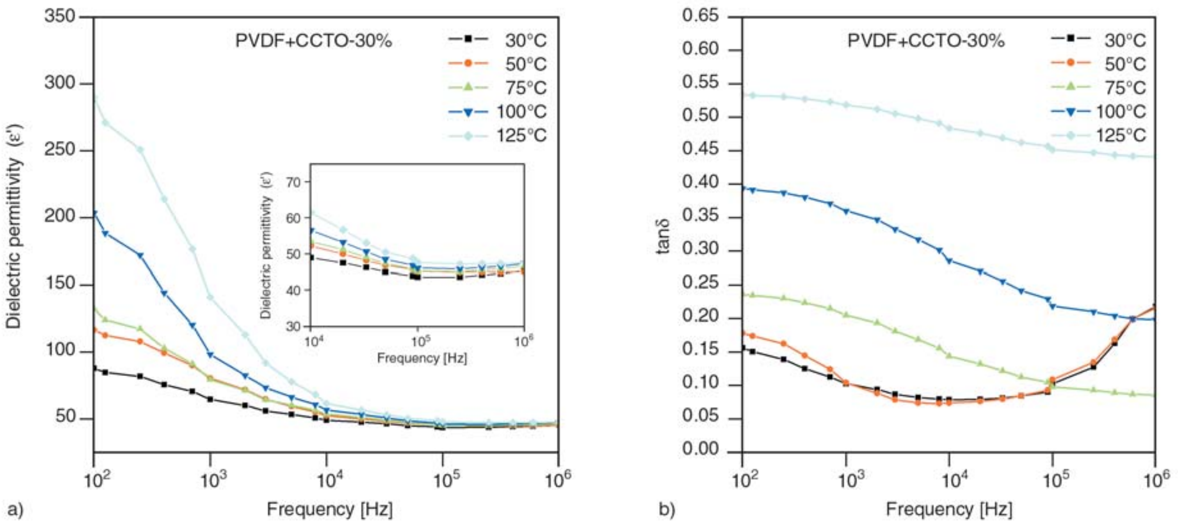

Figure 6. Frequency dependent (a) dielectric permittivity and (b) dielectric loss (tanδ) at various temperatures for PVDF+CCTO-30% nanocomposite

At low temperatures, the loss significantly increases subsequent to 1 MHz. At higher temperatures the sudden increases in loss may be beyond the frequency range that is covered in the present study.

The effective dielectric permittivity of polymer/filler composite material is dependent not only on the dielectric permittivity of the polymer and the filler, size and shape of the filler and the volume fraction of the filler, but also on the dielectric permittivity of the interphase region, volume of the interphase region and on the type of coupling agents. Hence, it is necessary to predict the dielectric permittivity by combining the theory and the experiment. Various models have been developed for the 0–3 composites [36–40].

The dielectric property of a diphasic dielectric mixture comprising of spherical crystallites with high dielectric permittivity dispersed in a matrix of low dielectric permittivity could be well described by Maxwell's model [36]. According to this model the effective dielectric permittivity of the composite is given by Equation (1):

$$\varepsilon_{eff} = \frac{\delta_p \varepsilon_p (2/3 + \varepsilon_c / 3\varepsilon_p) + \delta_c \varepsilon_c}{\delta_p (2/3 + \varepsilon_c / 3\varepsilon_p) + \delta_c} \tag{1}$$

where ε_c, ε_p, δ_c and δ_p and are the dielectric permittivity of CCTO, PVDF, the volume fraction of the dispersoid and the polymer, respectively. Here, the predicted value deviates much from that of the experimental value for all the volume fractions of CCTO under study.

The Maxwell and Furakawa theories were used as the basis for a new theory that was presented by Rayleigh [37]. In this model, the dielectric behaviour of the compsite is given by Equation (2):

$$\varepsilon_{eff} = \frac{2\varepsilon_p + \varepsilon_c + 2\delta_c(\varepsilon_c - \varepsilon_p)}{2\varepsilon_p + \varepsilon_c - \delta_c(\varepsilon_c - \varepsilon_p)} \tag{2}$$

where ε_c and ε_p are the dielectric permittivity of the matrix and ceramic particles, respectively, ε_{eff} is the effective dielectric permittivity and δ_c is the volume fraction of the ceramic particles. Here, again, it has been observed that the predicted value deviates much from that of the experimental value for all the volume fractions of CCTO under investigation.

The effective medium theory (EMT) model [38] has been established taking into account the morphology of the particles. According to which the effective dielectric permittivity is given by Equation (3):

$$\varepsilon_{eff} = \varepsilon_p \left(1 + \frac{\delta_c(\varepsilon_c - \varepsilon_p)}{\varepsilon_p + n(1-\delta_c)(\varepsilon_c - \varepsilon_p)} \right) \tag{3}$$

where δ_c is the volume fraction of the ceramic dispersed, ε_c, ε_p and n are the dielectric permittivity of the particle, polymer and the ceramic morphology fitting factor respectively. The small value of n indicates that the filler particles are of near-spherical shape, while a high value of n indicates largely non-spherical shaped particles. The shape parame-

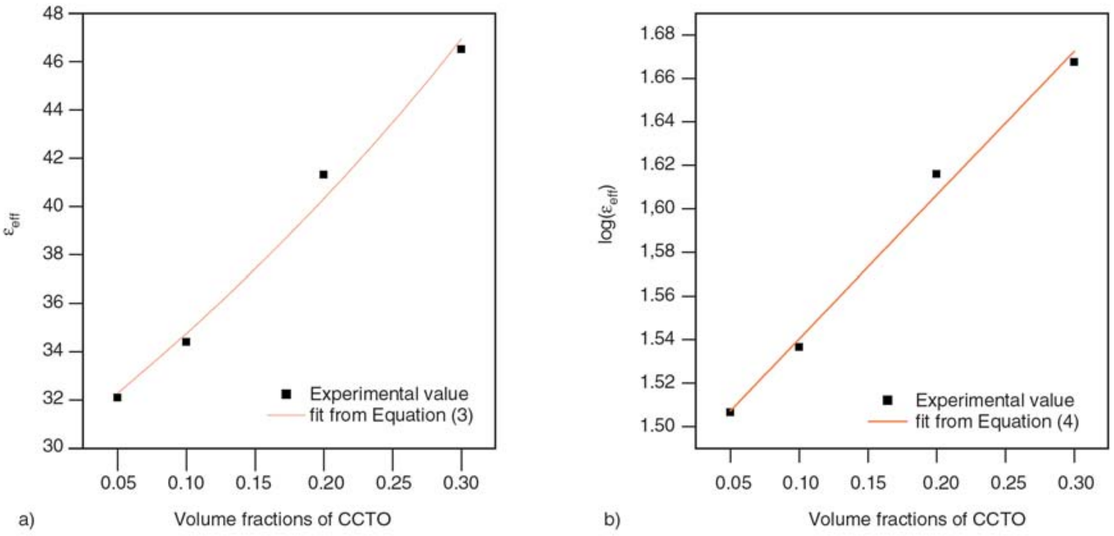

Figure 7. (a) Real permittivity as a function of volume fraction of CCTO. Dots are experimental data and the solid line is fit from the Equation (3) and (b) fit from the Equation (4).

ter obtained is around 0.49. The effective permittivity of PVDF-CCTO-30 composite computed using the above model for different volume fraction of CCTO is shown in Figure 7a. The experimental data are shown as filled squares.

Figure 7b gives the experimental data of permittivity as a function of filler volume fraction. Solid line is fit obtained for the Lichtenecker model (Equation (4)) given:

$$\log(\varepsilon_c) = V_m \cdot \log(\varepsilon_m) + 0.49 \cdot V_f \cdot \log(\varepsilon_f) \qquad (4)$$

where, ε_c, ε_m and ε_f are the dielectric permittivities of the composite, polymer matrix and the filler, V_m and V_f are the volume fractions of matrix and the filler respectively [19]. It is seen that, the effective permittivity values fitted from these models vary slightly since the shape parameter derived from these models also varies. Thus, it is concluded that the effective dielectric permittivity depends on the shape and size (need to be verified) of the filler particles.

The nano composite films were also studied for dielectric strength as per the procedure outlined in ASTM D 149 and the breakdown tests are carried out in a medium of air. The cylindrical electrodes (both top and bottom) of 6 mm in diameter and the sample was placed between the electrodes and the AC (50 Hz) voltage was continuously increased at a rate of 500 V/s till the sample broke down. Though the measurements were carried out in air, no flashover was noticed. The creepage distance calculated is given in the Table 1. The breakdown voltage, *V* [kV] of the samples were recorded and the dielectric strength, *E* [kV/mm] was calculated as *E* = *V*/*t*, where *t* is the thickness of the sample in millimeters. The electrical breakdown data obtained for the PVDF/CCTO nanocomposite films compared with the behaviour of the unfilled PVDF are presented as box and whisker plots (Figure 8). It is observed that (Figure 8), the pure PVDF films has higher electric strength compared to that of the composites. The nanocomposite dielectric strength decreases as the CCTO filler content increases from 5 to 30% by volume in the PVDF. Similar observations were reported for the other PVDF based composite systems [41, 42]. The introduction of fillers into the polymers generally introduces defects in the system causing centers of charge concentration leading to the lower dielectric strength [43]. Hence, the observed trend of decrease in the dielectric strength in the composites is attributed to the CCTO filler and its volume percent in the PVDF. It is also to be noted that the dielectric permittivity has an influence on the dielectric strength.

Table 1. Electric strength and creepage distance for the pure PVDF and PVDF+CCTO nanocrystal composites

Sl. No	Sample details	Electrode diameter	Electric strength, E [kV/mm]	Creepage distance
1	PVDF film	6 mm	64.2	16 mm
2	PVDF+CCTO-5%	6 mm	48.8	16 mm
3	PVDF+CCTO-10%	6 mm	35.1	16 mm
4	PVDF+CCTO-20%	6 mm	11.5	16 mm
5	PVDF+CCTO-30%	6 mm	7.9	16 mm

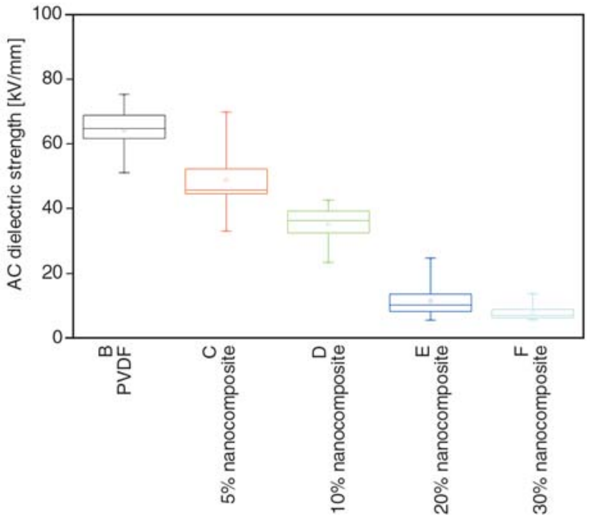

Figure 8. Variation of AC dielectric strength with respect to filler loading in PVDF-CCTO nanocrystal composites

When the breakdown strength is plotted against the dielectric permittivity, an inverse relationship of breakdown voltage to dielectric permittivity is evident [44]. It is also observed that the dielectric permittivity of the PVDF has increased from 18 to 87 as the volume percent of the CCTO increases. Hence, the decreasing trend of electric strength observed from 5 to 30% nanocomposites is attributed to the high dielectric permittivity associated with the CCTO ceramic. Higher dielectric permittivity associated with higher dielectric loss, act as the channels for charge leakage that lower the dielectric strength in the system.

In order to rationalize the temperature dependence of relaxation processes, electrical modulus approach was adopted. The real (M') and imaginary M'' parts of the electrical modulus obtained [45] as a function of temperature at fixed frequency of 5k Hz are shown in Figures 9a and 9b (Equation (5)):

$$\begin{aligned} M^* &= \frac{1}{\varepsilon^*} = \frac{1}{\varepsilon' - j\varepsilon''} = \\ &= \frac{\varepsilon'}{\varepsilon'^2 - \varepsilon''^2} + j\frac{\varepsilon''}{\varepsilon'^2 - \varepsilon''^2} = M' + jM'' \end{aligned} \qquad (5)$$

The M' values decrease as the filler content increases in the PVDF matrix (Figure 9a). The increase of the CCTO content results in lower values of M', implying that the real part of the dielectric permittivity increases with ceramic filler. The M'' obtained at the same frequency exhibits a relaxation process. The peak maximum value of M'' obtained decreases as the filler content increases from 10 to 30 volume percent in PVDF (Figure 9b) which is a characteristic of Maxwell-Wagner-Sillars (MWS) relaxation. Similar observations were made for the CCTO based composite systems where peak maximum value of M'' decreases as the filler content increases [19].

Figure 10a shows the variation of imaginary part of electrical modulus (M'') at various temperatures as a function of frequency for the PVDF+CCTO-30 composite. Two relaxation processes are clearly observed in the M'' curves. The low frequency M'' peak shifts towards higher frequency side with rise in temperature, but at high temperature one observes only one relaxation peak. There is a significant change in the relaxation peak height. The intensity

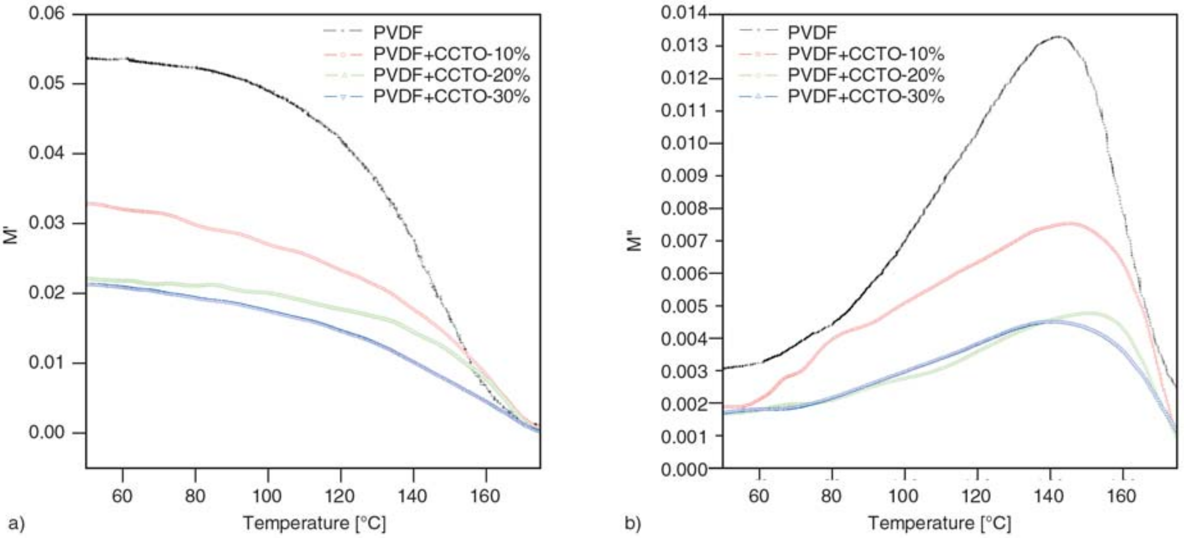

Figure 9. a) Real part (M') of electrical modulus vs. temperature for different volume percents of CCTO (at 5kHz); b) Imaginary part (M'') of electrical modulus vs. temperature for different volume percents of CCTO (at 5 kHz)

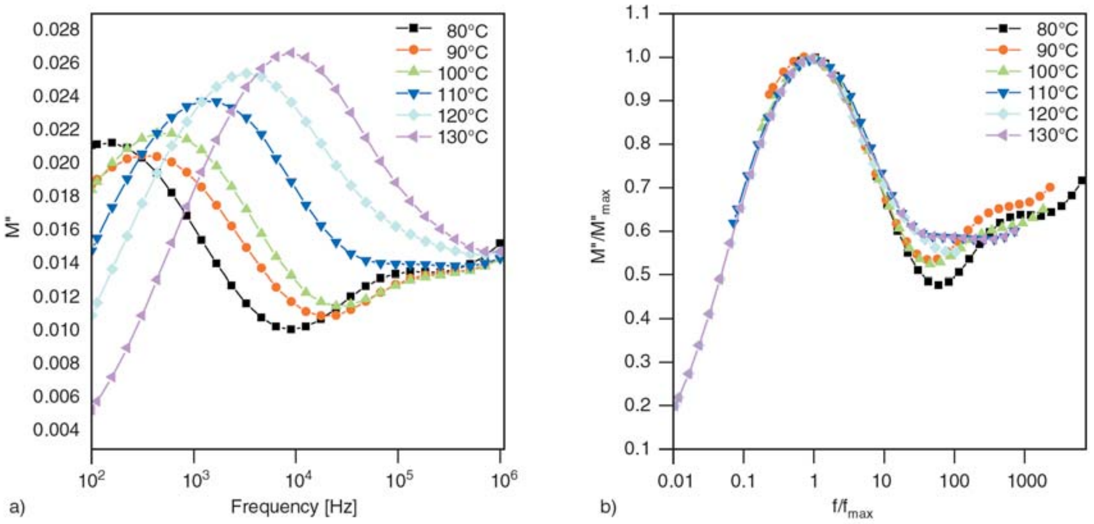

Figure 10. a) Electric modules spectra for PVDF+CCTO-30% nanocomposite at various temperatures as a function of frequency; b) Normalized plots of electric modulus against normalized frequency at various temperatures

of the low frequency relaxation peak is increased and shifts to higher frequency as the temperature increased. This relaxation is attributed to the interfacial or Maxwell-Wagner-Sillars (MWS) polarization which is normally encountered in heterogeneous materials [30]. These relaxation processes were influenced by the interfacial polarization effect which generated electric charge accumulation around the ceramic particles and the shift in the peak position to higher frequencies is attributed to the relaxation phenomena associated with PVDF. Figure 10b shows the normalized plots of electric modulus M'' versus frequency wherein the frequency is scaled by the peak frequency. A perfect overlapping of all the curves on a single master curve is not found at all the frequencies under study. This indicates that the relaxation process is temperature dependent.

The relaxation time associated with the process was determined from the plot of M'' versus frequency. The activation energy involved in the relaxation process is obtained from the temperature-dependent relaxation time (τ_{max}) (Equation (6)):

$$\tau_{max} = \tau_0 \exp\left(\frac{E_R}{kT}\right) \tag{6}$$

where E_R is the activation energy associated with the relaxation process, τ_0 is the pre-exponential factor, k is the Boltzmann constant and T is the absolute temperature. Figure 11 shows a plot between ln(τ) and 1000/T [K^{-1}] along with the theoretical fit

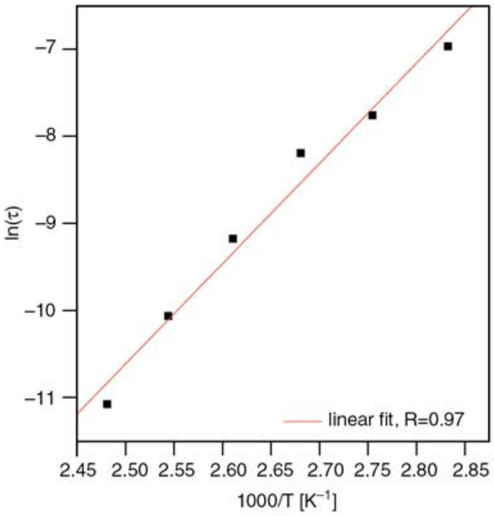

Figure 11. ln(τ_{max}) versus 1000/T [K^{-1}]

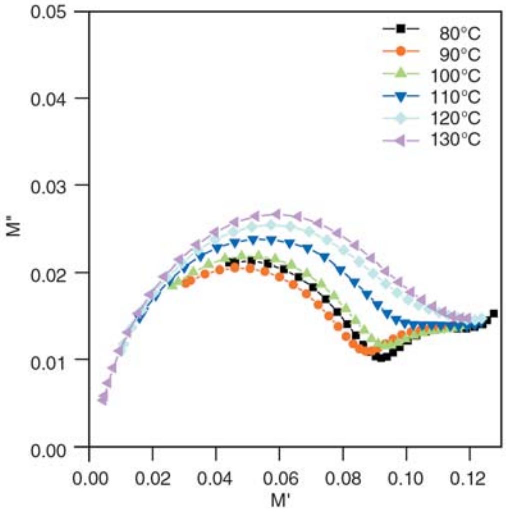

Figure 12. Cole-Cole plots of the electric modulus, M'' of the PVDF+CCTO-30 composite at various temperatures

(solid line) to the above equation (Equation (6)). The value that is obtained for E_R is 0.97±0.03 eV is attributed to the relaxation arising from the interfacial polarization.

In Figure 12, we show the Cole-Cole plot for the PVDF+CCTO-30 composite at various temperatures. In these plots, two distinct semicircles are clearly noticed. The high frequency end semicircle is attributed to the composite nature while the low frequency semicircle is attributed to the interfacial phenomenon occurring between the CCTO particles and the polymer.

4. Conclusions

High dielectric permittivity poly(vinylidene fluoride (PVDF)/$CaCu_3Ti_4O_{12}$ (CCTO) nanocrystal composite films were fabricated. The dielectric permittivity of PVDF increases with increase in CCTO content. The PVDF+CCTO-30% nanocomposite showed higher dielectric permittivity than that of pure PVDF and the other composites under study. The relaxation processes associated with these composites were attributed to the interfacial polarization or MWS effect. Though there is an improvement in the dielectric permittivity, the decrease in dielectric breakdown may limit its use for high voltage applications.

Acknowledgements

The management of Central Power Research Institute is acknowledged for the financial support. (Project No. 5.4.49). Thanks are due to Mr. Asai Thambi, Engineering officer, CPRI for breakdown voltage test.

References

[1] Newnham R. E.: Composite electroceramics. Annual Review of Materials Science, **16**, 47–68 (1986). DOI: 10.1146/annurev.ms.16.080186.000403

[2] Das-Gupta D. K.: Piezoelectricity and pyroelectricity. Key Engineering Materials, **92–93**, 1–14 (1994). DOI: 10.4028/www.scientific.net/KEM.92-93.1

[3] Dias C. J., Das-Gupta D. K.: Inorganic ceramic/polymer ferroelectric composite electrets. IEEE Transactions on Dielectric and Electrical Insulation, **3**, 706–734 (1996). DOI: 10.1109/94.544188

[4] Kuo D-H., Chang C-C., Su T-Y., Wang W-K., Lin B-Y.: Dielectric behaviours of multi-doped $BaTiO_3$/epoxy composites. Journal of the European Ceramic Society, **21**, 1171–1176 (2001). DOI: 10.1016/S0955-2219(00)00327-7

[5] Das-Gupta D. K., Doughty K.: Polymer-ceramic composite materials with high dielectric constants. Thin Solid Films, **158**, 93–105 (1988). DOI: 10.1016/0040-6090(88)90306-9

[6] Malecki J., Hilczer B.: Dielectric behaviour of polymers and composites. Key Engineering Materials, **92–93**, 181–216 (1994). DOI: 10.4028/www.scientific.net/KEM.92-93.181

[7] Chahal P., Tummala R. R., Allen M. G., Swaminathan M.: A novel integrated decoupling capacitor for MCM-L technology. IEEE Transaction on Components: Packaging, and Manufacturing Technology, **21**, 184–193 (1998). DOI: 10.1109/96.673707

[8] Bai Y., Cheng Z-Y., Bharti V., Xu H., Zhang Q. M.: High-dielectric-constant ceramic-powder polymer composites. Journal of Applied Physics Letters, **76**, 3804–3806 (2000). DOI: 10.1063/1.126787

[9] Adikary S. U., Chan H. L. W., Choy C. L., Sundaravel B., Wilson I. H.: Characterisation of proton irradiated $Ba_{0.65}Sr_{0.35}TiO_3$/P(VDF-TrFE) ceramic-polymer composites. Composites Science and Technology, **62**, 2161–2167 (2002). DOI: 10.1016/S0266-3538(02)00149-5

[10] Dang Z-M., Yu Y-F., Xu H-P., Bai J.: Study on microstructure and dielectric property of the $BaTiO_3$/epoxy resin composites. Composites Science and Technology, **68**, 171–177 (2008). DOI: 10.1016/j.compscitech.2007.05.021

[11] Sekar R., Tripathi A. K., Pillai P. K. C.: X-ray diffraction and dielectric studies of a $BaTiO_3$: PVDF composite. Materials Science and Engineering: B, **5**, 33–36 (1989). DOI: 10.1016/0921-5107(89)90302-4

[12] Muralidhar C., Pillai P. K. C.: Dielectric behaviour of barium titanate-polyvinylidene fluoride composites. Journal of Materials Science, **23**, 1071–1076 (1988). DOI: 10.1007/BF01154015

[13] Zhang Z-M., Shen Y., Nan C-W.: Dielectric behavior of three-phase percolative Ni-$BaTiO_3$/polyvinylidene fluoride composites. Journal of Applied Physics Letters, **81**, 4814–4816 (2002). DOI: 10.1063/1.1529085

[14] Arbatti M., Shan X., Cheng Z-Y.: Ceramic-polymer composites with high dielectric permittivity. Advanced Materials, **19**, 1369–1372 (2007). DOI: 10.1002/adma.200601996

[15] Shri Prakash B., Varma K. B. R.: Dielectric behavior of CCTO/epoxy and Al-CCTO/epoxy composites. Composites Science and Technology, **67**, 2363–2368 (2007).
DOI: 10.1016/j.compscitech.2007.01.010

[16] Tuncer E., Sauers I., James D. R., Ellis A. R., Paranthaman M. P., Tolga A. T., Sathyamurthy S., Karren L. M., Li J., Goyal A.: Electrical properties of epoxy resin based nanocomposites. Nanotechnology, **18**, 25703–25706 (2007).
DOI: 10.1088/0957-4484/18/2/025703

[17] Amaral F., Rubinger C. P. L, Henry F., Costa L. C., Valente M. A., Barros-Timmons A.: Dielectric properties of polystyrene-CCTO composite. Journal of Non Crystalline Solids, **354**, 5321–5322 (2008).
DOI: 10.1016/j.jnoncrysol.2008.05.056

[18] Thomas P., Dwarakanath K., Varma K. B. R.: In situ synthesis and characterization of polyaniline-$CaCu_3Ti_4O_{12}$ nanocrystal composites. Synthetic Metals, **159**, 2128–2134 (2009)
DOI: 10.1016/j.synthmet.2009.08.001

[19] Ramajo L. A., Ramírez M. A., Bueno P. R., Reboredo M. M., Castro M. S.: Dielectric behaviour of $CaCu_3Ti_4O_{12}$-epoxy composites. Materials Research, **11**, 85–88 (2008).
DOI: 10.1590/S1516-14392008000100016

[20] Patsidis A., Psarras G. C.: Dielectric behaviour and functionality of polymer matrix – ceramic $BaTiO_3$ composites. Express Polymer Letters, **2**, 718–726 (2008).
DOI: 10.3144/expresspolymlett.2008.85

[21] Thomas P., Varughese K. T. V., Dwarakanatha K., Varma K. B. R.: Dielectric properties of poly(vinylidene fluoride)/$CaCu_3Ti_4O_{12}$ composites. Composites Science and Technology, **70**, 539–545 (2010).
DOI: 10.1016/j.compscitech.2009.12.014

[22] Nalwa H. S.: Handbook of low and high dielectric permittivity materials and their applications, phenomena, properties and applications. Academic Press, San Diego (1999).

[23] Chiang C. K., Popielarz R.: Polymer composites with high dielectric permittivity. Ferroelectrics, **275**, 1–9 (2002).
DOI: 10.1080/00150190214285

[24] Hsiang H-I., Yin K-Y., Yen F-S., Hwang C-Y.: Effects of particle size of $BaTiO_3$ powder on the dielectric properties of $BaTiO_3$/polyvinylidene fluoride composites. Journal of Materials Science, **36**, 3809–3815 (2001)
DOI: 10.1023/A:1017946405447

[25] Ishida H., Campbell S., Blackwell J.: General approach to polymer nanocomposite preparation. Chemistry of Materials, **12**, 1260–1267 (2000).
DOI: 10.1021/cm990479y

[26] Kontos G. A., Soulintzis A. L., Karahaliou P. K., Psarras G. C., Georga S. N., Krontiras C. A., Pisanias M. N.: Electrical relaxation dynamics in TiO_2-polymer matrix composites. Express Polymer Letters, **1**, 781–789 (2007).
DOI: 10.3144/expresspolymlett.2007.108

[27] Djidjelli H., Benachour D., Boukerrou A., Zefouni O., Martinez-Véga J., Farenc J., Kaci M.: Thermal, dielectric and mechanical study of poly (vinyl chloride)/olive pomace composites. Express Polymer Letters, **1**, 846–852 (2007).
DOI: 10.3144/expresspolymlett.2007.117

[28] Muralidhar C., Pillai P. K. C.: Dielectric behaviour of barium titanate ($BaTiO_3$)/polyvinylidene fluoride (PVDF) composite. Journal of Materials Science Letters, **6**, 346–348 (1987).
DOI: 10.1007/BF01729348

[29] Dang Z-M., Wang H-Y., Zhang Y-H., Qi J-Q.: Morphology and dielectric property of homogenous $BaTiO_3$/PVDF nanocomposites prepared via the natural adsorption action of nanosized $BaTiO_3$. Macromolecular Rapid Communications, **26**, 1185–1189 (2005).
DOI: 10.1002/marc.200500137

[30] Chanmal C. V., Jog J. P.: Dielectric relaxations in PVDF/$BaTiO_3$ nanocomposites. Express Polymer Letters, **2**, 294–301 (2008).
DOI: 10.3144/expresspolymlett.2008.35

[31] Lando J. B., Olf H. G., Peterlin A.: Nuclear magnetic resonance and X-ray determination of the structure of poly(vinylidene fluoride). Journal of Polymer Science Part A-1: Polymer Chemistry, 4, 941–951 (1966).
DOI: 10.1002/pol.1966.150040420

[32] Hasegawa R., Takahashi Y., Chatani Y., Tadokoro H.: Crystal structures of three crystalline forms of poly(vinylidene fluoride). Polymer Journal, **3**, 600–610 (1972).
DOI: 10.1295/polymj.3.600

[33] Weinhold S., Litt M. H., Lando J. B.: The crystal structure of the γ phase of poly(vinylidene fluoride). Macromolecules, **13**, 1178–1183 (1980).
DOI: 10.1021/ma60077a029

[34] Thomas P., Dwarakanath K., Varma K. B. R., Kutty T. R. N.: Synthesis of nanoparticles of the giant dielectric material, $CaCu_3Ti_4O_{12}$ from a precursor route. Journal of Thermal Analysis and Calorimetry, **95**, 267–272 (2009).
DOI: 10.1007/s10973-007-8981-z

[35] Esterly M. D., Love B. J.: Phase transformation to β-poly(vinylidene fluoride) by milling. Journal of Polymer Science Part B: Polymer Physics, **42**, 91–97 (2004).
DOI: 10.1002/polb.10613

[36] Maxwell J. C.: A treatise on electricity and magnetism. Dover Publications, New York (1954).

[37] Bhimsankaran T., Suryanarayana S. V., Prasad G.: Piezoelectric polymer composite materials. Current Science, **74**, 967–976 (1998).

[38] Rao Y., Qu J., Marinis T., Wong C. P.: A precise numerical prediction of effective dielectric permittivity for polymer-ceramic composite based on effective-medium theory. IEEE Transactions on Components and Packaging Technologies, **23**, 680–683 (2000).
DOI: 10.1109/6144.888853

[39] Yamada T., Ueda T., Kitayama T.: Piezoelectricity of a high-content lead zirconate titanate/polymer composite. Journal of Applied Physics, **53**, 4328–4332 (1982).
DOI: 10.1063/1.331211

[40] Lunkenheimer P., Fichtl P., Ebbinghaus S. G., Loidl A.: Nonintrinsic origin of the colossal dielectric constants in $CaCu_3Ti_4O_{12}$. Physical Review B, **70**, 172102–172105 (2004).
DOI: 10.1103/PhysRevB.70.172102

[41] Dou X., Liu X., Zhang Y., Feng H., Chen J-F., Du S.: Improved dielectric strength of barium titanate-polyvinylidene fluoride nanocomposite. Applied Physics Letters, **95**, 132904–132906 (2009).
DOI: 10.1063/1.3242004

[42] Aulagner E., Guillet J., Seytre S., Hantouche C., Le Gonidec P., Terzulli G.: (PVDF/$BaTiO_3$) and (PP/$BaTiO_3$) films for energy storage apacitors. in 'IEEE 5th International Conference on Conduction and Breakdown in Solid Dielectrics, Leicester, England' 423–427 (1995).
DOI: 10.1109/ICSD.1995.523021

[43] Singha S., Thomas M. J.: Dielectric properties of epoxy nanocomposites. IEEE Transactions on Dielectrics and Electrical Insulation, **15**, 12–23 (2008).
DOI: 10.1109/T-DEI.2008.4446732

[44] McPherson J., Kim J-Y., Shanware A., Mogul H.: Thermochemical description of dielectric breakdown in high dielectric constant materials. Applied Physics Letters, **82**, 2121–2123 (2003).
DOI: 10.1063/1.1565180

[45] Ramajo L., Reboredo M., Castro M.: Dielectric response and relaxation phenomena in composites of epoxy with $BaTiO_3$ particles. Composites Part A: Applied Science and Manufacturing, **36**, 1267–1274 (2005).
DOI: 10.1016/j.compositesa.2005.01.026

eXPRESS Polymer Letters Vol.4, No.10 (2010) 644–658
Available online at www.expresspolymlett.com
DOI: 10.3144/expresspolymlett.2010.79

Healing of fatigue crack in epoxy materials with epoxy/mercaptan system via manual infiltration

Y. C. Yuan[1,3], M. Z. Rong[1], M. Q. Zhang[2*], G. C. Yang[1], J. Q. Zhao[3]

[1]Key Laboratory for Polymeric Composite and Functional Materials of Ministry of Education, DSAPM Lab, School of Chemistry and Chemical Engineering, Sun Yat-sen University, Guangzhou 510275, P. R. China
[2]Materials Science Institute, Zhongshan University, Guangzhou 510275, P. R. China
[3]College of Materials Science and Engineering, South China University of Technology, Guangzhou 510640, P. R. China

Received 12 May 2010; accepted in revised form 21 June 2010

Abstract. The present work verified the capability of epoxy/mercaptan/tertiary amine system for retarding and/or arresting fatigue cracks in epoxy materials subjected to cyclic loading at room temperature. By using static and dynamic manual infiltration methods, the effects of hydrodynamic pressure crack tip shielding, polymeric wedge and adhesive bonding of the healing agent were revealed. Depending on the applied stress intensity range and the competition between polymerization kinetics of the healing agent and crack growth rate, the above mechanisms exerted different influences on crack retardation under different circumstances. On the whole, the epoxy/mercaptan/tertiary amine system proved to be very effective in obstructing fatigue crack propagation. It formed a promising base for developing self-healing epoxy materials that enable *in-situ* autonomic rehabilitation of fatigue crack.

***Keywords:** smart polymers, fracture and fatigue, self-healing, epoxy*

1. Introduction

Fatigue and fatigue failure are critical for polymeric materials used in structural applications. Under fatigue loading, cracks might slowly grow above a threshold range of stress intensity, ΔK_{th}, which is significantly lower than the critical stress intensity, K_{IC}. Therefore, imparting self-healing capability to polymers and polymer composites is an effective way to solve the problem [1–8]. It is hoped that the cracks can be autonomously eliminated soon after their emergence.

Earlier studies on metals have shown that infiltrating proper substances into a fatigue crack could induce crack growth retardation and even crack arrest [9–16]. Recently, Brown *et al.* [4] established a protocol to extend fatigue life of epoxy using dicyclopentadiene (DCPD). Viscous flow of DCPD in the crack plane retarded crack growth, and its polymerized version further acted as a wedge at the crack tip for artificial crack closure. On the basis of this pilot research, they prepared self-healing epoxy with embedded DCPD-loaded microcapsules and particulate Grubbs' catalyst, which was capable of responding to propagating fatigue cracks by autonomic processes that led to higher endurance limit and life extension, or even complete arrest of cracking [5–8], in addition to the ability to repair the cracks generated by monotonic fracture [17].

In fact, epoxy resin has been employed as infiltrant material for obstructing fatigue crack development in metals [9–13]. It has the advantages like good adhesiveness, low cure shrinkage, broad compatibility, corrosion and chemical resistance, strength and durability. In particular, the epoxy/mercaptan/tertiary amine system (the basis of '5-min epoxies') is highly reactive. It can come to a practical han-

---

[*] Corresponding author, e-mail: ceszmq@mail.sysu.edu.cn

dling strength in minutes at room temperature and develop useful bond strengths at ambient temperatures as low as –20°C. Therefore, it should be favorable for repairing fatigue damages under cyclic loading.

In our previous work, self-healing epoxy composites containing dual encapsulated healant, i.e. two types of microcapsules that respectively include epoxy prepolymer as the polymerizable component and mercaptan/tertiary amine catalyst as the hardener, were made [18–21]. Upon fracture the unreacted epoxy can be bled into damage sites together with the hardener fluid and then polymerized to repair cracks. The system proved to work in the case of monotonic fracture as characterized by the attractive healing effect even below room temperature. As a continuation of our project, the present work is focused on examination of the performance of the epoxy/mercaptan/tertiary amine system in suppression and rehabilitation of fatigue crack in epoxy materials via manual infiltration. Effect of adhesive curing process on fatigue crack propagation was systematically studied. The results are expected to provide a knowledge frame for the subsequent *in-situ* self-healing that has the practical value for engineering application.

2. Experimental

2.1. Materials and specimen preparation

Tapered double cantilever beam (TDCB) specimens were cast from the mixture of epoxy resin (EPON 828, diglycidyl ether of bisphenol A, Hexion Specialty Chemicals, USA) and 12.5 pph curing agent (diethylenetriamine, DETA, Shanghai Medical Group Reagent Co., China). The mixture was degassed, poured into a closed silicone rubber mold and cured for 24 h at room temperature, followed by 48 h at 40°C. Table 1 shows the material properties.

Table 1. Properties of the cured epoxy (EPON 828/DETA)

Properties	Data
Density [kg/m^3]	1172
K_{IC} [MPa·m$^{1/2}$]	0.587±0.016
Tensile strength [MPa]	42.3±0.4
Young's modulus [GPa]	3.7±0.2
*Paris power law exponent, n	7.12
*Paris power law constant, C_o	0.11

*Note: n and C_o were obtained according to Equation (3). The data well agree with those reported in ref. [23].

The healing agent consists of epoxy (1:1 mixture by weight of EPON 828 and diglycidyl ether of resorcin (J-80, Wuxi Resin Factory of Bluestar New Chemical Materials Co., China)) and the hardener (pentaerythritol tetrakis (3-mercaptopropionate) (PMP, Fluka Chemie AG, Switzerland) and 2,4,6-tris(dimethylaminomethyl)phenol (DMP-30, Shanghai Medical Group Reagent Co., China). Weight ratio of epoxy/mercaptan/tertiary amine = 6/5/1.

2.2. Mechanical testing and characterization

Fatigue crack propagation behavior of epoxy specimens was investigated using the aforesaid TDCB specimen geometry (with groove length of 55 mm) [4, 21, 22] on a Shimadzu Air Servo Fatigue and Endurance Testing System ADT-AV02K1S5 with 2 kN load cell at room temperature (24±1°C). Specimens were pre-cracked (0.5–1.5 mm) with a razor blade while ensuring the pre-crack tip was centered in the groove and then pin loaded. A triangular waveform of frequency 5 Hz was applied with a stress ratio ($R = K_{\min}/K_{\max}$, where $K_{\min}$ and $K_{\max}$ denote the minimum and maximum values of the cyclic stress intensity, respectively) of 0.1, unless otherwise specified for the examination of the impact of R. Fatigue cracks were grown within constant mode-I stress intensity factor range, ΔK_I ($\Delta K_I = K_{\max} - K_{\min}$). Load line crack opening displacement (COD) was measured by a clip gauge. Crack lengths were measured optically and by specimen compliance [23].

Due to the complexity of healing a growing crack under fatigue circumstances, retardation and arrest of fatigue cracks were found to be dependent on the range of applied cyclic stress intensity, ΔK_I, as well as the competition between polymerization kinetics of the healing agent and crack growth rate [5–8]. Accordingly, static and dynamic infiltration experiments were designed and conducted as follows. For the static one, after a crack growth increment of ~8 mm, both the growth rate and crack closure response settled down to steady state values. At this point, about 0.5 μl of pre-mixed healing agent was injected into the crack plane by using a microsyringe. The mixing of the components of the healing agent took about 30 sec and the injection was completed within 10 sec. All the times were calculated from the start time of mixing of the healant (i.e. 0′, the single quotation mark represents minute hereinafter). The healing agent flowed backward and forward in the fracture plane and instantaneously evenly penetrated into the crack. After 10 seconds, the test was stopped and the crack held open at a constant load level. Fatigue loading was reestablished after a prescribed steady-state healing period. In the case of dynamic experiments, the testing procedures were the same as those applied for the static ones, except that fatigue loading wasn't interrupted after the manual infiltration.

The constant ΔK nature of the fatigue test yielded a constant crack growth rate over the majority of the length of the specimen [4]. Experimental errors mainly came from the initial stage of cracking because of a slight deflection of the pre-crack. In order to reduce data discreteness, the data within 2 mm of initial crack length (a = 19–21 mm) were discarded for all the specimens except those the healing agent had repaired. For each test, the result was an average of four specimens.

The healing efficiency, λ, was defined by fatigue life extension [4], defined by Equation (1):

$$\lambda = \frac{N_{Control} - N_{Healed}}{N_{Control}} \qquad (1)$$

where N_{Healed} and $N_{Control}$ denote the total number of cycles to failure of a healed specimen and that of a similar specimen without healing, respectively.

To evaluate fracture toughness, K_{IC}, of the cured epoxy (i.e. EPON 828/DETA), a natural pre-crack (~2 mm) was created on the TDCB specimen by inserting a fresh razor blade and gently tapping into the molded notch starter [21]. Subsequently, the specimen was pin loaded and tested with a Hounsfied H10 KS universal testing machine under displacement control using a 3 mm/min displacement rate at room temperature. For determination of fracture toughness, K_{IC}, of the cured healing agent, the epoxy TDCB specimen made of EPON 828/DETA was fractured only to the end of the groove and then about 3 µl of uniformly pre-mixed healing agent (i.e. EPON 828/J-80/PMP/DMP-30) was injected into the cracked face. Afterwards, the specimen was unloaded and left to cure for different times at room temperature. A natural pre-crack (2–10 mm) along the original crack route was rapidly created within one minute before the next test. Finally, the healed specimen was tested again following the above procedure.

Isothermal curing kinetics of the healing agent was studied with a TA differential scanning calorimeter (DSC) Q10 calorimeter in N_2 at 25°C. Morphological observation of the fracture surfaces was conducted on a Hitachi Model S-4800 field emission scanning electron microscope (SEM).

3. Results and discussion

3.1. Hydrodynamic pressure crack-tip shielding

Researches on fatigue crack propagation of metals immersed in fluid revealed that the forces required to squeeze the fluid out of the crack during unloading and to draw the fluid into the crack during loading provided effective crack-tip shielding [24–27]. Such a hydrodynamic pressure effect decreases the effective mode-I stress intensity factor range, ΔK_{eff}, reduces fatigue crack growth rate and extends fatigue life. The Equation (2) can explain this mechanism:

$$\Delta K_{eff} = \Delta K_I - \Delta K_{opening} - \Delta K_{closure} \qquad (2)$$

where $\Delta K_{opening}$ and $\Delta K_{closure}$ refer to the crack-opening and crack-closure stress intensities from viscosity resistance of the liquid, respectively. In general, a fluid with higher viscosity leads to greater reduction in crack growth rate, until an upper limit is reached and the fluid can no longer penetrate to the crack tip [4, 24].

Like most polymers, the rate of steady-state fatigue crack growth of cured epoxy under constant applied range of stress intensity, ΔK_I, can be described by the Paris power law [28], given by Equation (3):

$$\frac{\mathrm{d}a}{\mathrm{d}N} = C_o \Delta K_I^n \qquad (3)$$

where C_o and n are materials constants.

Figure 1 shows the dependence of fatigue crack length on loading cycle. On the basis of this dependence and the data in Table 1 as well, one can estimate the fatigue crack growth rate via Equation (3). Here in this work, the hydrodynamic pressure crack-tip shielding mechanism is investigated by infiltrating the polymerizable component of the healing agent (i.e. the 1:1 mixture by weight of EPON 828 and J-80, excluding the hardener) into the crack plane of the specimen without interrupting the fatigue experiment (i.e. dynamic infiltra-

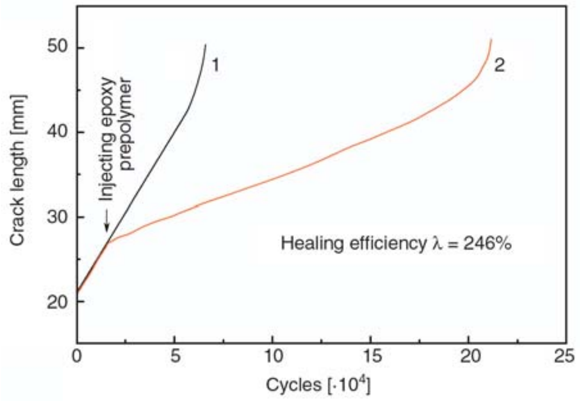

Figure 1. Crack length vs. fatigue cycles of (1) control fatigue specimen and (2) fatigue specimen with manual injection of epoxy prepolymer in dynamic infiltration fashion. Testing conditions: $K_{\max} = 0.504$ MPa·m$^{1/2}$, $K_{\min} = 0.050$ MPa·m$^{1/2}$, $\Delta K_I = 0.454$ MPa·m$^{1/2}$, $R = 0.1$.

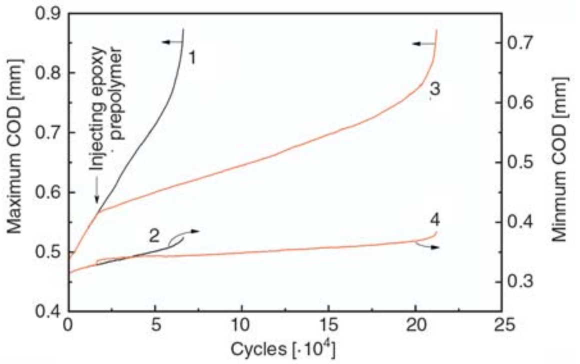

Figure 2. Maximum and minimum CODs vs. fatigue cycles of (1, 2) control fatigue specimens and (3, 4) fatigue specimens with manual injection of epoxy prepolymer in dynamic infiltration fashion. Testing conditions: $K_{\max} = 0.504$ MPa·m$^{1/2}$, $K_{\min} = 0.050$ MPa·m$^{1/2}$, $\Delta K_I = 0.454$ MPa·m$^{1/2}$, $R = 0.1$.

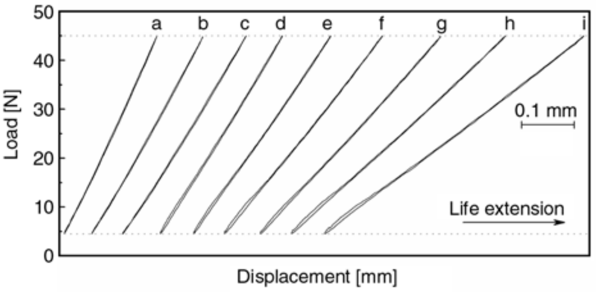

Figure 3. Load-displacement curves measured during selected cycles in Figure 2. Number of the fatigue cycles and the time after the manual infiltration of epoxy prepolymer: (a) 300; (b) 9900; (c) 16 200, 0′; (d) 17 100, 3′; (e) 50 100, 113′; (f) 99 900, 279′; (g) 150 000, 446′; (h) 200 100, 613′; and (i) 211 800, 652′. 0′ means the time when the epoxy prepolymer is injected. Testing conditions: $K_{\max} = 0.504$ MPa·m$^{1/2}$, $K_{\min} = 0.050$ MPa·m$^{1/2}$, $\Delta K_I = 0.454$ MPa·m$^{1/2}$, $R = 0.1$.

tion, see Experimental). For the control experiment, fatigue crack is grown in the specimen without injection until failure occurs (refer to curve 1 in Figure 1, $N_{Control} = 6.6\cdot10^4$ cycles). It is seen from Figure 1 that the slope of the crack length vs. fatigue cycles curve remains constant prior to the infiltration, suggesting a constant growth rate of approximately $3.8\cdot10^{-4}$ mm/cycle. After the infiltration, the crack growth rate is greatly reduced by 77% to $8.9\cdot10^{-5}$ mm/cycle. Like the case of submerged specimens [29], the subsequent crack propagation is also steady on the whole. According to Equation (1), the fatigue life-extension, λ, is calculated to be 246%.

For metals, crack-tip shielding from hydrodynamic pressure provides about 50% reduction in crack growth rate. As for microcapsule-toughened epoxy specimen, infiltration of an inert mineral oil to the crack plane leads to λ = 101% [4]. Coupled with our data in Figure 1, it is understood that the hydrodynamic pressure mechanism resulting from viscous fluid operates more efficiently in polymeric materials. Further study in this aspect is needed to reveal the underlying factor.

In fact, the marked post-infiltration drop in the crack growth rate indicates that filling the crack with the epoxy prepolymer has a fair effect on the reduction in the crack-tip stress intensity, and thus lowers the crack growth rate. The maximum and minimum values of crack opening displacement (COD) and the corresponding load-displacement curves shown in Figures 2 and 3 further illustrate this variation trend. In contrast to the situation prior to the infiltration, the fatigue crack in the presence of the injected epoxy prepolymer cannot be fully opened at the maximum load, leading to a remarkably lower crack growth rate over a long period of time (curve 3 in Figure 2). In addition, the crack also cannot be fully closed at the minimum load and the COD values become nearly independent of fatigue cycles (curve 4 in Figure 2). As a result, hysteresis loops appear on the load-displacement relationship between the initial phase of crack opening and the end phase of crack closing (curves d–i in Figure 3). Obviously, the hysteresis resistance offered by the viscous epoxy prepolymer raises $\Delta K_{opening}$ and $\Delta K_{closure}$, and hence decreases ΔK_{eff} as indicated in Equation (2).

With respect to the hardener component of the healing agent (i.e. the mixture of PMP and DMP-30), it exhibited approximately the same hydrodynamic pressure crack-tip shielding effect and fatigue life-extension ability as epoxy prepolymer, probably because of their similar viscosities. Further research in this aspect is needed to reveal the reasons.

3.2. Effects of cured wedge and its adhesiveness revealed by static infiltration tests

Following the traditional crack closure concept, it is known that if the fatigue crack opening load is purposely increased by a wedge with adhesive properties at the crack tip, the effective stress intensity factor range would be reduced accordingly [9–13], as shown by Equation (4):

$$\Delta K_{eff} = \Delta K_I - \Delta K_{bonding} - \Delta K_{wedge} \tag{4}$$

where $\Delta K_{bonding}$ refers to the stress intensity due to the combined (tensile) stresses in adhesives across the crack faces, and ΔK_{wedge} refers to the crack-closure stress intensity due to the wedge from adhesives gelling and hardening. With this idea in mind, a number of investigations were carried out by artificially introducing crack surface contact [4, 9–16]. It can be concluded that size and performance of the wedge are the most crucial factors affecting the crack closure effect.

In this work, the pre-mixed epoxy based healing agent was injected into the crack plane forming a crosslinked epoxy wedge. The wedge size was adjusted by changing the load level required for holding the crack open after the infiltration, while the wedge performance was tuned by changing the steady-state healing time, during which cyclic loading paused and crack held open (see the Experimental for more details).

Figures 4 and 5 show the representative crack length versus fatigue cycles of the specimens healed at constant applied stress intensities, K, and the dependence of healing efficiency on K, respectively. Sharp *et al.* [11] indicated that the load level or stress intensity applied for holding the crack open played a decisive role in retarding or arresting fatigue crack. Evidently, it is true for the current system. Fatigue crack growth is retarded at different K values (Figure 4). Higher stress intensity applied during healing results in more prominent retardation effect (i.e. higher healing efficiency). When the applied stress intensity is not less than 0.392 MPa·m$^{1/2}$, crack can hardly advance for more than 10^7 cycles and is considered to be completely arrested. Therefore, the applied stress intensity of 0.392 MPa·m$^{1/2}$ represents a watershed between fatigue crack growth retardation and crack arrest (Figure 5). The above results can be understood by the fact that thicker wedge is produced when the specimen is healed at higher applied stress intensity. Consequently, ΔK_{wedge} increases and ΔK_{eff}

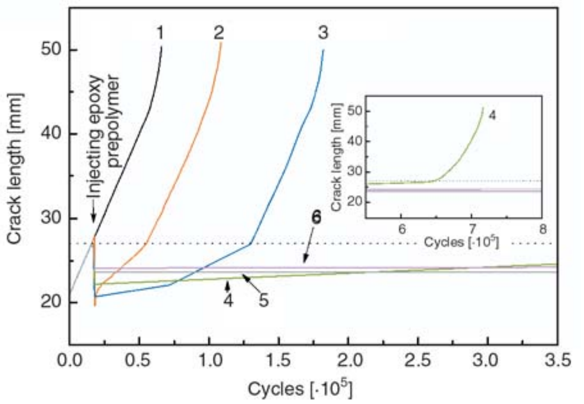

Figure 4. Crack length vs. fatigue cycles of (1) control fatigue specimen and (2–6) fatigue specimens with manual injection of pre-mixed healing agent in static infiltration fashion. The applied constant stress intensity for holding crack open after the injection: (2) 0, (3) 0.112 MPa·m$^{1/2}$, (4) 0.224 MPa·m$^{1/2}$, (5) 0.336 MPa·m$^{1/2}$, and (6) 0.392 MPa·m$^{1/2}$. The steady-state healing time: 10 min. Testing conditions: K_{max} = 0.504 MPa·m$^{1/2}$, K_{min} = 0.050 MPa·m$^{1/2}$, ΔK_I = 0.454 MPa·m$^{1/2}$, R = 0.1.

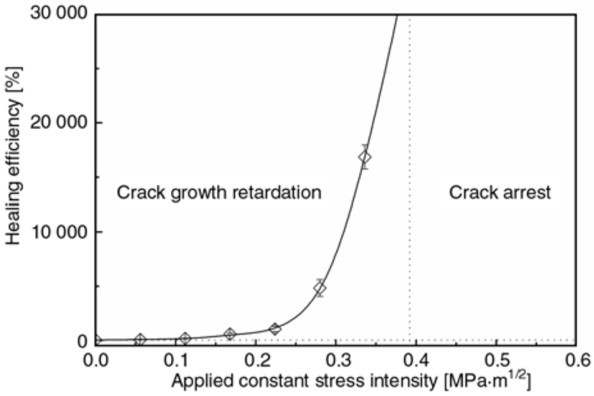

Figure 5. Healing efficiency of fatigue specimens with manual injection of pre-mixed healing agent in static infiltration fashion vs. the applied constant stress intensity for holding crack open after the injection. The data are calculated using the results in Figure 4.

decreases (refer to Equation (4)). When $\Delta K_{eff} \leq \Delta K_{th}$ (i.e. $\Delta K_{bonding} + \Delta K_{wedge} \geq \Delta K_I - \Delta K_{th}$), fatigue crack is fully arrested.

To look into the details of the retardation effect of the infiltrated epoxy based healing agent on fatigue crack growth, COD vs. fatigue cycles and load vs. displacement of the specimen healed at 0.112 MPa·m$^{1/2}$ are analyzed in the following as an example. It is seen that in the early stage when the healing agent has not been injected into the crack tip (refer to curve 3 in Fiure 4 and Figure 6), the corresponding load-displacement curves a and b in Figure 7 are linear with increasing compliance as the crack propagates. Following healing agent injection and cure, the load-displacement curve c in Figure 7 remains linear with reduced compliance due to the shorter (healed) crack length (refer to curve 3 in Figure 4). Accordingly, the crack cannot be fully opened at the maximum load as characterized by the deflected maximum COD vs. fatigue cycles (refer to curve 3 in Figure 6), and cannot be fully closed at the minimum load forming a terrace-like minimum COD vs. fatigue cycles (refer to curve 4 in Figure 6). The results imply that the consolidated healing agent has formed a wedge that has certain affinity for the cracked faces. As a result, the crack opening and closing under cyclic loading is significantly obstructed.

When the cyclic stress intensity exceeds the applied constant stress intensity during healing, the infiltrated epoxy healing agent bonds the crack surfaces together and starts to transfer tensile stress across the crack faces. The adhesive firstly fails on the tension part of the load cycle by cracking in the area that experiences the highest strain amplitude [11]. This is reflected by the turning point at about 71 700 cycles on the fatigue cycles dependences of crack length and maximum COD (refer to curve 3 in Figure 4 and Figure 6), from which the crack begins to advance fast. At this point, the crack advances about 1.4 mm. A stable pre-crack process seems to be formed. At about 115 500 cycles with fast crack advance, the load-displacement curve becomes clearly bimodal (curve j in Figure 7), representing the crack closure mechanism proposed by Elber [29]. The knee of the load-displacement curve corresponds to the open crack condition and the portion of the cyclic load experienced by the crack tip. Figure 7 further exhibits that the curve above the knee is increasingly compliant due to progressive cohesive failure of the cured healing agent (Figure 8). In contrast, the curve below the knee, which is related to the closed crack condition, retains a compliance corresponding to the epoxy wedge geometry. In the case that the cyclic stress intensity is lower than the applied constant stress intensity during healing, the infiltrated material acts as a wedge to transfer compressive stress between the crack faces. The extent to which the crack-tip

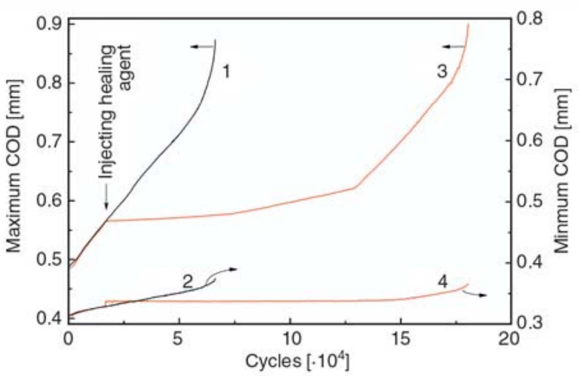

Figure 6. Maximum and minimum CODs vs. fatigue cycles of (1, 2) control fatigue specimens and (3, 4) fatigue specimens with manual injection of pre-mixed healing agent in static infiltration fashion. The applied constant stress intensity for holding crack open after the injection: 0.112 MPa·m$^{1/2}$. The steady-state healing time: 10 min. Testing conditions: K_{max} = 0.504 MPa·m$^{1/2}$, K_{min} = 0.050 MPa·m$^{1/2}$, ΔK_I = 0.454 MPa·m$^{1/2}$, R = 0.1.

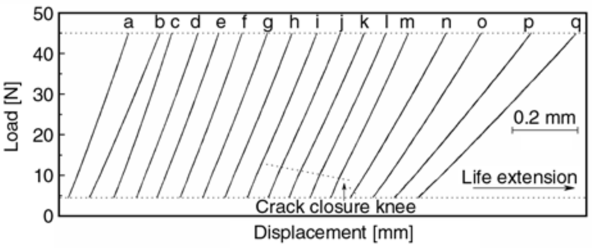

Figure 7. Load-displacement relationships measured during selected cycles of curve 3 in Figure 4. Number of the fatigue cycles and the time after the manual infiltration of pre-mixed healing agent: (a) 3000; (b) 9000; (c) 19 200, 10′; (d) 69 600; (e) 71 700, 185′; (f) 73 500; (g) 85 500; (h) 95 700; (i) 105 600; (j) 115 500, 331′; (k) 125 700; (l) 129 000, 376′; (m) 132 900; (n) 140 100; (o) 150 000, 446′; (p) 170 800; and (q) 181 800, 552′. The applied constant stress intensity for holding crack open after the injection: 0.112 MPa·m$^{1/2}$. The steady-state healing time: 10 min. Testing conditions: K_{max} = 0.504 MPa·m$^{1/2}$, K_{min} = 0.050 MPa·m$^{1/2}$, ΔK_I = 0.454 MPa·m$^{1/2}$, R = 0.1.

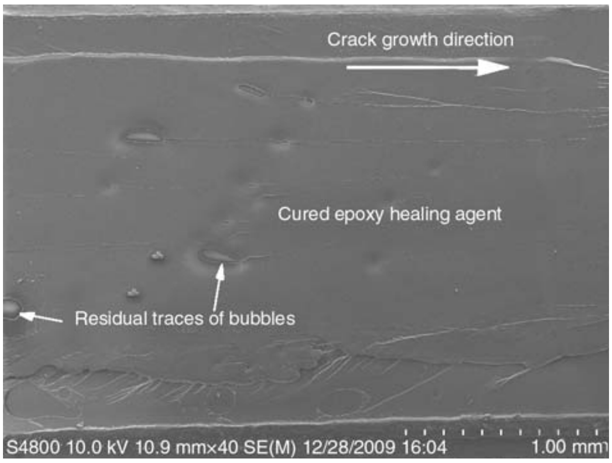

Figure 8. SEM micrograph of fatigue fracture specimen with manual injection of pre-mixed healing agent in static infiltration fashion. The applied constant stress intensity for holding crack open after the injection: 0.112 MPa·m$^{1/2}$. The steady-state healing time: 10 min. Testing conditions: K_{max} = 0.504 MPa·m$^{1/2}$, K_{min} = 0.050 MPa·m$^{1/2}$, ΔK_I = 0.454 MPa·m$^{1/2}$, R = 0.1.

could be unloaded is limited and hence higher ΔK_{eff} is maintained. Since cured epoxy material has very low deformation in compression and cannot be easily fragmented or otherwise dislodged from the crack, this is a potent crack retarding mechanism. Even when the adhesive wedge is damaged and the crack tip advances into the parent epoxy matrix beyond the region of the wedge, some benefit still remains from the wedging effect.

When fatigue cycles approach 129 000, the crack grows to the end of the cured epoxy wedge, and crack growth rate suddenly accelerates by 3.4-fold from $8.3\cdot10^{-5}$ to $3.7\cdot10^{-4}$ mm/cycle. Particularly large turning points appear on the curves of crack length and maximum COD vs. fatigue cycles (refer to curve 3 in Figure 4 and Figure 6). This is because the fracture toughness of the cured healing agent is higher than that of the epoxy matrix [20], and fatigue crack has to advance slowly within the wedge region. In the meantime, knee points are observed at decreasing loads (refer to curves j–n in Figure 7), indicating an increase in the effective cyclic stress intensity at the crack tip. As the crack grows past the wedge from the cured healing agent (refer to curve o in Figure 7), the crack growth rate increases with a rise in ΔK_{eff} approaching the rate before healing until failure of the specimen.

In previous studies, the adhesive infiltrants were generally allowed to be fully cured to form solid polymeric wedges under constant holding loads before resuming fatigue tests [4, 9–16]. Here the influence of the curing of the healing agent on fatigue crack growth is taken into consideration for evaluating the role of the wedge performance. For this purpose, as mentioned in the Experimental, 10 seconds after the pre-mixed healing agent was injected into the crack plane, the fatigue test was interrupted and the crack held open at a constant stress intensity of 0.504 MPa·m$^{1/2}$. Fatigue loading was reestablished after different steady-state healing times of 3′, 4′, 5′, 5′30″, 5′35″, 5′45″, 6′, 6′30″, 7′, 8′, 10′, 15′ and 30′ (the single and double quotation marks represent minute and second, respectively).

Figures 9 and 10 give the typical crack length vs. fatigue cycles curves and the relationship between healing efficiency and steady-state healing time, respectively. The results indicate that healing agent hardly takes effect within the steady-state healing time range of 3′–5′35″ (refer to curves 2 and 3 in Figure 9), so that the healing efficiency is only about 12–15% (Figure 10). When the steady-state healing time reaches 5′45″ and 6′, however, the healing efficiency is greatly increased to 302 and 1473%, respectively. The crack retardation behavior is similar to that of the specimen healed at 0.112 MPa·m$^{1/2}$ for 10 min (refer to curve 3 in Figure 4). In the case that the steady-state healing time is not less than 6′30″, crack can hardly advance

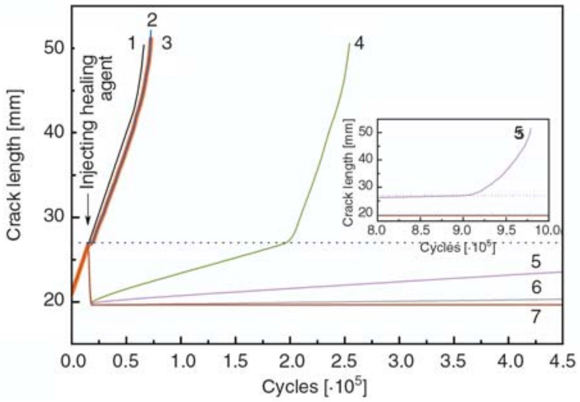

Figure 9. Crack length vs. fatigue cycles of (1) control fatigue specimen and (2–7) fatigue specimens with manual injection of pre-mixed healing agent in static infiltration fashion. The steady-state healing time: (2) 3′, (3) 5′35″, (4) 5′45″, (5) 6′, (6) 6′30″, and (7) 8′. The applied constant stress intensity for holding crack open after the injection: 0.504 MPa·m$^{1/2}$. Testing conditions: K_{max} = 0.504 MPa·m$^{1/2}$, K_{min} = 0.050 MPa·m$^{1/2}$, ΔK_I = 0.454 MPa·m$^{1/2}$, R = 0.1.

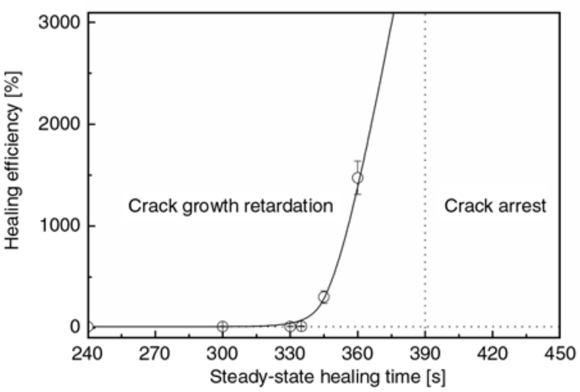

Figure 10. Healing efficiency of fatigue specimens with manual injection of pre-mixed healing agent in static infiltration fashion vs. the steady-state healing time (during which crack held open). The data are calculated using the results in Figure 9.

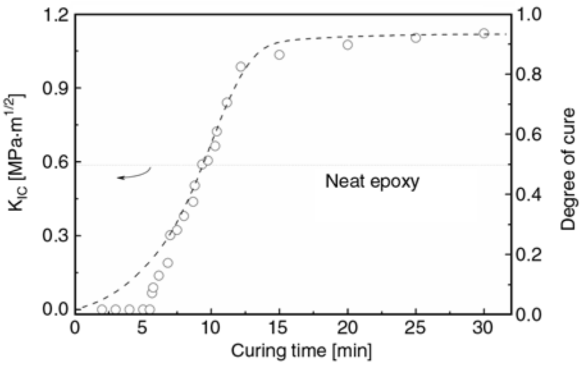

Figure 11. Curing time dependences of K_{IC} (circles) and degree of cure (dash line) of the healing agent. The horizontal dotted line represents K_{IC} of the epoxy matrix. K_{IC} values of the healing agent were obtained from monotonic fracture tests performed at prescribed times. The data of degree of cure were estimated from isothermal polymerization of the healing agent conducted in DSC at 25°C.

after more than 10^7 fatigue cycles and is considered to be fully arrested. Similarly, this time can be regarded as the critical threshold to distinguish fatigue crack growth retardation from crack arrest (Figure 10).

The above phenomena are closely related to the curing process of the epoxy based healing agent. During curing of the healing agent, the system transforms from low molecular liquid mixture into three dimensional cross-linked macromolecular networks. Molecular dynamics and macroscopic behavior of the material drastically change in the meantime [30]. Early study on curing kinetics demonstrated that the viscosity of the healing agent slowly increased in the beginning 5 min after mixing, and then rapidly increased until it gelled within about one minute [20, 21]. The gelation of the healing agent is essentially a rapid formation and increase process of hardness and adhesive strength (Figure 11). Although nearly no adhesion can be detected at a time less than 5.5 min, fracture toughness of the healing agent sharply increases within 5′40″ and 12′, and exceeds that of the epoxy matrix at about 9′. Obviously, the increase in K_{IC} keeps in step with the degree of cure of the healing agent, as shown by Brown *et al.* [5]. In this context, development of fatigue crack might become rather difficult when the steady-state healing time is longer than 9′. The deduction is confirmed by the fact that very few tearing marks appear at the initial phase of the

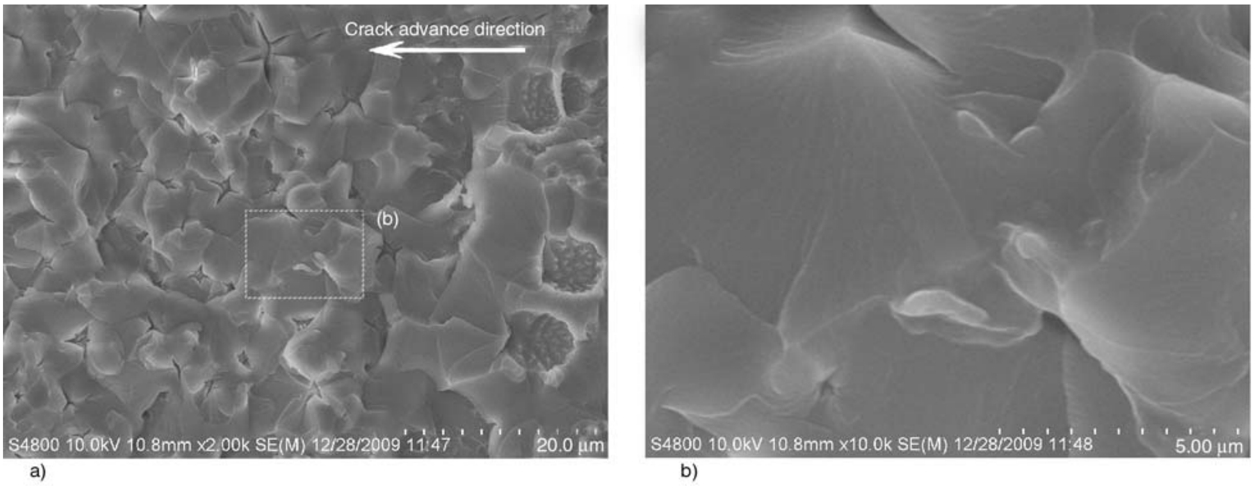

a)

b)

Figure 12. SEM micrographs of the fractured surface of a TDCB specimen with manual injection of pre-mixed healing agent for determination of K_{IC} of the cured healing agent (see the Experimental for more details). The healing agent was allowed to be cured for 9′20″ and then the specimen was tested to falure within 5 sec at a rate of displacement of 3 mm/min.

fatigue crack (figure omitted). Obvious tearing traces are found on the fast fracture plane when the healing agent is in the rubbery state (Figure 12). Accordingly, evident retardation effect is obtained for the steady-state healing time from 5′45″ to 6′.

3.3. Effect of applied range of cyclic stress intensity revealed by dynamic infiltration tests

The works by other researchers have shown that the *in-situ* retardation and arrest of fatigue crack are closely related to the applied range of cyclic stress intensity, ΔK_I [5–8]. To check whether this rule is also valid for the current healing system, the fatigue experiments associated with dynamic infiltration were conducted at different ΔK_I values by changing the maximum cyclic stress intensity $K_{\max}$ between 0.336 and 0.560 MPa·m$^{1/2}$ at constant stress ratio of $R = 0.1$, and by changing the stress ratio R from 0.05 to 0.6 at constant $K_{\max} = 0.504$ MPa·m$^{1/2}$.

As shown in Figures 13–15, fatigue crack is retarded by the infiltrated healing agent following the injection. The lower the maximum cyclic stress intensity (or the higher stress ratio), the more evident the retardation effect and the higher healing efficiency. Especially when the $K_{\max}$ is not more than 0.420 MPa·m$^{1/2}$ or the R value is not less than 0.25, crack can hardly advance for more than 10^7 cycles with the gelation and solidification of the healing agent, and hence is considered to be fully arrested. During this process, the mechanisms of polymeric wedge crack-tip shielding and adhesive bonding must play the key role. In fact, reducing $K_{\max}$ or increasing R is equivalent to decreasing ΔK_I, so that ΔK_{eff} is decreased, offering improved retardation effect.

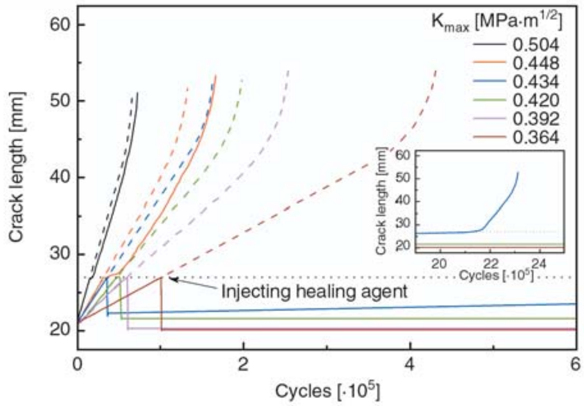

Figure 13. Crack length vs. fatigue cycles of control fatigue specimens (dash lines) and fatigue specimens with manual injection of pre-mixed healing agent in dynamic infiltration fashion (solid lines). Testing conditions: $K_{\max} = 0.504$, 0.448, 0.434, 0.420, 0.392 and 0.364 MPa·m$^{1/2}$, $R = 0.1$.

To have more information about the healing mechanism involved in the dynamic infiltration tests, the processes of crack growth retardation and crack arrest measured at two typical $K_{\max}$ values (i.e. 0.504 and 0.420 MPa·m$^{1/2}$) are analyzed in the following.

Immediately after the injection, the fluidic healing agent rapidly flows throughout the cracked plane and penetrates into the crack tip under cycling load. The rate of crack growth decreases to a lower value. Similar to the cases discussed in the last subsections, full opening and closing of crack at the maximum and minimum loads are hindered accord-

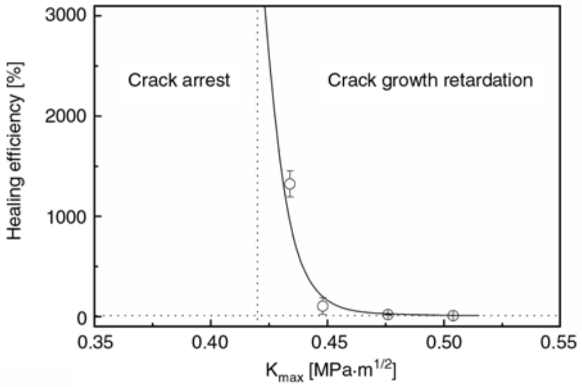

Figure 14. Healing efficiency of fatigue specimens with manual injection of pre-mixed healing agent in dynamic infiltration fashion vs. maximum cyclic stress intensity. The data are calculated using the results in Figure 13.

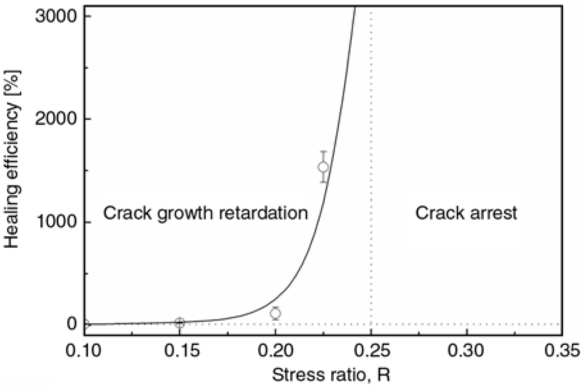

Figure 15. Healing efficiency of fatigue specimens with manual injection of pre-mixed healing agent in dynamic infiltration fashion vs. cyclic stress intensity ratio. The data are calculated using the results in Figure 13.

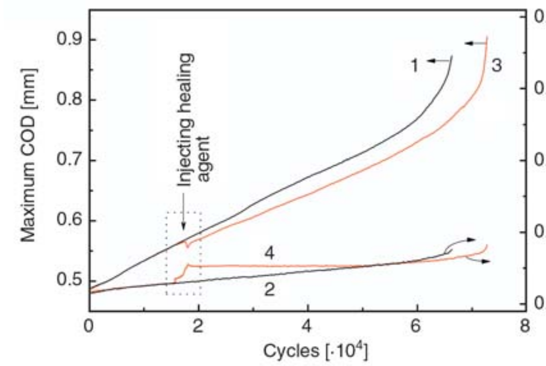

Figure 16. Maximum and minimum CODs vs. fatigue cycles of (1, 2) control fatigue specimens and (3, 4) fatigue specimens with manual injection of pre-mixed healing agent in dynamic infiltration fashion. Testing conditions: $K_{\max} = 0.504$ MPa·m$^{1/2}$, $K_{\min} = 0.050$ MPa·m$^{1/2}$, $\Delta K_I = 0.454$ MPa·m$^{1/2}$, $R = 0.1$.

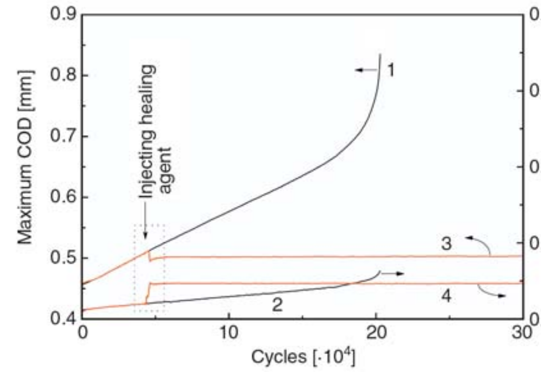

Figure 17. Maximum and minimum CODs vs. fatigue cycles of (1, 2) control fatigue specimens and (3, 4) fatigue specimens with manual injection of pre-mixed healing agent in dynamic infiltration fashion. Testing conditions: $K_{\max} = 0.420$ MPa·m$^{1/2}$, $K_{\min} = 0.042$ MPa·m$^{1/2}$, $\Delta K_I = 0.378$ MPa·m$^{1/2}$, $R = 0.1$.

ingly, so that fluctuations appear on the fatigue cycles dependence of the maximum and minimum CODs (Figures 16–19). Hysteresis loops are also observed on the load-displacement curves (refer curve d in Figure 20 and Figure 21). On the basis of the study in the sub-section 3.1, it is known that hydrodynamic pressure crack-tip shielding mechanism should be the main contributor to the crack retardation within the beginning ~5.5 min. Combining with the results of static infiltration tests with steady-state healing time of 3′–5′35″ (refer to curves 2 and 3 in Figure 9), we can conclude that the stress status of crack has no influence on crack growth retardation basically before the healing agent gels.

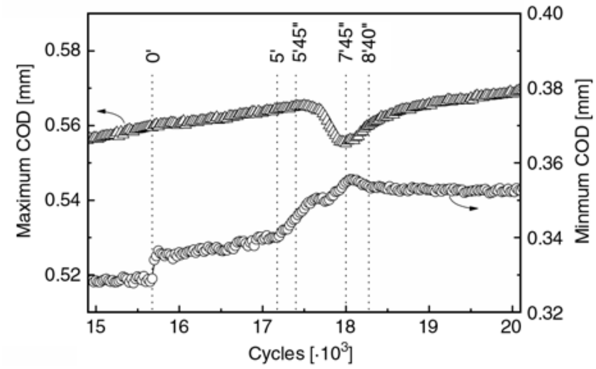

Figure 18. Maximum and minimum CODs vs. fatigue cycles of fatigue specimens with manual injection of pre-mixed healing agent in dynamic infiltration fashion (partial magnification of curves 3 and 4 within the dotted frame in Figure 16). 0′ means the time when the epoxy prepolymer is injected. Testing conditions: $K_{\max} = 0.504$ MPa·m$^{1/2}$, $K_{\min} = 0.050$ MPa·m$^{1/2}$, $\Delta K_I = 0.454$ MPa·m$^{1/2}$, $R = 0.1$.

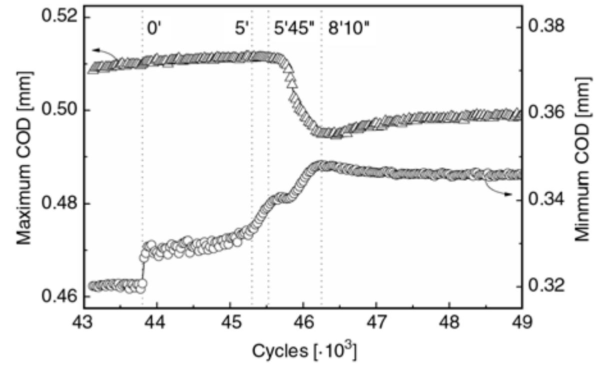

Figure 19. Maximum and minimum CODs vs. fatigue cycles of fatigue specimens with manual injection of pre-mixed healing agent in dynamic infiltration fashion (partial magnification of curves 3 and 4 within the dotted frame in Figure 17). 0′ means the time when the epoxy prepolymer is injected. Testing conditions: $K_{\max} = 0.420$ MPa·m$^{1/2}$, $K_{\min} = 0.042$ MPa·m$^{1/2}$, $\Delta K_I = 0.378$ MPa·m$^{1/2}$, $R = 0.1$.

Along with the abrupt increase in viscosity and gelation as of ~5.5 min (Figure 11), the healing agent rapidly changes from liquid to rubbery state. Its bonding capability forms and begins to take effect. The maximum and minimum CODs are further constrained with a regression of the crack tip (Figures 18 and 19). They reach the extreme values at 7′45″ for $K_{\max} = 0.504$ MPa·m$^{1/2}$ and at 8′10″ for $K_{\max} = 0.420$ MPa·m$^{1/2}$, respectively. Afterwards, the increase in the maximum COD for $K_{\max} = 0.504$ MPa·m$^{1/2}$ with fatigue cycles becomes steady, meaning that the closed crack can be quickly opened (refer to curve 3 in Figure 16, and Figure 18). With respect to the minimum COD for $K_{max} = 0.504$ MPa·m$^{1/2}$, it quickly declines to a plateau (refer to curve 4 in Figure 16 and Figure 18) owing to the formation of a stable wedge. In the case that $K_{max} = 0.420$ MPa·m$^{1/2}$, however, the results are not completely the same. The maximum COD slightly increases and then becomes nearly invariable with fatigue cycles (refer to curve 3 in Figure 17 and Figure 19). This corresponds to the fact that the closed crack advances for a very short distance before it is fully arrested. In contrast, the variation in the minimum COD resembles that at $K_{max} = 0.504$ MPa·m$^{1/2}$ as characterized by the appearance of a plateau (refer to curve 4 in Figure 17 and Figure 19) because of the newly established cured epoxy wedge.

It is worth noting that in the course of hardening of the healing agent, the opening degree of the hysteresis loops gradually increases and the maximum open position constantly moves upward (refer to curves f–j in Figure 20, and curves f–n in Figure 21). The former reaches the maximum at about 8′ for $K_{max} = 0.504$ MPa·m$^{1/2}$ and at 7′20″ for $K_{max} = 0.420$ MPa·m$^{1/2}$, as shown in curve k in Figure 20 and Figure 21, respectively. Then, it gradually decreases until disappearance at about 11′ (refer to curves k–r in Figure 20 and Figure 21). Clearly, within the time range from 5.5′ to 11′, the visco-elastic damping provided by the healing agent increases and then decreases with the gradual increase in crosslinking of the healing agent. The increase in the maximum open position is attributed to the fact that trigger of the hysteresis in terms of lower tension or pressure becomes increasingly difficult. When the curing of the healing agent is almost completed, the hysteresis loop disappears (refer to curve r in Figure 20 and Figure 21). Especially for $K_{max} = 0.504$ MPa·m$^{1/2}$, the knee on the load-displacement curves gradually forms from about 8′10″ to 11′ (refer to curves l–r in Figure 20) as a result of crack closure [15]. Nevertheless, when $K_{max} = 0.420$ MPa·m$^{1/2}$, the aforesaid knee doesn't appear on the load-displacement curves even after disappearance of the hysteresis loop (Figure 21). The slopes of the load-displacement curves (related to the compliance) hardly increase after $6\cdot10^8$ cycles (refer to curve t in Figure 21), which represents that the crack is fully arrested.

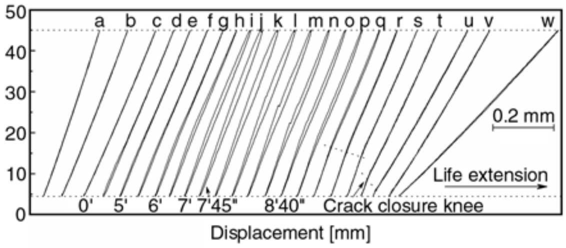

Figure 20. Load-displacement relationships measured during selected cycles in Figures 16 and 18. Number of the fatigue cycles and the time after the manual infiltration of pre-mixed healing agent: (a) 17 400; (b) 23 400; (c) 15 675, 0′; (d) 15 825, 30″; (e) 17 175, 5′; (f) 17 325, 5′30″; (g) 17 475, 6′; (h) 17 625, 6′30″; (i) 17 775, 7′; (j) 18 000, 7′45″; (k) 18 075, 8′; (l) 18 125, 8′10″; (m) 18 175, 8′20″; (n) 18 225, 8′30″; (o) 18 275, 8′40″; (p) 18 375, 9′; (q) 18 675, 10′; (r) 18 975, 11′; (s) 22 400; (t) 30 000; (u) 45 000; (v) 49 950; and (w) 72 750. 0′ means the time when the pre-mixed healing agent is injected. Testing conditions: $K_{max} = 0.504$ MPa·m$^{1/2}$, $K_{min} = 0.050$ MPa·m$^{1/2}$, $\Delta K_I = 0.454$ MPa·m$^{1/2}$, $R = 0.1$.

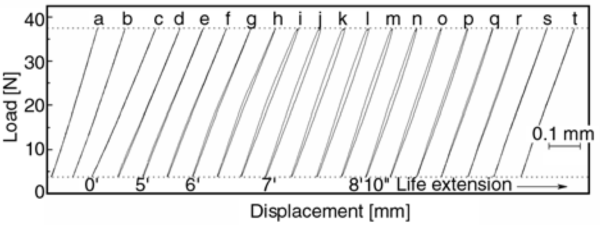

Figure 21. Load-displacement relationships measured during selected cycles in Figures 17 and 19. Number of the fatigue cycles and the time after the manual infiltration of pre-mixed healing agent: (a) 3000; (b) 30 000; (c) 43 800, 0′; (d) 43 950, 30″; (e) 45 300, 5′; (f) 45 450, 5′30″; (g) 45 600, 6′; (h) 45 725, 6′25″; (i) 45 800, 6′40″; (j) 45 900, 7′; (k) 46 000, 7′20″; (l) 46 100, 7′40″; (m) 46 200, 8′; (n) 46 250, 8′10″; (o) 46 350, 8′30″; (p) 46 500, 9′; (q) 46 800, 10′; (r) 47 100, 11′; (s) 53 100; and (t) $6\cdot10^8$. 0′ means the time when the pre-mixed healing agent is injected. Testing conditions: $K_{max} = 0.420$ MPa·m$^{1/2}$, $K_{min} = 0.042$ MPa·m$^{1/2}$, $\Delta K_I = 0.378$ MPa·m$^{1/2}$, $R = 0.1$.

On the other hand, ear-piercing sound of 'dada' was perceived as of about 8′40″ during the process of crack growth for $K_{max} = 0.504$ MPa·m$^{1/2}$, but never for $K_{max} = 0.420$ MPa·m$^{1/2}$. It should come from (i) tearing of the curing adhesive in the process of crack opening and advancing, and (ii) impact of torn surfaces in the process of crack closing after growth of fatigue crack through cured adhesive to the original crack tip position. The phenomenon proves the events of crack advancing or crack growth retardation from another angle.

Morphology of the fatigue fracture surfaces can further explain the crack healing process (Figures 22 and 23). The cured healing agent is symmetrically distributed on the two opposite planes of fatigue crack (Figures 22a–d). This result indicates

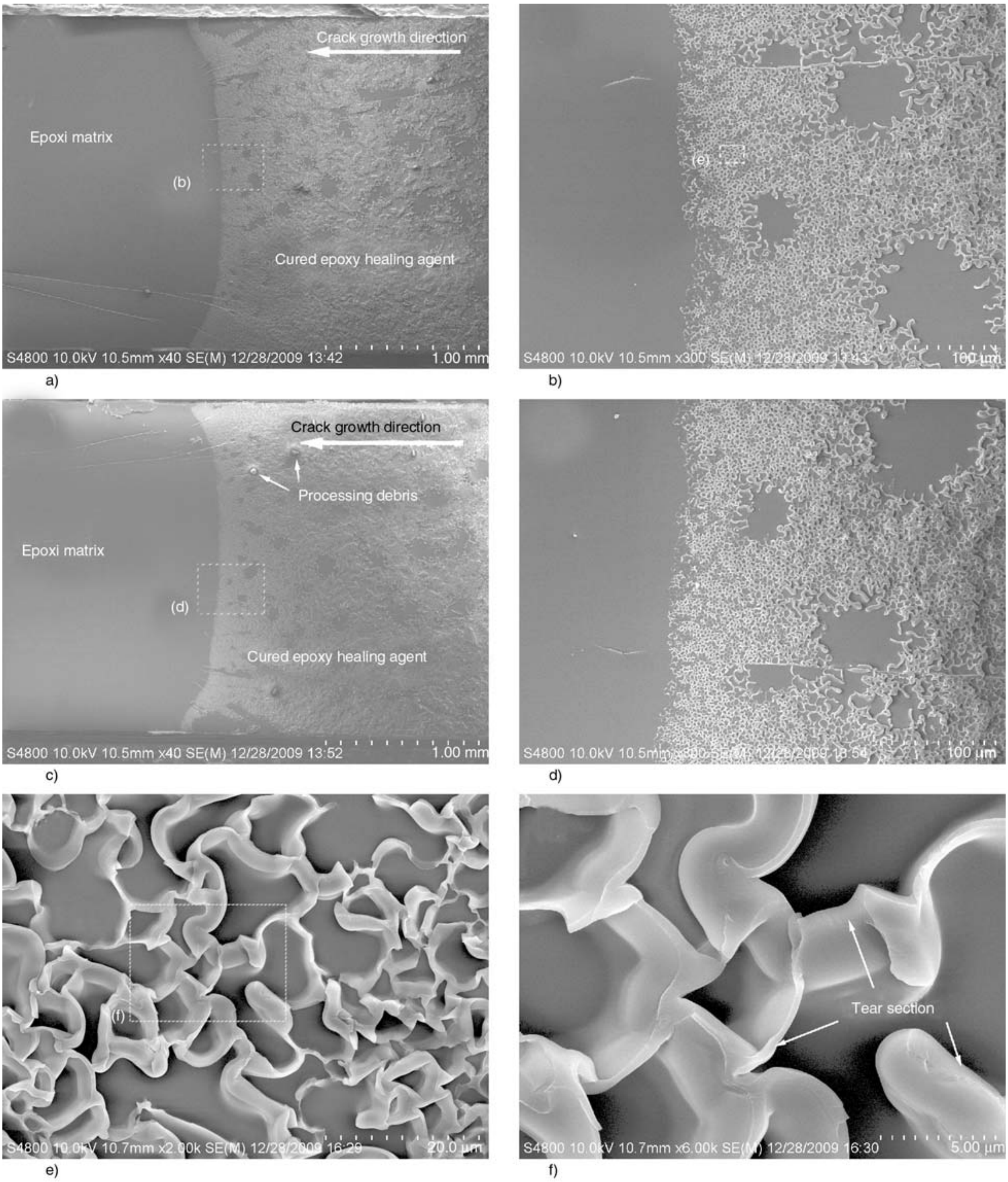

Figure 22. SEM micrographs of fatigue fracture surfaces of the specimen with manual injection of pre-mixed healing agent in dynamic infiltration fashion. (a) Fatigue crack plane; (b) partial magnification of (a); (c) the opposite part of (a); (d) the opposite part of (b) taken from (c); (e) partial magnification of (b); (f) partial magnification of (e). Testing conditions: $K_{\max} = 0.504$ MPa·m$^{1/2}$, $K_{\min} = 0.050$ MPa·m$^{1/2}$, $\Delta K_I = 0.454$ MPa·m$^{1/2}$, $R = 0.1$.

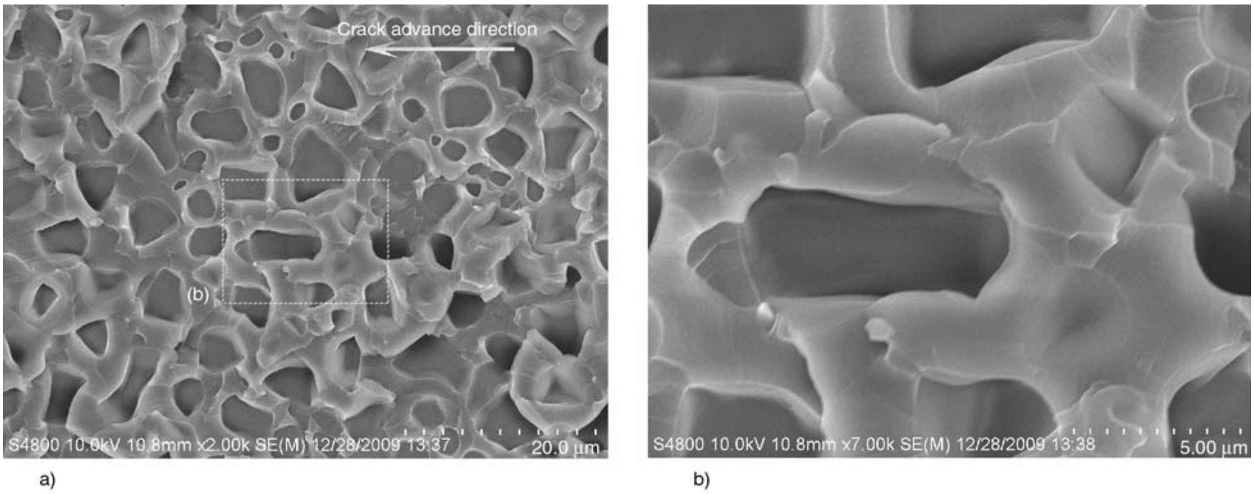

Figure 23. SEM micrographs of fatigue fracture surface of the specimen with manual injection of pre-mixed healing agent in dynamic infiltration fashion. (a) Fatigue crack plane; (b) partial magnification of (a). Crack can hardly advance for $6\cdot10^8$ cycles and hence is fully arrested. The specimen was fractured at static load using a rate of displacement of 3 mm/min without precrack. Fatigue testing conditions: $K_{\max} = 0.420$ MPa·m$^{1/2}$, $K_{\min} = 0.042$ MPa·m$^{1/2}$, $\Delta K_I = 0.378$ MPa·m$^{1/2}$, $R = 0.1$.

that the crack propagates through the membrane formed by the cured healing agent, and cohesive failure rather than interfacial debonding occurs in the case of crack retardation. Obvious tear traces and good bonding effect of the healing agent are found on the fracture plane (Figures 22e and f). Besides, blank areas without the healing agent are also observed on the fracture plane (e.g. Figures 22b and d). They originate from the air bubbles that were introduced when the liquid healing agent was subjected to the repeated extrusion under cycling loading.

When the fatigue crack is arrested at $K_{\max} =$ 0.420 MPa·m$^{1/2}$, the specimen is eventually fractured at static load using a displacement rate of 3 mm/min without precrack. The maximum fracture load reaches 121 N, which is much higher than that of the epoxy matrix (~52 N). The cohesive failure of the cured healing agent is characterized by wider tear tapes and larger bonding area on the fracture plane (Figures 23). It implies that stronger adhesion effect is obtained at lower $K_{\max}$, which favors to arrest crack.

4. Conclusions

The epoxy component of the healing agent proved to act as a viscous fluid, effectively retarding fatigue crack growth in epoxy material by hydrodynamic pressure crack-tip shielding effect. Accordingly, the latter's fatigue life was extended by about 2.5 times.

Artificial crack closure was achieved during static infiltration tests by injecting the pre-mixed healing agent into the crack plane forming a polymer wedge at the crack tip. As a result, crack growth retardation and even permanent crack arrest were observed. Both crack-face wedging and adhesion contributed to the retardation, but the adhesive component ceased after the crack grew through the wedge to the original crack tip position. The higher the constant stress intensity applied for holding crack open after the manual infiltration, the thicker the polymerized wedge and the better the retardation effect. When the former was not less than 0.392 MPa·m$^{1/2}$, crack was fully arrested. Similarly, in the case that the steady-state healing time approached about 6 min after the infiltration, adhesive strength and hardness of the gelled healing agent were well developed and ΔK_{eff} was effectively reduced. Cohesive failure of the wedge occurred under cyclic loading. Further extending the steady-state healing time to 6′30″, crack arrest was observed.

As for the dynamic infiltration tests, the applied stress intensity range was found to be the most influential parameter. When the pre-mixed healing agent was infiltrated into the crack plane, hydrodynamic pressure shielding mechanism firstly provided resistance to crack growth. With the rapid increase in viscosity of the healing agent until gelation, shielding effect resulting from the wedge and adhesive bonding gradually played the leading role. The lower the maximum cyclic stress intensity or the higher the stress ratio, the more prominent the retardation effect. The maximum cyclic stress intensity of about 0.420 MPa·m$^{1/2}$ and the stress ratio of about 0.25 became the watersheds between fatigue crack growth retardation and crack arrest, respectively.

The present work is the first attempt of ours towards healing fatigue crack using epoxy/mercaptan/tertiary amine system. The capability of the healing agent for retarding or arresting fatigue crack growth revealed hereinbefore demonstrates its potential for *in-situ* self-healing of fatigue damage. More importantly, the microscopic information helps to understand the healing mechanisms of self-healing composites with dual microencapsulated healing agent subjected to cyclic loading, and to optimize the healant formulation accordingly. In authentic self-healing composites, the appearance of the healant loaded capsules would change the intrinsic properties of the composites and deviate the propagation path of fatigue crack, which disfavors the analysis of the true healing mechanism involved.

Successful retardation and/or arrest of fatigue cracks have been observed in *in-situ* self-healing epoxy composites containing dual encapsulated healant, i.e. two types of microcapsules that respectively include epoxy prepolymer and mercaptan/tertiary amine hardener. The results and analyses will be reported in another article of the authors.

Acknowledgements

The authors are grateful to the support of the Natural Science Foundation of China (Grants: U0634001, 20874117, 50573093 and 50903095) and China Postdoctoral Science Foundation.

References

[1] Murphy E. B., Wudl F.: The world of smart healable materials. Progress in Polymer Science, **35**, 223–251 (2010).
DOI: 10.1016/j.progpolymsci.2009.10.006

[2] Yuan Y. C., Yin T., Rong M. Z., Zhang M. Q.: Self healing in polymers and polymer composites. Concepts, realization and outlook: A review. Express Polymer Letters, **2**, 238–250 (2008).
DOI: 10.3144/expresspolymlett.2008.29

[3] Caruso M. M., Davis D. A., Shen Q., Odom S. A., Sottos N. R., White S. R., Moore J. S.: Mechanically-induced chemical changes in polymeric materials. Chemical Reviews, **109**, 5755–5798 (2009).
DOI: 10.1021/cr9001353

[4] Brown E. N., White S. R., Sottos N. R.: Retardation and repair of fatigue cracks in a microcapsule toughened epoxy composite – Part I: Manual infiltration. Composites Science and Technology, **65**, 2466–2473 (2005).
DOI: 10.1016/j.compscitech.2005.04.020

[5] Brown E. N., White S. R., Sottos N. R.: Retardation and repair of fatigue cracks in a microcapsule toughened epoxy composite – Part II: In situ self-healing. Composites Science and Technology, **65**, 2474–2480 (2005).
DOI: 10.1016/j.compscitech.2005.04.053

[6] Jones A. S., Rule J. D., Moore J. S., Sottos N. R., White S. R.: Life extension of self-healing polymers with rapidly growing fatigue cracks. Journal of the Royal Society Interface, **4**, 395–403 (2007).
DOI: 10.1098/rsif.2006.0199

[7] Maiti S., Geubelle P. H.: Cohesive modeling of fatigue crack retardation in polymers: Crack closure effect. Engineering Fracture Mechanics, **73**, 22–41 (2006).
DOI: 10.1016/j.engfracmech.2005.07.005

[8] Maiti S., Shankar C., Geubelle P. H., Kieffer J.: Continuum and molecular-level modeling of fatigue crack retardation in self-healing polymers. Journal of Engineering Materials and Technology-Transactions of the ASME, **128**, 595–602 (2006).
DOI: 10.1115/1.2345452

[9] James M. N., Smith G. C.: Surface microcrack closure in fatigue: A comparison of compliance and crack sectioning data. International Journal of Fracture, **22**, R69–R75 (1983).
DOI: 10.1007/BF00942729

[10] Shin C. S., Wang C. M., Song P. S.: Fatigue damage repair: A comparison of some possible methods. International Journal of Fatigue, **18**, 535–546 (1996).
DOI: 10.1016/S0142-1123(96)00029-1

[11] Sharp P. K., Clayton J. Q., Clark G.: Retardation and repair of fatigue cracks by adhesive infiltration. Fatigue and Fracture of Engineering Materials and Structures, **20**, 605–614 (1997).
DOI: 10.1111/j.1460-2695.1997.tb00292.x

[12] Song P. S., Hwang S., Shin C. S.: Effect of artificial closure materials on crack growth retardation. Engineering Fracture Mechanics, **60**, 47–58 (1998).
DOI: 10.1016/S0013-7944(97)00180-X

[13] Shin C. S., Cai C. Q.: Surface fatigue crack growth suppression in cylindrical rods by artificial infiltration. International Journal of Fatigue, **30**, 560–567 (2008).
DOI: 10.1016/j.ijfatigue.2007.03.005

[14] ur-Rehman A., Thomason P. F.: The effect of artificial fatigue-crack closure on fatigue-crack growth. Fatigue and Fracture of Engineering Materials and Structures, **16**, 1081–1090 (1993).
DOI: 10.1111/j.1460-2695.1993.tb00079.x

[15] Shin C. S., Chen Z. Z.: Fatigue life extension by electroless nickel infiltration plating. International Journal of Fatigue, **23**, 777–788 (2001).
DOI: 10.1016/S0142-1123(01)00038-X

[16] Wang Y., Zho M., Feng D.: A study of retarding fatigue crack growth using an artificial wedge. Fatigue and Fracture of Engineering Materials and Structures, **16**, 363–376 (1993).
DOI: 10.1111/j.1460-2695.1993.tb00093.x

[17] White S. R., Sottos N. R., Geubelle P. H., Moore J. S., Kessler M. R., Sriram S. R., Brown E. N., Viswanathan S.: Autonomic healing of polymer composites. Nature, **409**, 794–797 (2001).
DOI: 10.1038/35057232

[18] Yuan Y. C., Rong M. Z., Zhang M. Q.: Preparation and characterization of microencapsulated polythiol. Polymer, **49**, 2531–2541 (2008).
DOI: 10.1016/j.polymer.2008.03.044

[19] Yuan Y. C., Rong M. Z., Zhang M. Q.: Preparation and characterization of poly (melamine-formaldehyde) walled microcapsules containing epoxy. Acta Polymerica Sinica, **5**, 472–480 (2008).

[20] Yuan Y. C., Rong M. Z., Zhang M. Q., Chen J., Yang G. C., Li X. M.: Self-healing polymeric materials using epoxy/mercaptan as the healant. Macromolecules, **41**, 5197–5202 (2008).
DOI: 10.1021/ma800028d

[21] Yuan Y. C., Rong M. Z., Zhang M. Q., Yang G. C.: Study of factors related to performance improvement of self-healing epoxy based on dual encapsulated healant. Polymer, **50**, 5771–5781 (2009).
DOI: 10.1016/j.polymer.2009.10.019

[22] Brown E. N., Sottos N. R., White S. R.: Fracture testing of a self-healing polymer composite. Experimental Mechanics, **42**, 372–379 (2002).
DOI: 10.1007/BF02412141

[23] Brown E. N., White S. R., Sottos N. R.: Fatigue crack propagation in microcapsule-toughened epoxy. Journal of Materials Science, **41**, 6266–6273 (2006).
DOI: 10.1007/s10853-006-0512-y

[24] Tzou J-L., Hsueh C. H., Evans A. G., Ritchie R. O.: Fatigue crack propagation in oil environments – II. A model for crack closure induced by viscous fluids. Acta Metallurgica, **33**, 117–127 (1985).
DOI: 10.1016/0001-6160(85)90225-1

[25] Davis F. H., Ellison E. G.: Hydrodynamic pressure effects of viscous fluid flow in a fatigue crack. Fatigue and Fracture of Engineering Materials and Structures, **12**, 527–542 (1989).
DOI: 10.1111/j.1460-2695.1989.tb00561.x

[26] Yi K. S., Cox B. N., Dauskardt R. H.: Fatigue crack-growth behavior of materials in viscous fluid environments. Journal of the Mechanics and Physics of Solids, **47**, 1843–1871 (1999).
DOI: 10.1016/S0022-5096(99)00002-2

[27] Endo K., Okada T., Komai K., Kiyota M.: Fatigue crack propagation of steel in oil. Bulletin of the Japan Society of Mechanical Engineers, **15**, 1316–1323 (1972).

[28] Paris P. C., Gomez M. P., Anderson W. E.: A rational analytic theory of fatigue. The Trend in Engineering, **13**, 9–14 (1961).

[29] Elber W.: Fatigue crack closure under cyclic tension. Engineering Fracture Mechanics, **2**, 37–45 (1970).
DOI: 10.1016/0013-7944(70)90028-7

[30] Petrie E. M.: Epoxy adhesive formulations. McGraw-Hill, New York (2006).

eXPRESS Polymer Letters Vol.4, No.10 (2010) 659–668
Available online at www.expresspolymlett.com
DOI: 10.3144/expresspolymlett.2010.80

Crystalline structure of annealed polylactic acid and its relation to processing

*T. Tábi[1], I. E. Sajó[2], F. Szabó[1], A. S. Luyt[3], J. G. Kovács[1]**

[1]Department of Polymer Engineering, Budapest University of Technology and Economics, Műegyetem rkp. 3., H-1111 Budapest, Hungary
[2]Hungarian Academy of Sciences, Chemical Research Center, Department of X-ray Diffraction, Pusztaszeri út 57–59, H-1025 Budapest, Hungary
[3]Department of Chemistry, University of the Free State (Qwaqwa Campus), Private Bag X13, Phuthaditjhaba, 9866, South Africa

Received 8 April 2010; accepted in revised form 27 June 2010

Abstract. This paper focuses on the crystalline structure of injection moulding grade poly(lactic acid) (PLA) and the effect of crystalline structure on the processing. The research is induced by the significant differences in crystallinity of the pure PLA resin, and the injection moulded product, and thus the reprocessing of PLA products. 2 mm thick PLA sheets were injection moulded and re-crystallized in a conventional oven at 60–140°C, for 10–60 minutes to achieve various crystalline contents. The properties of these sheets were investigated by dynamic mechanical analysis (DMA), differential scanning calorimetry (DSC), and wide angle X-ray diffraction (WAXD). In a processing plant the rejected parts are recycled and reused as raw material for further cycles, accordingly the various crystalline content PLA products were reprocessed as a resin, to investigate the processing itself. When PLA products are reprocessed, due to the adherent feature of amorphous PLA processing difficulties may occur. This adherent effect of the amorphous PLA was investigated and characterized.

Keywords: *biodegradable polymers, polylactic acid, annealing, crystallinity, recycling*

1. Introduction

In the last few decades interest has turned from the conventional petrol based polymers to biodegradable polymers. This attention is due to the fact that some of these biodegradable polymers can be bio-based while the conventional plastics are petrol based. Furthermore, the degradation feature of these biodegradable polymers also carries great advantage in contrast with the low recycled ratio of the mass plastics like polyethylene (PE) or polypropylene (PP). Besides these advantages the products made from biodegradable polymers can be fit in the natural recycling processes [1–4].

Among the bio-based products, most of the research has been made on starch. Starch is a renewable feedstock, which can be found all over the world in significant amounts in agricultural plants like maize, wheat, potato, rice, pea, etc. Based on the experience in the food processing industry, thermoplastic starch (TPS) was developed by disrupting starch granules with the help of heat and shearing action [5–8]. TPS can be further processed with slightly modified equipment like ordinary plastics, however, its drawbacks like low mechanical properties, quick ageing feature, and low water resistant properties made it only adequate for blends mostly in combination with another biodegradable polymer [9–12]. Nowadays the TPS/PCL (polycaprolactone) blend is mostly used for disposable shopping bags.

---

*Corresponding author, e-mail: kovacs@pt.bme.hu

Another way of utilizing starch in the field of biopolymers is its fermentation with other biomass products like sugar. In the late 1990's a breakthrough came in the fermentation process of starch and sugar, thus lactic acid was made as a raw material for poly(lactic acid) (PLA). The technology has a reasonable price compared to the synthesis of petrol based plastics, which made PLA to reach wide industrial interest. PLA proved not only to be a fully bio-based and compostable biodegradable polymer, but a biodegradable polymer with excellent mechanical properties, easy processability and reasonable price. Shopping bags, mulch films, cutleries, office utensils, flower pots, yoghurt cans, and toothbrush handles can be made from PLA, but in the near future it can enter into medical applications or it can serve as the material for engineering products [13–15].

Based on the stereoregularity (L and D) of lactic acid, L, D and D-L type lactides can be used in PLA production. Semi-crystalline PLLA (poly-L-lactic acid) or amorphous PDLA (poly-D-lactic acid) can be produced by a ring opening polymerisation of these lactides. For a commercial PLA a blend of a higher amount of L-lactide and a lower amount of D-lactide is used. The ratio of the two lactides influences the mechanical properties, crystallinity and even the degradation characteristics. When semi-crystalline PLA is processed, its crystallinity changes depend on the cooling rate. Typically in injection moulding, due to the high cooling rates, totally amorphous PLA products are produced. In the differential scanning calorimetry (DSC) curve of this amorphous PLA an exotherm can be found, related to the cold crystallization above T_g, and an endotherm, related to melting. When PLA is recrystallized prior to measurement, the exotherm in the DSC curve is not present [16, 17].

During the crystallization of PLLA at high temperatures (>130–140°C) it is found that the disordered α' crystalline form, which can be produced by annealing at lower temperatures, transforms into the ordered α form. The differences between the α' and α forms can be observed by wide angle X-ray diffraction (WAXD) spectrometry and DSC analysis [18]. In the WAXD analysis, more intense and new peaks can be found, while in the DSC curves two endothermic peaks appear related to the melting of the α'- and α phases. The peak at the lower temperature is related to the melting of the α' form and its recrystallization into the α form, while the second peak corresponds to the melting of the α form. The two processes, the melting of the α' form and the recrystallization into the α form can be considered as the α'–α phase transition. For lower molecular weight PLA, the α'–α phase transition occurs at lower temperatures compared to higher molecular weight PLA [18, 19]. Crystallinity also influences the dynamic mechanical analysis (DMA) properties. As it can be seen in the DSC curves, the recrystallization occurs above T_g and increases the storage modulus [20].

Recrystallized PLA products also carry a huge advantage compared to amorphous products. This advantage is manifested in the much higher heat deflection temperature (HDT); while amorphous PLA products have an HDT of 50°C, semi-crystalline PLA products have an HDT of 130°C. Although PLA can be recrystallized after processing into a product, the products shrink and significant warpage occurs during recrystallization due to the increasing crystallinity. Distortion-free semi-crystallized PLA products can only be made during the process using nucleating agents. Talc was found to be an effective nucleating agent, which was observed during DMA analyses [21].

The injection moulding grade PLA with a D-Lactide content of 4% can be purchased in semi-crystalline form, but when it is processed into a product, or mixed with natural fillers or fibres using melt mixing techniques like extrusion, this PLA becomes amorphous even at very low cooling rates (without the use of nucleating agents). Thus, if it is to be further processed like in the case of PLA based composite pellets or if it is to be reused like in an industrial processing plant where the rejected parts are to be recycled, then because of the change in crystallinity, a totally different material is going to be processed. The changes in crystallinity during processing and its effect on the re-processing have been investigated with injection moulding; furthermore, the properties of various crystalline content injection moulding grade PLA resins were analysed, and the processing difficulties due to crystalline structure were explained.

2. Materials, processing and experimental

Semi crystalline PLA injection moulding grade resin (type Ingeo 3051D from NatureWorks Ltd., USA, with a D-lactide content of 4%) was used for the measurements. It was dried at 85°C for 6 hours before injection moulding to prevent any degradation due to hydrolysis. 2 mm thick, 80 mm by 80 mm specimens were injection moulded with an Arburg Allrounder 320C 600-250 injection moulding machine equipped with a ø35 mm screw. The injection pressure was 850 bars, while the applied holding pressure was 600 bars. The temperature profile used was 165-175-180-185-190°C from the hopper to the nozzle.

In order to produce quality PLA products some precautions were taken. To form a homogenous melt, at least 30 bar of backpressure was necessary with a screw rotational speed of 15 m/min. In some cases, when the mould opened, the sprue broke, stuck into the stationary mould half and had to be removed manually. To avoid this, a long holding time (20 s) had to be used, not only to compensate for the shrinkage of the part but also for the shrinkage of the sprue, especially to avoid the formation of voids. Furthermore, the part and the sprue had to be adequately stiff to avoid this phenomenon, thus for proper demoulding, long holding and residual cooling times (30 s) and a low mould temperature (20°C) had to be used.

The injection moulded samples were totally transparent, indicating their amorphous nature. After injecting the samples, 50 mm long, 2 mm by 4 mm specimens were cut for the DMA measurements, and 2 mm thick 15 mm by 15 mm specimens were cut for the WAXD measurements. The other injection moulded samples were shredded, repelletized, and the amorphous PLA pellets were investigated in two ways: firstly, it was reprocessed in the same way as before to analyse the processing differences; secondly, the pellets were annealed at 80°C for only 10 minutes to observe the beginning of the re-crystallization with a scanning electron microscope (SEM) type Jeol JSM6380 LA.

The specimens (for WAXD, DMA and DSC) were placed on a glass plate in a vented oven for annealing at 60-80-100-120-140°C for 10-20-30-40-50-60 minutes. The reason for the glass plate support was the low heat deflection temperature of the material. The notation of the samples is as follows: *X*/*Y*, where *X* represents the temperature [°C], and *Y* represents the time interval [min] of the annealing. The DMA measurements were made with a Perkin-Elmer Pyris Diamond dynamic mechanical analyser, while the DSC measurements were made with a Perkin-Elmer Pyris 1 differential scanning calorimeter. The crystallinity was calculated from the DSC melting enthalpies, using a melting enthalpy value of 75.57 J/g for 100% crystalline PLLA [22]. The un-annealed specimens were measured at heating rates of 1-2-5-10-15-20°C/min, while the annealed specimens were measured at a heating rate of 5°C/min. WAXD analysis was done with a Philips model PW 3710 based PW 1050 Bragg-Brentano parafocusing goniometer using CuK$_\alpha$ radiation ($\lambda = 0.15418$ nm).

Besides the analysis of the crystalline structure of pure PLA, 30 weight% maize starch (type Meritena 100, from Brenntag Hungária Ltd., Hungary) content PLA was made using a Brabender Plasti-Corder PL 2100 twin screw extruder. The processing of the annealed and un-annealed PLA/starch blends was analysed.

3. Results and discussion

To analyse the effect of the different crystalline content PLA specimens, they were annealed at different temperatures for different time periods as mentioned before. The transparency of the samples changed from transparent to nearly totally white as the crystallinity increased. This observation was verified by WAXD analysis. The results show that the un-annealed PLA had no crystallinity, but one significant peak appeared at 16.3° for the specimens annealed at 80°C. The intensity of the peak increased gradually as a function of annealing time at 80°C (Figure 1), and this peak also shifted to 16.6° for the specimen annealed at 120°C for 10 minutes.

Three more peaks appeared at 14.8, 19.0 and at 22.3° for samples annealed at higher temperatures (Figure 2), which indicate higher crystallinities, but the specimens annealed at 100, 120, and 140°C show the same WAXD spectrum independent of annealing time.

These specimens were also analysed by DMA and DSC. At first, the amorphous PLA specimen was examined (Figure 3).

As one can see in the DMA curve, the storage modulus of the amorphous PLA decreases at T_g, but as a

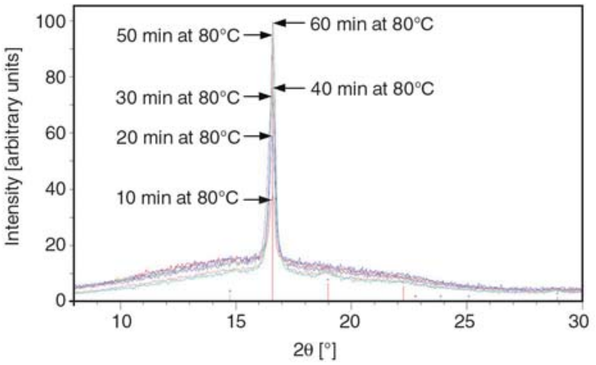

Figure 1. WAXD spectra of PLA annealed at 80°C for 10–60 minutes. The intensity of the peak increases as annealing time increases. The arrows point out the peak maxima.

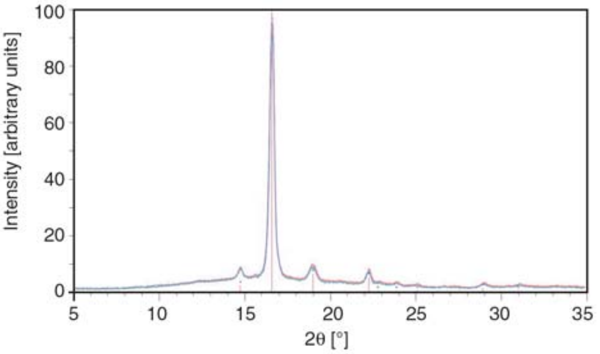

Figure 2. WAXD spectra of PLA annealed at 120°C for 10–60 minutes

result of re-crystallization during the measurement the storage modulus returns to that of a semi-crystalline material. In the DSC curve one can observe

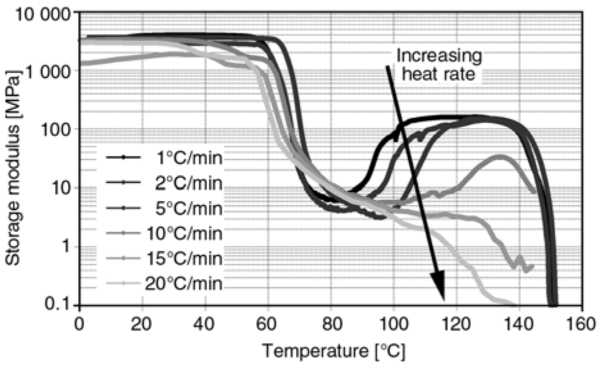

Figure 4. DMA curves of un-annealed PLA captured at 1-2-5-10-15-20°C/min heating rates

the T_g at 58°C, the re-crystallization exotherm between 80 and 105°C and the melting endotherm as a double peak between 140 and 160°C. With the increasing heating rate, the recrystalization during measurement was less significant (Figure 4, Figure 5).

At higher heating rates, the time to develop crystallinity was less, thus the DMA curves tends to the real curve of amorphous PLA. In the DSC curves one can see the decrease in crystallization enthalpies and enthalpies of fusion as the heating rate increases (Table 1).

The crystallization enthalpies and the enthalpies of fusion did not change within experimental error, thus the crystals formed during the cold crystallization at lower temperatures melted at 150°C. The crystallization peak has also shifted to higher tem-

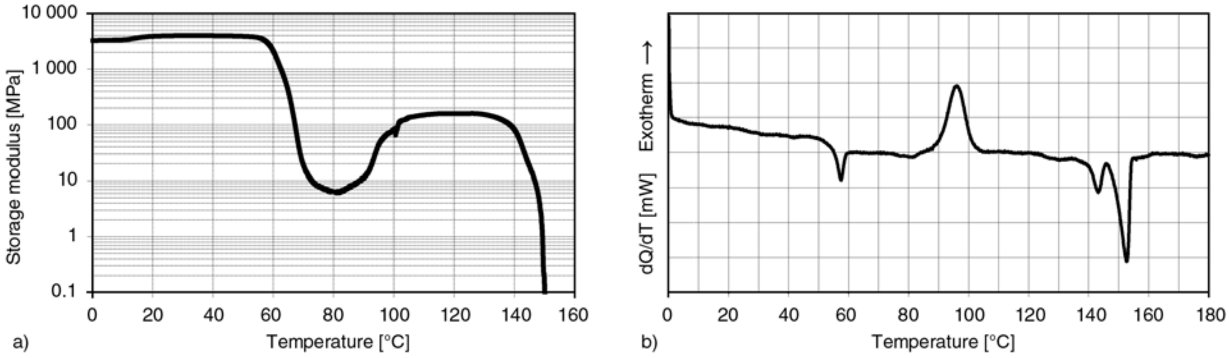

Figure 3. (a) DMA and (b) DSC curves of un-annealed, amorphous PLA captured at a 1°C/min heating rate

Table 1. Crystallization enthalpies and enthalpies of fusion of the unannealed specimens

Heat rate [°C/min]	Crystallization peak [°C]	Crystallization enthalpy [J/g]	Melting peak [°C]	Enthalpy of fusion [J/g]
2	96.1	–25.8	152.6	25.3
5	107.7	–29.9	152.6	27.5
10	117.8	–22.4	149.2	22.7
15	126.1	–11.4	151.9	11.5
20	130.7	–4.8	154.4	5.8

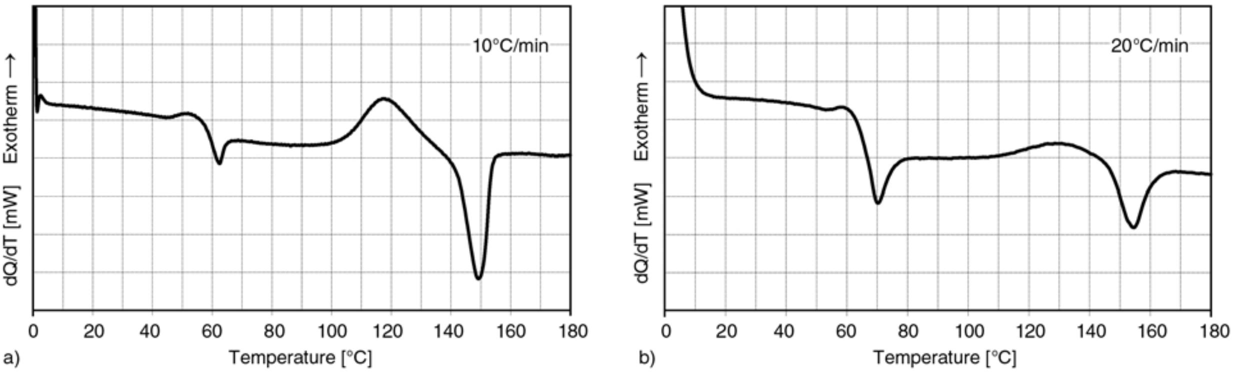

Figure 5. DSC curves of un-annealed PLA captured at (a) 10 and (b) 20°C/min heating rates

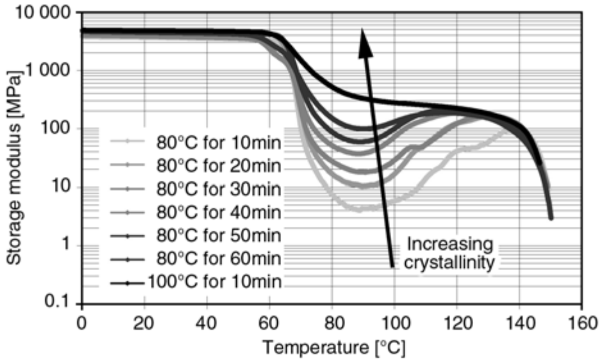

Figure 6. DMA curves of annealed PLA. The annealing temperatures and time intervals from the bottom curve to the top are: 80/10, 80/20, 80/30, 80/40, 80/50, 80/60, 100/10

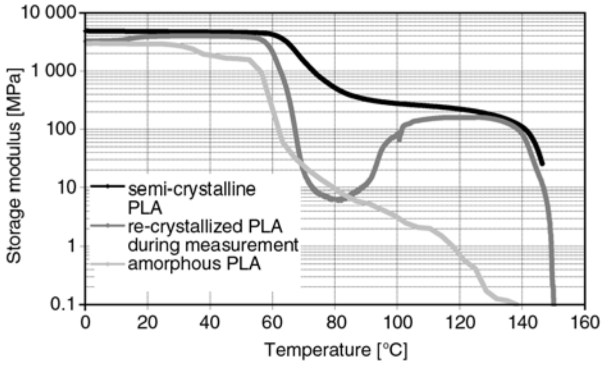

Figure 7. The DMA curve of amorphous, semi crystalline, and re crystallized PLA

peratures. For the annealed specimens, the loss in storage modulus decreased with increasing crystalline content (Figure 6).

It can be seen that during the measurement the un-annealed specimens fully re-crystallized, since the storage moduli returned to those of the specimen with the highest possible crystallinity around 120–140°C. The higher the crystallinity, the lower the storage modulus drop observed at the glass transition. Figure 7 summarizes the DMA curves for amorphous PLA, semi-crystalline PLA, and PLA re-crystallizing during measurement.

In the DSC curves the intensity of the exothermic peak observably decreases with increasing PLA crystallinity (Figure 8).

The enthalpy of fusion does not seem to change significantly after the different heat treatments (Table 2.), but from the differences in cold crystallization it is clear that the samples reached their maximum crystallinity after only 10 minutes at 100 and 120°C. It is further interesting that the double melting peak, indicative of the melting of both the α′- and α crystalline phases, changed to a single melting peak typical of the α crystalline phase.

The supplier of PLA Ingeo 3051D has published a know-how about crystallizing and drying of PLA [23]. The adherent feature of the amorphous PLA and the solution is well discussed, and warnings

Table 2. Crystallinity values, crystallization enthalpies and enthalpies of fusion of the annealed specimens

Annealing time and temperature	Crystallization peak [°C]	Crystallization enthalpy [J/g]	Melting peak [°C]	Enthalpy of fusion [J/g]	Crystallinity [%]
80°C, 10 min	105.4	–18.4	150.8	20.9	3.3
80°C, 20 min	100.9	–16.3	152.1	21.4	6.7
80°C, 30 min	99.4	–17.8	151.9	21.8	5.3
80°C, 40 min	95.4	–13.2	152.1	23.0	13.0
80°C, 50 min	91.1	–11.4	150.9	24.5	17.3
80°C, 60 min	96.4	–7.5	150.4	23.4	21.0
100°C, 10 min	none	none	151.4	25.8	34.1
120°C, 10 min	none	none	151.6	29.0	38.4

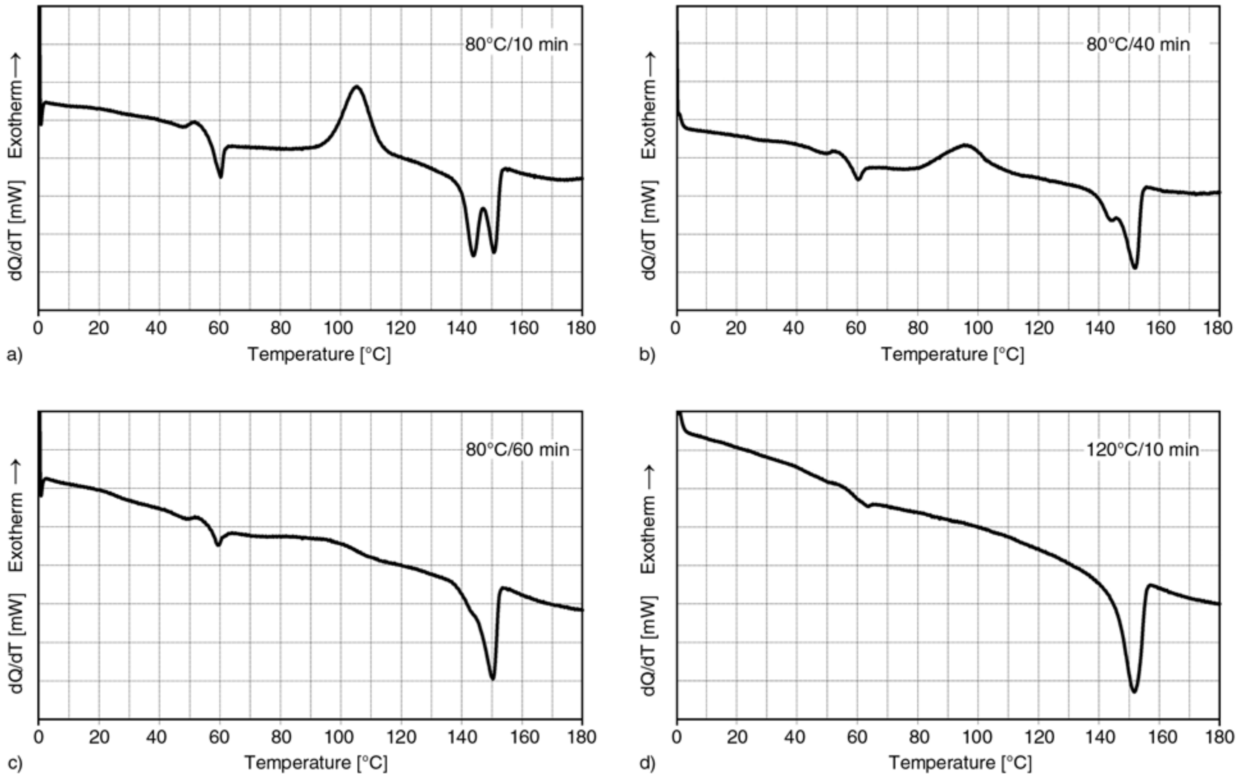

Figure 8. DSC curves of PLA annealed at 80°C for (a) 10, (b) 40, (c) 60 minutes and (d) at 120°C for 10 minutes

about pneumatic material transportation from driers to processing equipment are mentioned. Amorphous PLA was injection moulded to investigate the effect of recycled PLA on the processing, but it was found that from cycle to cycle more and more amorphous PLA pellets stuck to the surface of the screw and rotated together with the screw. The pellets stuck on the screw even at the feed zone, where the material should only be transported to the compression zone, but not melted (Figure 9).

As more and more pellets stuck to the screw, more and more torque was necessary to plasticize the material; finally it reached a value which could destabilize the injection moulding process. This phenomenon prevented further processing of the material until the barrel is cleaned. This effect was characterized by the number of 'problem free' processes before the needed cleaning procedure. For amorphous PLA, and for the used injection moulding machine and parameters, the number of problem free processes was around 10 cycles. To further analyse the adherent effect with SEM, amorphous pellets were heated at 80°C for 10 minutes in a conventional oven (Figure 10).

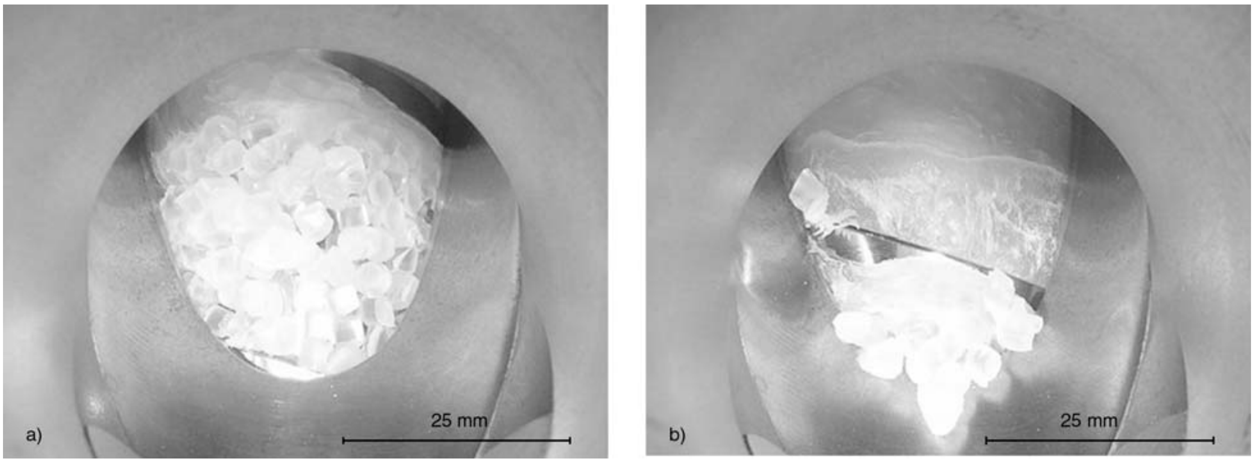

Figure 9. The amorphous PLA pellets stuck on the surface of the screw at the (a) beginning and at the (b) end of the feeding zone

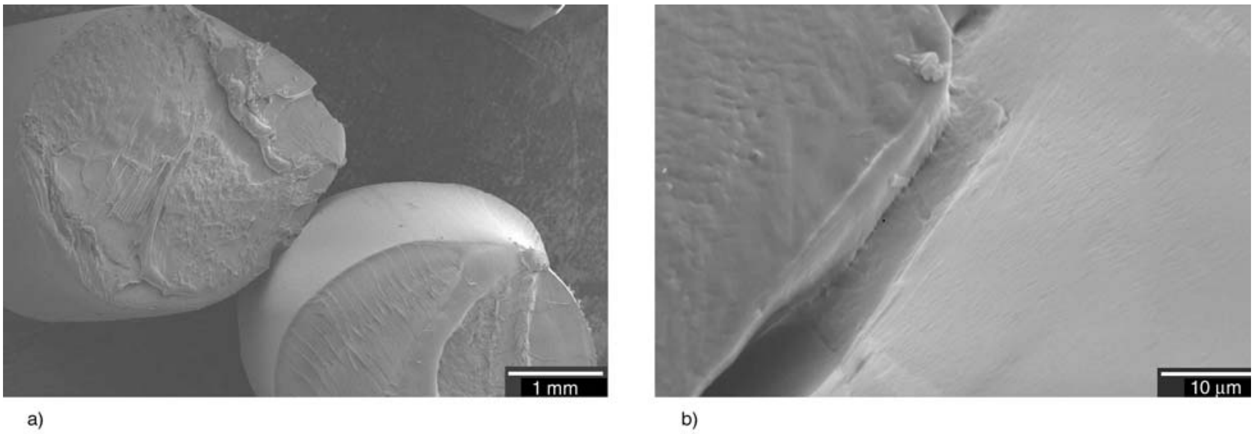

Figure 10. Welded surface of pellets at 80°C, with a magnification of (a) 20 and (b) 2000

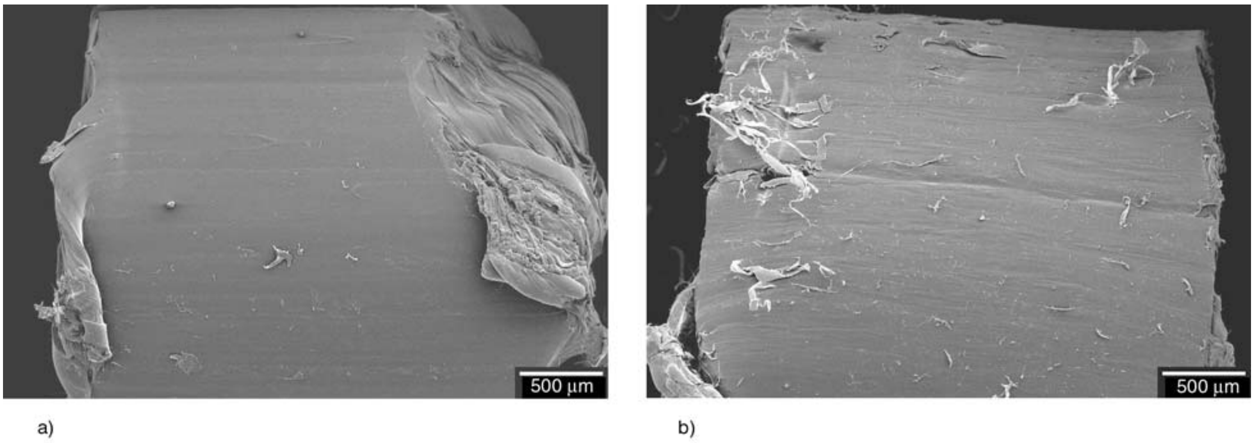

Figure 11. (a) Unannealed and (b) annealed pellet with peeled-off ribbons

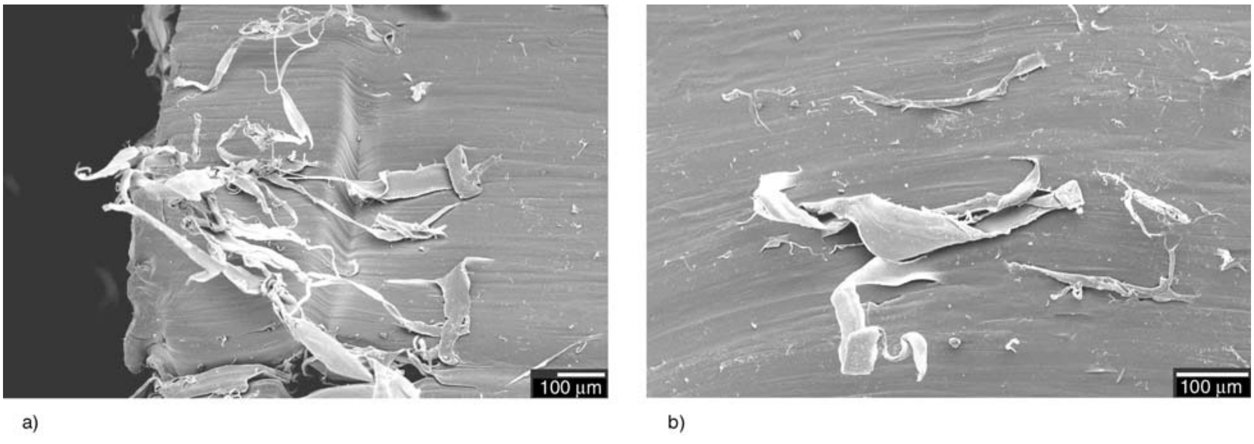

Figure 12. Peeled-off ribbons on the surface of PLA pellet, with a magnification of (a) 100 and (b) 150

As the SEM pictures showed, the pellets locally welded together, and a weld line between the pellets developed even at this low temperature. It can also be observed that for the pellets annealed at 120°C for 10 minutes, ribbon-like PLA formations peeled off the surface of the pellet, suggesting local melting of the pellets during crystallization (Figure 11, Figure 12).

This 'melting' is probably caused by the significant exothermic cold crystallization heat and the low heat transfer capabilities of PLA, and can be related to the softening of the amorphous phase only. During cold crystallization the exothermic heat is transported to the surface of the pellet, where due to the low heat transfer capabilities of PLA the accumulated exothermic heat causes local softening of the

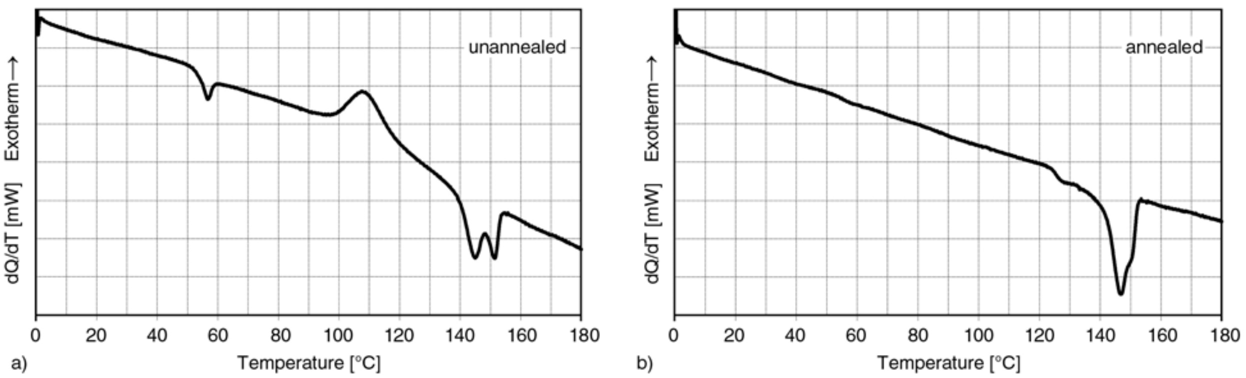

Figure 13. DSC curves of (a) annealed and (b) unannealed PLA/starch blends

amorphous phase. With the continuation of cold crystallization, the crystallinity increases which already retards the macro Brownian movement. Accordingly, the injection moulding difficulties could be totally overcome by the annealing of the amorphous pellets in a vented oven prior to injection moulding, because with higher crystallinity the re-crystallization phenomenon becomes negligibly small or disappears. The pellets will also stick together during the annealing process, but with low mechanical action they can be separated easily. With proper crystallization, the processing of re-crystallized PLA pellets was as easy as the processing of original (virgin) pellets; there were no processing problems within the investigated 100 injection cycles.

Although many authors made PLA based composites and further processed the pellets into injection moulded products, only a few reported the adherent effect, and even fewer reported that annealing was done before injection moulding. To analyse the effect of annealing on PLA based blends, 30 weight% starch content PLA was made using a twin screw extruder. The differences between the annealed (at 120°C for 60 minutes) and un-annealed blends can be seen in the DSC curves (Figure 13).

Here it can also be seen that after annealing the exothermic peak responsible for the adhering feature of the amorphous PLA – and thus causing unstable injection moulding technology – disappeared. No adherent effect was found with annealing of the PLA/starch blend, while the un-annealed pellets led again to processing difficulties. The injection moulding of the annealed pellets of the PLA/starch blend was found to be stable.

4. Conclusions

The crystalline structure of injection moulding grade polylactic acid (PLA) was analysed by wide angle X-ray diffraction (WAXD) spectrometry, dynamic mechanical analysis (DMA), differential scanning calorimetry (DSC), and the effect of the crystalline structure on the processing with injection moulding was analysed. The research is induced by the significant differences in crystallinity of the pure PLA resin, and the injection moulded product, and thus the reprocessing of PLA products. Different temperatures (60–140°C) and time intervals (10–60 minutes) were used to investigate the crystallization of injection moulded amorphous PLA specimens in a vented oven. The WAXD results show that in an annealing temperature range of 100–140°C, 10 minutes were enough to achieve as high crystallinity as possible for injection moulding grade PLA (crystalline content around 40%). The DMA properties show that the amorphous specimens re-crystallized during measurement, which gave rise to an increase in the storage modulus above T_g. At a high heating rate it was possible to measure the DMA curve of the amorphous PLA, thus the differences in DMA curves of the amorphous and semi-crystalline PLA could be studied. The DSC results showed a significant exothermic peak in the temperature range of 80–140°C which is related to cold crystallization. The exothermic peak decreased with increasing crystallinity, thus no exothermic peak could be observed for the fully annealed specimens (specimens with around 40% crystalline content).

Amorphous PLA was injection moulded to investigate the effect of recycled PLA on the processing, but due to the adherent feature of the amorphous PLA, pellets stuck to the screw already in the feeding zone, where the material should be only transported but not melted. This phenomenon destabilized the injection moulding process, preventing further processing after 10 injection cycles. It was observed by scanning electron microscopy (SEM) that the pellets welded together locally, and that ribbon-like formations peeled off the surface of the pellets. This suggests that during processing, due to the significant crystallization exotermic heat accumulated at the surface of the pellets, and due to the low heat transfer capability of the material, the amorphous phase of the pellets softens locally and causes the adherent effect that destabilizes the injection moulding processing. These injection moulding difficulties can be totally overcome by re-crystallization of the amorphous material prior to the injection. In this case, within the investigated 100 injection cycles, the processing was easy and problem-free, like the processing of semi-crystalline PLA. It was also found that annealing is also effective in eliminating processing difficulties when processing PLA based, starch filled materials.

Acknowledgements

This paper was supported by the János Bólyai Research Scholarship of the Hungarian Academy of Sciences and the Hungarian-French (TéT FR-5/2007) Intergovernmental Science and Technology Cooperation Programme. The authors would like to thank Arburg Hungária Kft. for the injection moulding machine, Wittmann Robottechnika Kft. for the W711 robot and the mould temperature control unit, and Lenzkes GmbH for the clamping tool system.

References

[1] Avérous L.: Biodegradable multiphase systems based on plasticized starch: A review. Polymer Reviews, **44**, 231–274 (2004).
DOI: 10.1081/MC-200029326

[2] Ren X.: Biodegradable plastics: A solution or a challenge? Journal of Cleaner Production, **11**, 27–40 (2003).
DOI: 10.1016/S0959-6526(02)00020-3

[3] Zhang M. Q.: Polymeric materials from natural resources- Emerging as the times require. Express Polymer Letters, **1**, 406 (2007).
DOI: 10.3144/expresspolymlett.2007.57

[4] Siracusa V., Rocculi P., Romani S., Dalla Rosa M.: Biodegradable polymers for food packaging: A review. Trends in Food Science and Technology, **19**, 634–643 (2008).
DOI: 10.1016/j.tifs.2008.07.003

[5] Czigány T., Romhány G., Kovács J. G.: Starch for injection moulding purposes. in ‘Engineering biopolymers: Homopolymers, blends, and composites’ (eds.: Fakirov S., Bhattacharyya D.) Hanser Publisher, Munich, Vol 1, 81–108 (2006).

[6] Tábi T., Kovács J. G.: Examination of injection moulded thermoplastic maize starch. Express Polymer Letters, **1**, 804–809 (2007).
DOI: 10.3144/expresspolymlett.2007.111

[7] Gáspár M., Benkő Zs., Dogossy G., Réczey K., Czigány T.: Reducing water absorption in compostable starch-based plastics. Polymer Degradation and Stability, **90**, 563–569 (2005).
DOI: 10.1016/j.polymdegradstab.2005.03.012

[8] Stepto R. F. T.: The processing of starch as a thermoplastic. Macromolecular Symposia, **201**, 203–212 (2003).
DOI: 10.1002/masy.200351123

[9] Averous L., Moro L., Dole P., Fringant C.: Properties of thermoplastic blends: Starch-polycaprolactone. Polymer, **41**, 4157–4167 (2000).
DOI: 10.1016/S0032-3861(99)00636-9

[10] Avérous L., Fringant C.: Association between plasticized starch and polyesters: Processing and performances of injected biodegradable systems. Polymer Engineering and Science, **41**, 727–734 (2001).
DOI: 10.1002/pen.10768

[11] Avérous L., Fauconnier N., Moro L., Fringant C.: Blends of thermoplastic starch and polyesteramide: Processing and properties. Journal of Applied Polymer Science, **76**, 1117–1128 (2000).
DOI: 10.1002/(SICI)1097-4628(20000516)76:7<1117::AID-APP16>3.0.CO;2-W

[12] Schwach E., Avérous L.: Starch-based biodegradable blends: Morphology and interface properties. Polymer International, **53**, 2115–2124 (2004).
DOI: 10.1002/pi.1636

[13] Mohanty A. K., Misra M., Hinrichsen G.: Biofibres, biodegradable polymers and biocomposites: An overview. Macromolecular Materials and Engineering, **276–277**, 1–24 (2000).
DOI: 10.1002/(SICI)1439-2054(20000301)276:1<1::AID-MAME1>3.0.CO;2-W

[14] Yu L., Dean K., Li L.: Polymer blends and composites from renewable resources. Progress in Polymer Science, **31**, 576–602 (2006).
DOI: 10.1016/j.progpolymsci.2006.03.002

[15] Vilpoux O., Avérous L.: Starch-based plastics. in ‘Technology, use and potentialities of Latin American starchy tubers’ (eds.: Cereda M. P., Vilpoux O.) NGO Raízes and Cargill Foundation, São Paolo, Brasil, Vol 3, 521–553 (2004).

[16] Lim L-T., Auras R., Rubino M.: Processing technologies for poly(lactic acid). Progress in Polymer Science, **33**, 820–852 (2008).
DOI: 10.1016/j.progpolymsci.2008.05.004

[17] Pyda M., Bopp R. C., Wunderlich B.: Heat capacity of poly(lactic acid). Journal of Chemical Thermodynamics, **36**, 731–742 (2004).
DOI: 10.1016/j.jct.2004.05.003

[18] Pan P., Zhu B., Kai W., Dong T., Inoue Y.: Polymorphic transition in disordered poly(L-lactide) crystals induced by annealing at elevated temperatures. Macromolecules, **41**, 4296–4304 (2008).
DOI: 10.1021/ma800343g

[19] Pan P., Kai W., Zhu B., Dong T., Inoue Y.: Polymorphous crystallization and multiple melting behavior of poly(L-lactide): Molecular weight dependence. Macromolecules, **40**, 6898–6905 (2007).
DOI: 10.1021/ma071258d

[20] Martin O., Avérous L.: Poly(lactic acid): Plasticization and properties of biodegradable multiphase systems. Polymer, **42**, 6209–6219 (2001).
DOI: 10.1016/S0032-3861(01)00086-6

[21] Li H., Huneault M. A.: Effect of nucleation and plasticization on the crystallization of poly(lactic acid). Polymer, **48**, 6855–6866 (2007).
DOI: 10.1016/j.polymer.2007.09.020

[22] Kantoglu Ö., Güven O.: Radiation induced crystallinity damage in poly(L-lactic acid). Nuclear Instruments and Methods in Physics Research Section B: Beam Interactions with Materials and Atoms, **197**, 259–264 (2002).
DOI: 10.1016/S0168-583X(02)01473-8

[23] NatureWorks: Crystallizing and drying of PLA. http://www.natureworksllc.com (2010).